

1  
2

CONNECTING OBSERVED MICROBURST PRECIPITATION WITH ITS  
SCATTERING MECHANISM

3

by

Mykhaylo Sergeevich Shumko

4

A dissertation submitted in partial fulfillment  
of the requirements for the degree

of

Doctor of Philosophy

in

Physics

5

MONTANA STATE UNIVERSITY  
Bozeman, Montana

October 2019

6

7

©COPYRIGHT

8

by

Mykhaylo Sergeevich Shumko

2019

All Rights Reserved

## DEDICATION

<sup>9</sup> I dedicate this to all MSU students who use L<sup>A</sup>T<sub>E</sub>X. Dedication is optional  
<sup>10</sup> and may be no longer than one page, single spaced, and should precede the  
<sup>11</sup> acknowledgments page.

## ACKNOWLEDGEMENTS

<sup>12</sup> I would like acknowledge the countless engineers, technicians, and scientists who  
<sup>13</sup> made the FIREBIRD, AC-6, and RBSP missions a success. This work was supported  
<sup>14</sup> by Montana State University and by NASA Headquarters under the NASA Earth and  
<sup>15</sup> Space Science Fellowship Program - Grant 80NSSC18K1204. **Add co-author support.**

## TABLE OF CONTENTS

16	1. INTRODUCTION .....	1
17	Charged Particle Motion in Electric and Magnetic Fields .....	2
18	Particle Populations and Their Interractions in the Magnetosphere .....	8
19	Inner Magnetosphere Populations.....	11
20	Plasmasphere.....	13
21	Ring Current .....	15
22	Radiation Belts.....	16
23	Radiation Belt Particle Sources and Sinks .....	20
24	Adiabatic Heating .....	20
25	Wave Resonance Heating .....	21
26	Particle Losses .....	25
27	Microbursts .....	26
28	Scope of Reserach .....	29
29	2. CHAPTER TWO	
30	EVIDENCE OF MICROBURSTS OBSERVED NEAR THE EQUA-	
31	TORIAL PLANE IN THE OUTER VAN ALLEN RADIATION	
32	BELT .....	31
33	Contribution of Authors and Co-Authors .....	31
34	Manuscript Information .....	32
35	Key Points .....	33
36	Abstract .....	33
37	Introduction .....	33
38	Spacecraft Instrumentation .....	36
39	Observations .....	37
40	Analysis .....	40
41	Microburst and Source PSD .....	40
42	Motion of resonant electrons in phase space .....	43
43	Comparing the microburst PSD to diffusion theory .....	46
44	Discussion and Conclusions .....	48
45	Acknowledgments .....	49
46	3. CHAPTER THREE	
47	MICROBURST SCALE SIZE DERIVED FROM MULTIPLE BOUNCES	
48	OF A MICROBURST SIMULTANEOUSLY OBSERVED WITH	
49	THE FIREBIRD-II CUBESATS .....	51
50	Contribution of Authors and Co-Authors .....	51

## TABLE OF CONTENTS – CONTINUED

51	Manuscript Information .....	52
52	Key Points .....	53
53	Abstract .....	53
54	Introduction .....	54
55	Spacecraft and Observation .....	56
56	Analysis.....	59
57	Electron Bounce Period .....	60
58	Microburst Energy Spectra .....	62
59	Microburst Scale Sizes .....	62
60	Discussion and Conclusions .....	65
61	Acknowledgments .....	67
62	4. CONCLUSION .....	68
63	REFERENCES CITED.....	69
64	APPENDIX: Appendix A .....	78
65	APPENDIX: Appendix B .....	81
66	Time and position correction .....	81

## LIST OF FIGURES

Figure	Page
67      1.1 The three periodic motions of charged particles 68      in Earth's dipole magnetic field. These motions 69      are: gyration about the magnetic field line, bounce 70      motion between the magnetic poles, and azimuthal 71      drift around the Earth. Figure from (Baumjohann 72      and Treumann, 1997). ....	2
73      1.2 Charged particle motion in a uniform magnetic field 74 $\vec{B}$ . Panel (A) shows the geometry defining the 75      pitch angle, $\alpha$ . Panel (B) and (C) show two helical 76      electron trajectories with dashed lines assuming a 77      large and small $\alpha$ (corresponding to a small and large 78      parallel velocity $v_{  }$ ), respectively. ....	6
79      1.3 Contours of constant gyration, bounce, and drift 80      frequencies for electrons and protons in a dipole field. 81      Figure from Schulz and Lanzerotti (1974). ....	7
82      1.4 Macroscopic structures in the outer magnetosphere. 83      The solar wind with its frozen-in interplanetary 84      magnetic field is shown on the left and is traveling 85      supersonically towards the right. The solar wind 86      envelops Earth's magnetic field to create the mag- 87      netosphere cavity. Since the solar wind is traveling 88      supersonically, it creates a bow shock up stream. 89      Downstream of the bow shock the shocked solar wind 90      plasma inside the magnetosheath flows around the 91      magnetopause, a boundary between the solar wind 92      and magnetosphere. Figure from Baumjohann and 93      Treumann (1997). ....	9
94      1.5 Macroscopic structures in the inner magnetosphere 95      most relevant to this dissertation. The plasmas- 96      sphere, and the radiation belts are shown and ring 97      current is co-located there as well. Sun is to the left. 98      Figure from Baumjohann and Treumann (1997). ....	10
99      1.6 The series of steps involved in magnetic reconnection 100     with a southward IMF. Figure from Baumjohann 101     and Treumann (1997). ....	12

## LIST OF FIGURES – CONTINUED

Figure	Page
102      1.7 Equipotential lines and electric field arrows due to 103      the superposition of the co-rotation and convection 104      electric fields. Electrons in the shaded region execute 105      closed orbits. Outside of the shaded regions the 106      electrons are not trapped and will escape. The 107      region separating the two regimes is called the Alfvén 108      layer. Figure from Baumjohann and Treumann (1997).....	14
109      1.8 The DST index during the St. Patrick's Day 2015 110      storm. This storm was caused by a coronal mass 111      ejection on March 15th, 2015. The storm phases 112      are: initial phase, main phase, and recovery phase. 113      The initial phase occurred when the Dst peaked at 114      +50 nT on March 17th during which the ring current 115      was eroded by the coronal mass ejection during the 116      interval shown by the red bar. Then the rapid 117      decrease to $\approx -200$ nT was during the main phase 118      where many injections from the magnetotail pumped 119      up the ring current which reduced Earth's magnetic 120      field strength at the ground and is shown with the 121      green bar. Lastly, the recovery phase lasted from 122      March 18th to approximately March 29th during 123      which the ring current particles were lost and the 124      ring current returned to its equilibrium state. The 125      recovery phase is shown with the blue bar.....	17
126      1.9 The two radiation belts with a the locations of 127      various satellites and orbits. Figure from (Horne 128      et al., 2013). .....	18
129      1.10 The dynamics of the outer radiation belt in 1997 130      from the POLAR satellite. Top panel shows the 1.2- 131      2.4 MeV electron flux as a function of L and 1997 day 132      of year. The middle panel shows the DST index, and 133      bottom panel shows the solar wind velocity. Figure 134      from (Reeves et al., 2003). .....	19

## LIST OF FIGURES – CONTINUED

Figure	Page
135      1.11 The trajectories of an electron and a right-hand cir- 136      cularly polarized wave during a cyclotron resonance. 137      The electron's $v_{\parallel}$ and the wave's $k_{\parallel}$ are in opposite 138      directions such that the wave's frequency is Doppler 139      shifted to a integer multiple of the electron cyclotron 140      frequency. Figure from (Tsurutani and Lakhina, 1997). ....	22
141      1.12 Various wave modes in the magnetosphere. Ultra 142      low frequency waves occur throught the magneto- 143      sphere. Chorus waves are typically observed in 144      the 0-12 midnight-dawn region. EMIC waves are 145      typically observed in the dusk MLT sector. Hiss 146      waves are observed inside the plasmasphere. Figure 147      from Millan and Thorne (2007). ....	24
148      1.13 An example train of microbursts observed by FIREBIRD- 149      II unit 4 on February 2nd, 2015. The colored curves 150      show the differential energy channel count rates in 151      six channels from $\approx 200$ keV to greater than 1 MeV. 152      The x-axis labels show auxiliary information such as 153      time of observation and the spacecraft position in L, 154      MLT, latitude and longitude coordinates. ....	27
155      1.14 Relativistic ( $> 1$ MeV) distribution of microburst 156      occurrence rates as a function of L and MLT. The 157      three panels show the microburst occurrence rate 158      dependence on geomagnetic activity, parameterized 159      by the auroral electrojet (AE) index for (a) $AE <$ 160      100 nT, (b) $100 < AE < 300$ nT and (c) $AE > 300$ 161      nT. Figure from Douma et al. (2017)....	28

## LIST OF FIGURES – CONTINUED

Figure	Page
162      2.1 Electron and wave conditions from the MagEIS-A 163      and EMFISIS WFR sensors for the microburst time 164      interval. Panels (a), (b), and (c) are from RBSP-A 165      with its position information annotated in panel (a). 166      Panels (d), (e), and (f) are from RBSP-B with its 167      position information annotated in panel (d). Panel 168      (a) is the MagEIS-A high rate timeseries. Panels (b) 169      and (e) show the evolution of the MagEIS-A $J$ as a 170      function of $\alpha_L$ from the $\sim 40$ to $\sim 60$ keV channel. 171      Every 10th point is shown in panel (b). The solid 172      black line in panels (a) and (b) mark the end of 173      the time period used for the PSD fit extrapolation 174      analysis explained in section 3. The dashed black 175      lines in panels (a) and (b) show the time interval 176      used for the observed microburst PSD. Panels (c) 177      and (f) show the EMFISIS WFR spectra, with the 178      available burst data superposed. The red, green, and 179      cyan traces are equatorial $f_{ce0}$ , $f_{ce0}/2$ , and $f_{ce0}/10$ , 180      respectively. ....	39
181      2.2 Panel (a) shows the MagEIS-A high rate timeseries. 182      Panel (b) shows the RBSPICE EBR count rate 183      timeseries for $\zeta 19$ keV electrons. The microbursts 184      were observed between 11:17:10 - 11:17:12 UT and 185      are indicated with the vertical black arrows in panels 186      (a) and (b) for MagEIS-A times. Panel (c) shows the 187      RBSPICE EBR (family of relatively sparse sampled 188      curves) and MagEIS-A $J$ from the 29-41 keV energy 189      channel (single curve) as a function of $\alpha_L$ . The 190      vertical dashed lines show the time interval for the 191      PSD analysis.....	41

## LIST OF FIGURES – CONTINUED

Figure	Page
192      2.3 The colored annulus represents $f(p_\perp, p_{\parallel})$ in normalized momentum space, parallel and perpendicular to the background magnetic field. The microburst $f(p_\perp, p_{\parallel})$ is highlighted with the white circle. The columns show different powers of the sine extrapolation, and rows show the different magnetic latitudes of the scattering. The white dotted traces represent the boundary between the data and extrapolation. The green, red, and white solid traces are the resonance curves for $\omega = 0.2\Omega_{ce}$ , $0.4\Omega_{ce}$ , $0.6\Omega_{ce}$ , respectively. The cyan dashed traces are the diffusion curves for a $\omega = 0.4\Omega_{ce}$ wave (waves of other frequency have similar diffusion curves). The magnetic latitude of the scattering, the ratio of the plasma to the cyclotron frequency, and the power of the sine extrapolation is annotated in each panel. For the resonance and diffusion curves, the density model assumed a $n_L = 1 e^-/cm^3$ and $\psi = -1$ .....	44
210      3.1 HiRes data of the microburst observed at February 2nd, 2015 at 06:12:53 UT, smoothed with a 150 ms rolling average. The subsequent bounces showed some energy dispersion. As discussed in Appendix B, a time correction of -2.28 s was applied to FU3. While the flux from five energy channels is shown, only channels with reasonable counting statistics were used for the spatial scale analysis. Vertical colored bars show the $\sqrt{N}$ error every 10th data point and vertical black bars are lined up with the peaks in the 220-283 keV energy channel to help identify dispersion.....	58

## LIST OF FIGURES – CONTINUED

Figure	Page
222      3.2 Observed and theoretical $t_b$ for electrons of energies 223      from 200 to 770 keV. The solid black line is $t_b$ 224      in a dipole magnetic field, derived in Schulz and 225      Lanzerotti (1974). The red dotted and cyan dashed 226      lines are the $t_b$ derived using the T89, and T04 227      magnetic field models with IRBEM-Lib. Lastly, 228      the blue dot-dash curve is the $t_b$ derived using the 229      Olson & Pfitzer Quiet model. The green and purple 230      rectangles represent the observed $t_b$ for FU3 and 231      FU4 using a Gaussian fit, respectively. The blue 232      rectangles represent the observed $t_b$ calculated with 233      the minima between the bounces. The width of the 234      boxes represent the width of those energy channels, 235      and the height represents the uncertainty from the fit.....	61
236      3.3 The topology of the FIREBIRD-II orbit and the 237      multiple bounces of the microburst projected onto 238      latitude and longitude with axis scaled to equal 239      distance. Attributes relating to FU3 shown in red 240      dashed lines, and FU4 with blue solid lines. The 241      spacecraft path is shown with the diagonal lines, 242      starting at the upper right corner. The labels P1- 243      4 for FU4 and P1-5 for FU3 indicate where the 244      spacecraft were when the $N^{th}$ peak was seen in 245      the lowest energy channel in the HiRes data. The 246      stars with the accompanying energy labels represent 247      the locations of the electrons with that energy that 248      started at time of P1, and were seen at the last peak 249      on each spacecraft. The rectangles represent the 250      lower bound of the microburst scale size, assuming 251      that the majority of the electrons were in the upper 252      boundary of energy channel 4.....	64

## LIST OF FIGURES – CONTINUED

Figure	Page
253      A.1 Panel (A) shows the magnetic power spectral density 254      as a function of frequency and time from the EMFI- 255      SIS WFR instrument on board RBSP-A. The “hiss- 256      like” wave used for the resonant diffusion analysis 257      was observed starting at 11:17:03 UT. In the same 258      format as panel (A), panel (B) shows the polar angle 259      of the wave vector for this time period. The wave 260      of interest had a normal wave vector, $\theta_k < 30^\circ$ . 261      Since the results in panel (B) are valid only for high 262      planarity, panel (C) shows planarity in the same 263      format as panels (A) and (B). The wave of interest 264      was found to have a planarity of $> 0.8$ . Lastly, panel 265      (D) shows the available burst mode data. ....	79
266      A.2 Ratio of the RBSPICE EBR at microburst times 267      indicated with the black vertical arrows in Fig. 2, 268      to the EBR at the same pitch angles one spin prior 269      (quiet time). The microburst flux was enhanced by 270      10-80% across $100^\circ < \alpha_L < 160^\circ$ PA, and appear to 271      be peaked closer to $\alpha_L = 90^\circ$ ....	80
272      B.1 Cross-correlation time lag analysis applied to a train 273      of microbursts. Panel (a) and (b) show the count 274      rate from the lowest energy channel. Panel (c) shows 275      the cross-correlation coefficient as a function of time 276      lag. Panel (d) shows the shifted timeseries. Clock 277      difference was 2.23 s. ....	83
278      B.2 Same analysis as Fig. B.1 on a different time period. 279      Clock difference was 2.21 s. ....	84
280      B.3 Same analysis as Fig. B.1 on a different time period. 281      Clock difference was 2.25 s. ....	85
282      B.4 Same analysis as Fig. B.1 on a different time period. 283      Clock difference was 2.27 s. ....	86

## LIST OF FIGURES – CONTINUED

Figure		Page
284	B.5 Same cross-correlation time lag analysis applied to	
285	stationary spatial structures. The cross-correlation	
286	lag between these events is a sum of the clock differ-	
287	ence and time lag due to the spacecraft separation.	
288	The lag derived at this time was 4.95 s.....	87
289	B.6 Same analysis as Fig. B.5 applied to a different	
290	stationary spatial feature. The lag derived at this	
291	time was 5.01 s. ....	88

## NOMENCLATURE

292

- $\mu$  Dynamic viscosity
- $\mathbf{n}$  Normal vector
- $\mathbf{u}$  Velocity vector

293

## INTRODUCTION

294        Above Earth's atmosphere are the a pair of Van Allen radiation belts, a complex  
295        and dynamic plasma environment that effects our technology-driven society. These  
296        effects include: a higher radiation dose for astronauts and cosmonauts, higher chance  
297        of spacecraft failure due to single event upsets that can lead to catastrophic latchups,  
298        degradation of silicon (changing the silicon doping) from an extended radiation dose  
299        that can degrade a transistor to the point where it no longer function as a switch,  
300        and the degradation of the ozone layer due to the chemical production of  $\text{NO}_X$  and  
301         $\text{HO}_X$  molecules. With these effects in mind, it is no surprise that the radiation belts  
302        have been extensively studied since their discovery in the 1960s.

303        One natural phenomenon in the radiation belts that has been a topic of interest  
304        in the space physics community is wave-particle intersections that, as we will explore  
305        throughout this dissertation, can accelerate particles to very high energies (e.g.  $\approx$   
306        MeV for electrons) and scatter them into the atmosphere.

307        The goal of this dissertation is to study the wave-particle mechanism that  
308        scatters microbursts, a sub-second impulse of electrons into Earth's atmosphere.  
309        Before we dive deep into the physics of wave-particle interactions, an introduction to  
310        Earth's magnetosphere is warranted. Single charged particle motion in Earth's electric  
311        and magnetic fields will be described first. Then the major particle populations in  
312        the magnetosphere and the coupling between them will be described. Lastly, a brief  
313        overview of wave-particle interactions and their effects will be presented.

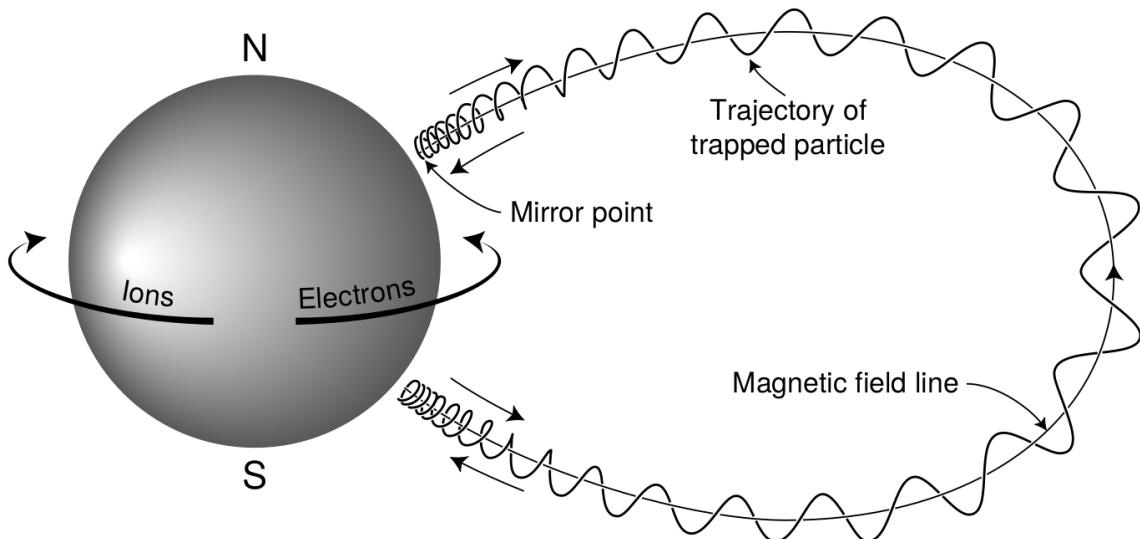


Figure 1.1: The three periodic motions of charged particles in Earth's dipole magnetic field. These motions are: gyration about the magnetic field line, bounce motion between the magnetic poles, and azimuthal drift around the Earth. Figure from (Baumjohann and Treumann, 1997).

<sup>314</sup>

### Charged Particle Motion in Electric and Magnetic Fields

A charged particle trapped in the magnetosphere will experience three types of periodic motion in Earth's nearly dipolar magnetic field. The three motions are ultimately due to the Lorentz force that a particle of momentum  $\vec{p}$ , charge  $q$ , and velocity  $\vec{v}$  experiences in an electric field  $\vec{E}$  and magnetic field  $\vec{B}$  and is given by

$$\frac{d\vec{p}}{dt} = q(\vec{E} + \vec{v} \times \vec{B}). \quad (1.1)$$

- <sup>315</sup> In the magnetosphere, the three periodic motions in decreasing frequency are gyration,
- <sup>316</sup> bounce, and drift and are schematically shown in Fig. 1.1. Each of these
- <sup>317</sup> motions have a corresponding conserved quantity i.e. an adiabatic invariant.

The highest frequency periodic motion is gyration about a magnetic field of

magnitude  $B$ . This motion is circular with a Larmor radius of

$$r = \frac{mv_{\perp}}{|q|B} \quad (1.2)$$

where  $m$  is the mass and  $v_{\perp}$  the particle's velocity perpendicular to  $\vec{B}$ . This motion has a corresponding gyrofrequency

$$\Omega = \frac{|q|B}{m} \quad (1.3)$$

in units of radians/second. Inside the radiation belts the electron gyrofrequency,  $\Omega_e$  is on the order of a kHz. The corresponding adiabatic invariant is found by integrating the particle's canonical momentum around the particle's path of gyration

$$J_i = \oint (\vec{p} + q\vec{A}) \cdot d\vec{l} \quad (1.4)$$

where  $J_i$  is the  $i^{th}$  adiabatic invariant and  $\vec{A}$  is the magnetic vector potential. This integral is carried out by integrating the first term over the circumference of the gyro orbit and integrating the second term using Stokes theorem to calculate the magnetic flux enclosed by the gyro orbit. With suitable integration,  $J_1 \sim v_{\perp}^2/B$  and is conserved as the frequency of the driving force,  $\omega$  satisfies  $\omega \ll \Omega_e$ .

The second highest frequency periodic motion is bouncing due to a parallel gradient in  $\vec{B}$ . This periodic motion naturally arises in the magnetosphere because Earth's magnetic field is stronger near the poles, and artificially in the laboratory in magnetic bottle machines. To understand this motion we first we need to define the concept of pitch angle  $\alpha$  as the angle between  $\vec{B}$  and  $\vec{v}$  which is schematically shown in Fig. 1.2a. The pitch angle relates  $v$  with  $v_{\perp}$ , and  $v_{||}$  (the component of the particles velocity parallel to  $\vec{B}$ ). As shown in 1.2b and c, a larger  $\alpha$  will tighten the

<sup>330</sup> particle's helical trajectory and vice versa.

Assuming the particle's kinetic energy is concerned, the conservation of  $J_1$  implies that given a particle's  $v_{\perp}(0)$  and  $B(0)$  at the magnetic equator (where Earth's magnetic field is usually at a minimum), we can calculate its  $v_{\perp}(s)$  along the particle's path  $s$  by calculating  $B(s)$  from magnetic field models. The particle's perpendicular velocity is then related via

$$\frac{v_{\perp}^2(0)}{B(0)} = \frac{v_{\perp}^2(s)}{B(s)} \quad (1.5)$$

<sup>331</sup> which can be rewritten as

$$\frac{v^2 \sin^2 \alpha(0)}{B(0)} = \frac{v^2 - v_{\parallel}^2(s)}{B(s)} \quad (1.6)$$

<sup>332</sup> and re-arranged to solve for  $v_{\parallel}(s)$

$$v_{\parallel}(s) = v \sqrt{1 - \frac{B(s)}{B(0)} \sin^2 \alpha(0)} \quad (1.7)$$

<sup>333</sup> which will tend towards 0 when the second term in the radical approaches 1.

<sup>334</sup> The location where  $v_{\parallel}(s) = 0$  is called the mirror point and is where a particle  
<sup>335</sup> stops and reverses direction. Since Earth's magnetic field is stronger towards the  
<sup>336</sup> poles, the mirroring particle will execute periodic bounce motion between its two  
<sup>337</sup> mirror points in the northern and southern hemispheres. The corresponding adiabatic  
<sup>338</sup> invariant,  $J_2$  is

$$J_2 = \oint p_{\parallel} ds \quad (1.8)$$

where  $ds$  describes the particle path between the mirror points in the northern and southern hemispheres (see Fig. 1.1).  $J_2$  is found by substituting Eq. 1.7 into Eq. 1.8 and defining the magnetic field strength at the mirror points as  $B_m$  where  $\alpha(m) = 90^\circ$ .

The  $J_2$  integral can be written as

$$J_2 = 2p \int_{m_n}^{m_s} \sqrt{1 - \frac{B(s)}{B(m)}} ds \quad (1.9)$$

where  $m_n$  and  $m_s$  are the northern and southern mirror points, respectively. The bounce period can be estimated (e.g. Baumjohann and Treumann, 1997) to be

$$t_b \approx \frac{LR_e}{\sqrt{W/m}} (3.7 - 1.6 \sin \alpha(0)) \quad (1.10)$$

where  $L$  is the  $L$ -shell which describes the distance from the Earth's center to the location where a particular magnetic field line crosses the magnetic equator, in units of Earth radii,  $R_e$ .  $W$  is the particle's kinetic energy. As with gyration, a particle bounces as long as  $\omega \ll \Omega_b$ , where  $\Omega_b$  is the bounce frequency.

At this stage it is instructional to introduce the notion of the loss cone pitch angle,  $\alpha_L$ . A particle with  $\alpha \leq \alpha_L$  will mirror at or below  $\approx 100$  km altitude in the atmosphere. A particle at those altitudes will encounter Earth's atmosphere and has a significant probability of Coulomb scattering with atmospheric particles and be lost to the atmosphere.

The slowest periodic motion experienced by charged particles in Earth's magnetic field is azimuthal drift around the Earth. This drift results from a combination of a radial gradient in  $\vec{B}$  and the curvature of the magnetic field. The radial gradient drift arises because Earth's magnetic field is stronger near the Earth where the particle's gyroradius radius of curvature is smaller as it gyrates towards stronger magnetic field, and larger when it gyrates outward. The overall effect is the particle gyro orbit does not close on itself and negatively charged particles drift East and positively charged particles drift West. The radial gradient drift is enhanced by the centrifugal force that a particle experiences as it bounces along the curved field lines. The drift adiabatic

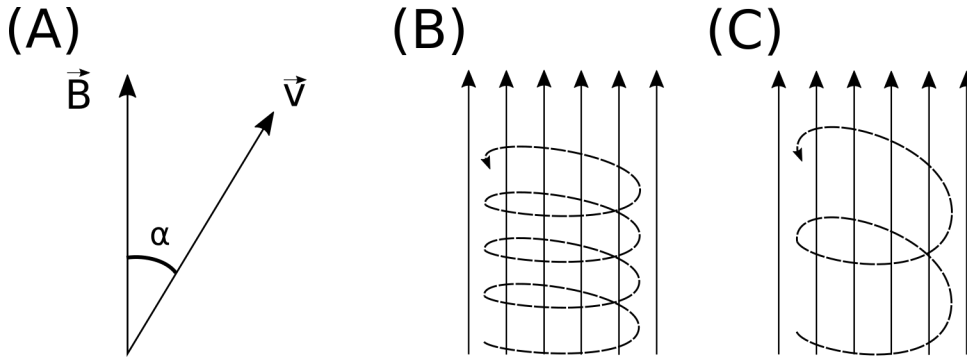


Figure 1.2: Charged particle motion in a uniform magnetic field  $\vec{B}$ . Panel (A) shows the geometry defining the pitch angle,  $\alpha$ . Panel (B) and (C) show two helical electron trajectories with dashed lines assuming a large and small  $\alpha$  (corresponding to a small and large parallel velocity  $v_{||}$ ), respectively.

359 invariant,  $J_3$  is found by integrating Eq. 1.4 over the complete particle orbit around  
 360 the Earth. The shape of this drift orbit is otherwise known as a drift shell. For  $J_3$ ,  
 361 the first term is negligible and the second term is the magnetic flux enclosed by the  
 362 drift shell,  $\Phi_m$  i.e.  $J_3 \sim \Phi_m$ .

363 Figure 1.3 from Schulz and Lanzerotti (1974) shows contours of the gyration,  
 364 bounce, and drift frequencies for electrons and protons in Earth's dipole magnetic  
 365 field.

Up until now we have considered the three periodic motions due Earth's magnetic field and the absence of electric fields. If  $\vec{E}$  is present, a particle's center of gyration i.e., averaged position of the particle over a gyration, will drift with a velocity perpendicular to both  $\vec{E}$  and  $\vec{B}$ . The drift velocity can be solved directly from Eq. 1.1 and is

$$\vec{v}_E = \frac{\vec{E} \times \vec{B}}{B^2}. \quad (1.11)$$

366 Lastly, for more detailed derivations of these motions, see the following texts:  
 367 Baumjohann and Treumann (1997); Schulz and Lanzerotti (1974); Tsurutani and  
 368 Lakhina (1997).

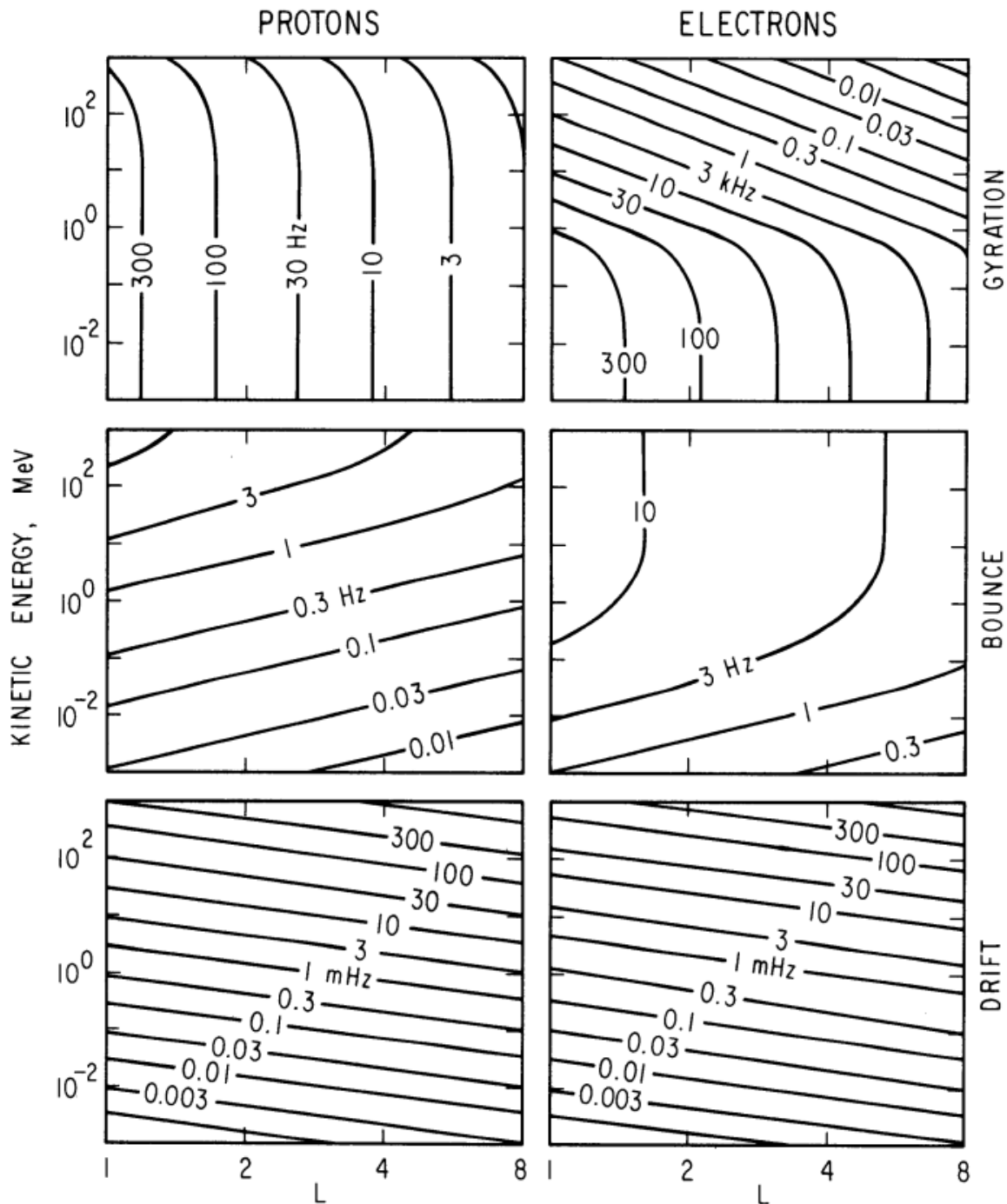


Figure 1.3: Contours of constant gyration, bounce, and drift frequencies for electrons and protons in a dipole field. Figure from Schulz and Lanzerotti (1974).

369        Particle Populations and Their Interractions in the Magnetosphere

370        The single-particle motion in Earth's magnetic field described in the previous  
371        section is a prerequisite to understanding how magnetospheric particles organize into  
372        macroscopic populations. The structure of the outer magnetosphere is shown in Fig.  
373        1.4 and inner magnetosphere in Fig. 1.5. In this section we will introduce the various  
374        particle populations in the magnetosphere and how they couple.

375        The sun and its solar wind are ultimately the source of energy input into the  
376        magnetosphere. The solar wind at Earth's orbit is a plasma traveling at supersonic  
377        speeds with an embedded interplanetary magnetic field (IMF). When the solar wind  
378        encounters Earth's magnetic field the plasma can not easily penetrate into the  
379        magnetosphere, rather it drapes around the magnetosphere forming a cavity in the  
380        solar wind that is roughly shaped as shown in Fig. 1.4. Because the solar wind is  
381        supersonic at 1 AU, a bow shock exists upstream of the magnetosphere. The solar  
382        wind plasma, after it is shocked by the bow shock, flows around the magnetosphere  
383        inside the magnetosheath. The surface where the solar wind ram pressure and Earth's  
384        magnetic pressure balance is termed the magnetopause, which can be thought of as  
385        a boundary between the solar wind's and Earth's plasma environments. This is  
386        a slightly naive description of the magnetopause, but is nonetheless an instructive  
387        conceptual picture. The shocked plasma then flows past the Earth where it shapes  
388        the magnetotail. In the magnetotail the solar wind magnetic pressure balances Earth's  
389        magnetic field pressure in the lobes. The magnetotail extends on the order of 100  
390         $R_E$  downstream of Earth [Add citation](#), and the tailward stretching of magnetic field  
391        lines creates the plasma sheet which exists in the region of low magnetic field strength  
392        near the magnetic equator [Add citation](#). The plasma sheet flows from dusk to dawn  
393        (out of the page in Figs. 1.4 and 1.5) and this current is connected to a zoo of other

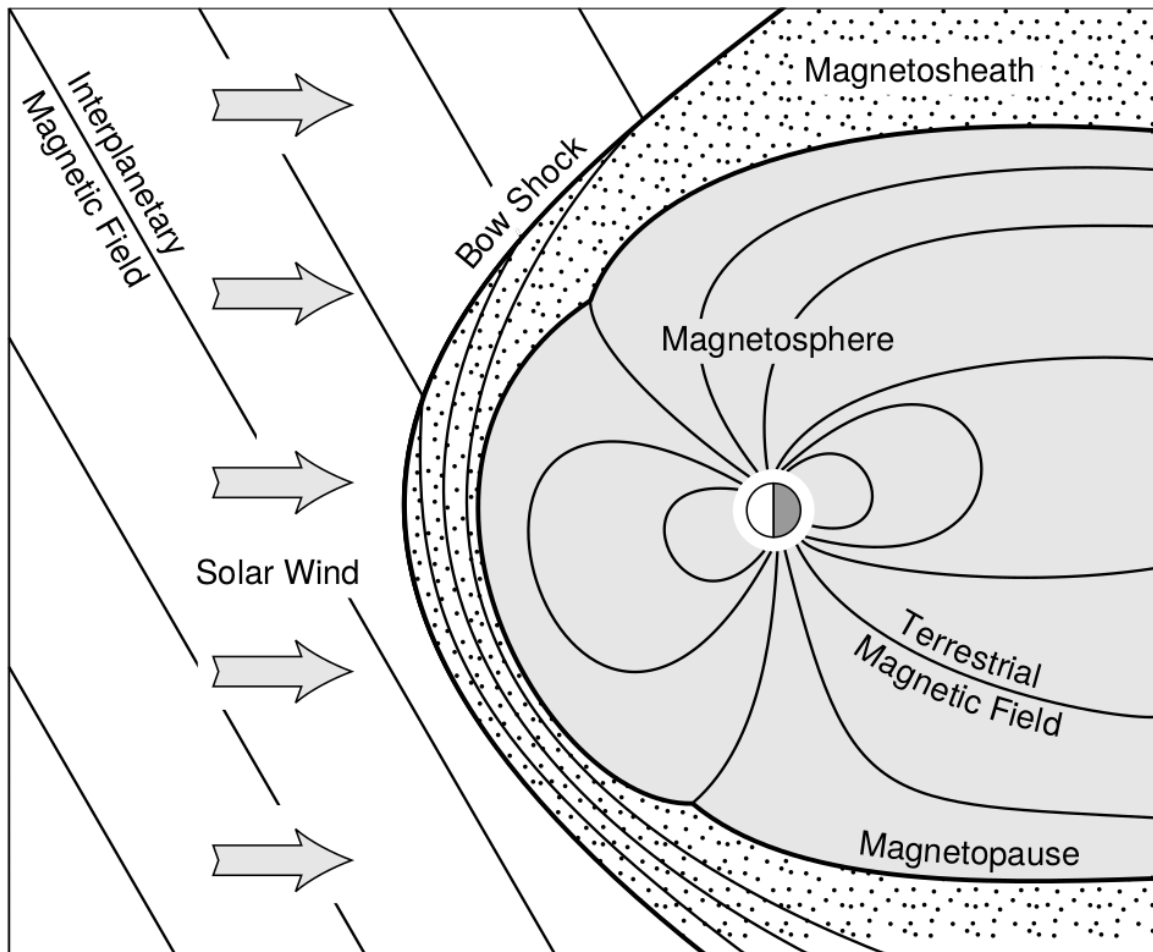


Figure 1.4: Macroscopic structures in the outer magnetosphere. The solar wind with its frozen-in interplanetary magnetic field is shown on the left and is traveling supersonically towards the right. The solar wind envelops Earth's magnetic field to create the magnetosphere cavity. Since the solar wind is traveling supersonically, it creates a bow shock up stream. Downstream of the bow shock the shocked solar wind plasma inside the magnetosheath flows around the magnetopause, a boundary between the solar wind and magnetosphere. Figure from Baumjohann and Treumann (1997).

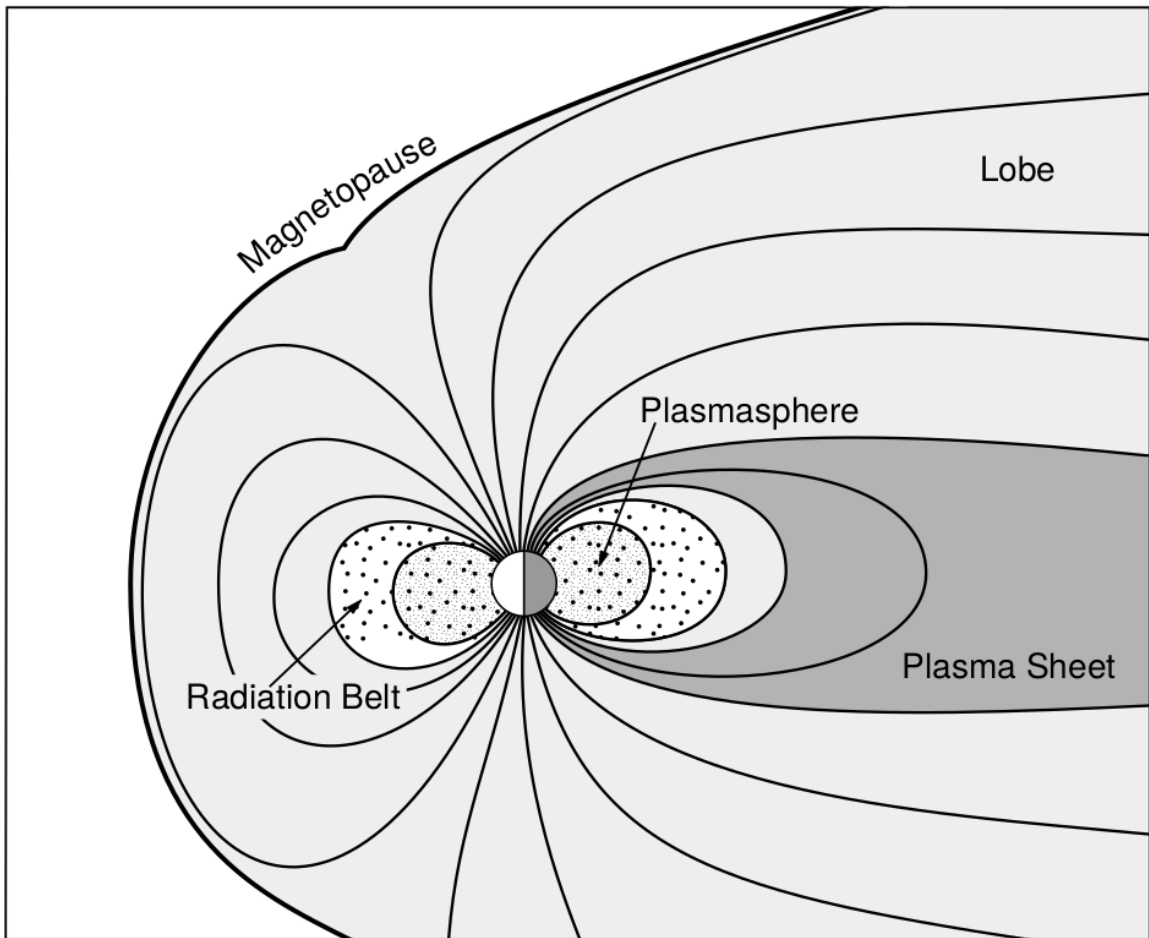


Figure 1.5: Macroscopic structures in the inner magnetosphere most relevant to this dissertation. The plasmasphere, and the radiation belts are shown and ring current is co-located there as well. Sun is to the left. Figure from Baumjohann and Treumann (1997).

394 currents in the magnetosphere which is beyond the scope of this dissertation.

395 The idea of the magnetopause as a barrier between the solar wind and  
 396 the magnetosphere is not entirely accurate due to the presence of reconnection.  
 397 Reconnection was first conceived by Dungey (1961) who described the convection of  
 398 Earth's magnetic field between the bow and tail regions of the magnetosphere. This  
 399 process is known as the Dungey cycle and is most effective when the IMF is pointing  
 400 southward as is shown in Fig. 1.6 part 1. As the IMF contacts Earth's magnetic  
 401 field it reconnects with it so that Earth's magnetic field is directly connected to the  
 402 IMF. Then as the solar wind flows tailward the IMF drags Earth's magnetic field  
 403 towards the magnetotail as shown in Fig. 1.6 parts 2-6. As more and more magnetic  
 404 field lines are draped in the magnetotail, magnetic pressure increases in the lobes  
 405 which squeezes the plasma sheet until Earth's magnetic field reconnects as is shown  
 406 in Fig. 1.6 part 7. Lastly, Fig. 1.6 part 8 shows the newly merged magnetic field  
 407 line and the plasma frozen on it moves Earthward under the magnetic tension force  
 408 to become more dipolar. This is called a dipolarization of the magnetic field, and the  
 409 plasma frozen on these field lines can be observed as injections (e.g. Turner et al.,  
 410 2015). Injection of plasma into the inner magnetosphere is one of the drivers of inner  
 411 magnetosphere dynamics. Should I talk about the K-H instability and how there  
 412 could be micro reconnection? i.e. cite a paper or two that support or refute that  
 413 idea.

#### 414 Inner Magnetosphere Populations

415 Before we describe the inner magnetosphere particle populations, we first need to  
 416 describe the coordinate system used to organize the inner magnetosphere populations.  
 417 The first coordinate was defined in section 1 and is the L shell. L shell can be thought  
 418 of as an analogue to a radius but in a dipole geometry. The azimuthal coordinate

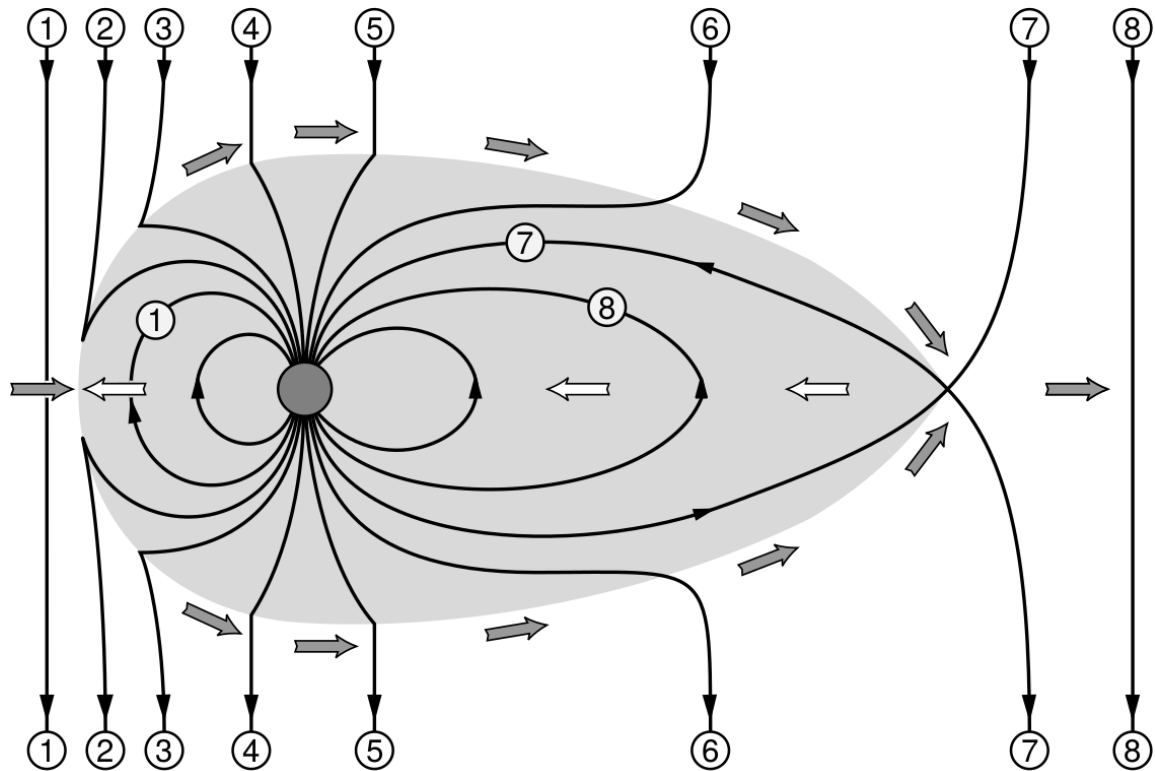


Figure 1.6: The series of steps involved in magnetic reconnection with a southward IMF. Figure from Baumjohann and Treumann (1997).

419 is the magnetic local time (MLT). For an observer above Earth's north pole looking  
 420 down, MLT is defined to be 0 (midnight) in the anti-sunward direction, and increases  
 421 in the counter-clockwise direction with 6 at dawn, 12 at noon (sunward direction),  
 422 and 18 in dusk. The last coordinate used in this dissertation is the magnetic latitude,  
 423  $\lambda$  which is analogous to the latitude coordinate and is defined to be 0 at the magnetic  
 424 equator.

425 The low energy particle dynamics in the inner magnetosphere are organized by  
 426 two electric fields: the co-rotation and the dawn-dusk electric fields. The co-rotation  
 427 electric field arises from the rotation of Earth's magnetic field. Since particles are  
 428 frozen on magnetic field lines and the plasma conductivity is effectively infinite, to  
 429 a non-rotating observer, Earth's rotation appears as a radial electric field that drops  
 430 off as  $\sim L^2$ . This electric field makes particles orbit around the Earth due to the  
 431  $\vec{E} \times \vec{B}$  drift. The other electric field, pointing from dawn to dusk is called the  
 432 convection electric field and is formed by the Earthward transport of particles from  
 433 the magnetotail that appears as an electric field to a stationary observer (with respect  
 434 to Earth). The superposition of the co-rotation and convection electric fields  
 435 results in a potential field shown in Fig. 1.7. The shaded area in Fig. 1.7 shows  
 436 the orbits on which low energy electrons are trapped, and outside are the untrapped  
 437 particles. The dynamic topology of the shaded region in Fig. 1.7 is controlled by only  
 438 the convection electric field which is dependent on the solar wind speed and the IMF.  
 439 The lowest energy particles, that are most effected by these electric fields, make up  
 440 the plasmasphere.

441 Plasmasphere The plasmasphere is a dense ( $n_e \sim 10^3/\text{cm}^3$ ), cool plasma  
 442 ( $\sim \text{eV}$ ) that extends to  $L \sim 4$  (extent is highly dependent on the solar wind and  
 443 magnetospheric conditions) and is sourced from the ionosphere. The two main

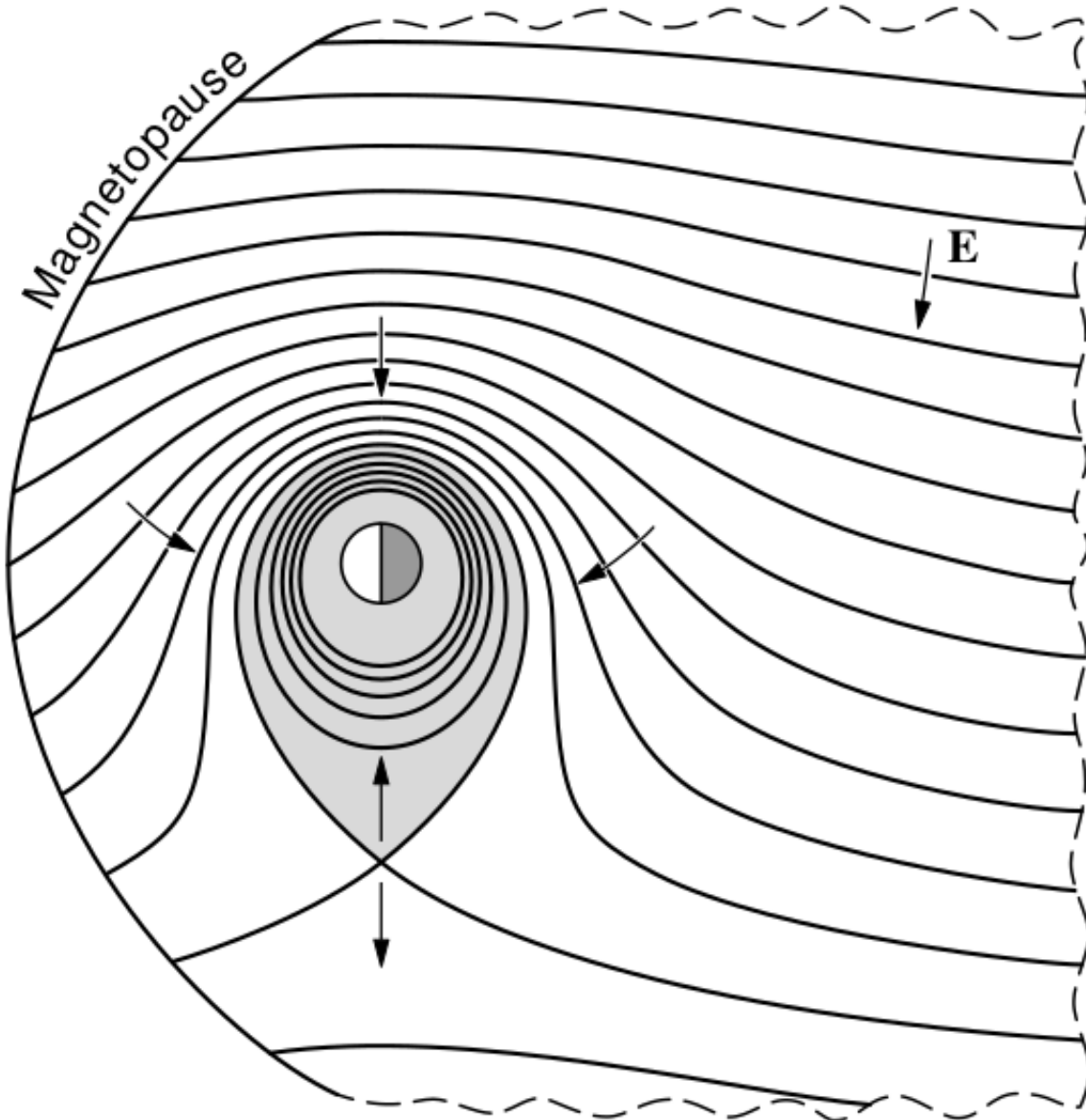


Figure 1.7: Equipotential lines and electric field arrows due to the superposition of the co-rotation and convection electric fields. Electrons in the shaded region execute closed orbits. Outside of the shaded regions the electrons are not trapped and will escape. The region separating the two regimes is called the Alfvén layer. Figure from Baumjohann and Treumann (1997).

444 mechanisms that source the cold plasma from the ionosphere are ultraviolet ionization  
 445 by sunlight and particle precipitation. The ultraviolet ionization by sunlight is  
 446 strongly dependent on the time of day (day vs night), latitude (more ionization near  
 447 the equator). The ionization due to particle precipitation, on the other hand, is highly  
 448 dependent on magnetospheric conditions, and mostly occurs at high latitudes.

449 The outer boundary of the plasmasphere is the plasmapause which is typically  
 450 identified as a steep radial gradient in plasma density from  $\sim 10^3/\text{cm}^3$  to  $\sim 1/\text{cm}^3$ . As  
 451 we will see throughout this dissertation, the location of the plasmapause is important  
 452 to model (e.g. O'Brien and Moldwin, 2003) and understand since the plasma density  
 453 strongly controls the efficiency of particle scattering (Horne et al., 2005).

454 Ring Current The next higher energy population is the ring current. This  
 455 population consists of protons and electrons between tens and a few hundred keV  
 456 that drift around the Earth. The orbits of higher energy particles are not as effected  
 457 by the convection and co-rotation electric field, rather they drift around the Earth  
 458 due to gradient and curvature drifts. Since the direction of the drift is dependent on  
 459 charge, protons drift west around the Earth and electrons drift East. This has the  
 460 effect of creating a current around the Earth.

461 The ring current generates a magnetic field which decreases the magnetic field  
 462 strength on Earth's surface and increases it outside of the ring current. The decrease  
 463 of Earth's magnetic field strength is readily observed by a system of ground-based  
 464 magnetometers and is merged into a Disturbance Storm Time (DST) index. An  
 465 example of a DST index time series from a coronal mass ejection (CME) driven 2015  
 466 St. Patrick's Day storm is shown in Fig. 1.8. The ring current is sometimes first  
 467 depleted and DST increases slightly (initial phase or sudden storm commencement).  
 468 Then the ring current is rapidly built up during which DST rapidly decreases (main

469 phase). Lastly the ring current gradually decays toward its equilibrium state over a  
 470 period of a few days and DST increases towards 0 (recovery phase). The DST index  
 471 along with other indicies are readily used by the space physics community to quantify  
 472 the global state of the magnetosphere.

473        Radiation Belts The highest energy particle populations are in the Van Allen  
 474 radiation belts. These belts were discovered by Van Allen (1959) and Vernov and  
 475 Chudakov (1960) during the Cold War and are a pair of toroidally shaped populations  
 476 of trapped electrons and protons usually within to  $L < 8$  and are shown in Fig. 1.9.  
 477 Their quiescent toroidal shape is similar to the shape of the plasmasphere and ring  
 478 current and is a result of Earth's dipole magnetic field and the conservation of the  
 479 three adiabatic invariants discussed in section 1.

480        The inner radiation belt is extremely stable on time periods of years, extends  
 481 to  $L \approx 2$ , and mainly consists of protons with energies between MeV and GeV and  
 482 electrons with energies up to  $\approx 1$  MeV (Claudepierre et al., 2019). The source of  
 483 inner radiation belt protons is believed to be due to cosmic-ray albedo neutron decay  
 484 (e.g. Li et al., 2017) and inward radial diffusion for electrons (e.g. O'Brien et al.,  
 485 2016). The gap between the inner and outer radiation belt is called the slot, which is  
 486 believed to be due to hiss waves inside the plasmasphere (described below) scattering  
 487 particles into the atmosphere (e.g. Breneman et al., 2015; Lyons and Thorne, 1973).

488        The outer radiation belt, on the other hand is much more dynamic and consists  
 489 of mainly electrons of energies up to a few MeV. The outer belt's spatial extent is  
 490 highly variable e.g. see Fig. 1.10, and is typically observed at  $4 < L < 8$ . Since  
 491 the outer radiation belt contains a dynamic population of energetic particles that  
 492 pose a threat to human and technological presence in Earth's atmosphere and space,  
 493 decades of research has been undertaken to understand and predict the outer radiation

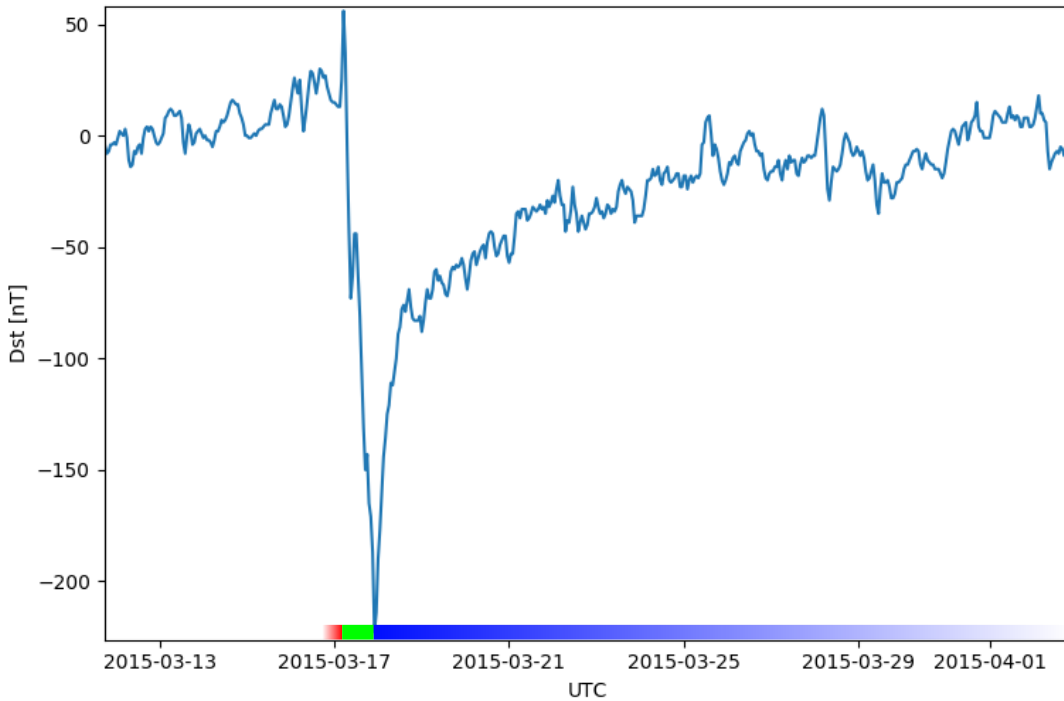


Figure 1.8: The DST index during the St. Patrick's Day 2015 storm. This storm was caused by a coronal mass ejection on March 15th, 2015. The storm phases are: initial phase, main phase, and recovery phase. The initial phase occurred when the Dst peaked at +50 nT on March 17th during which the ring current was eroded by the coronal mass ejection during the interval shown by the red bar. Then the rapid decrease to  $\approx -200$  nT was during the main phase where many injections from the magnetotail pumped up the ring current which reduced Earth's magnetic field strength at the ground and is shown with the green bar. Lastly, the recovery phase lasted from March 18th to approximately March 29th during which the ring current particles were lost and the ring current returned to its equilibrium state. The recovery phase is shown with the blue bar.

## The Earth's Electron Radiation Belts

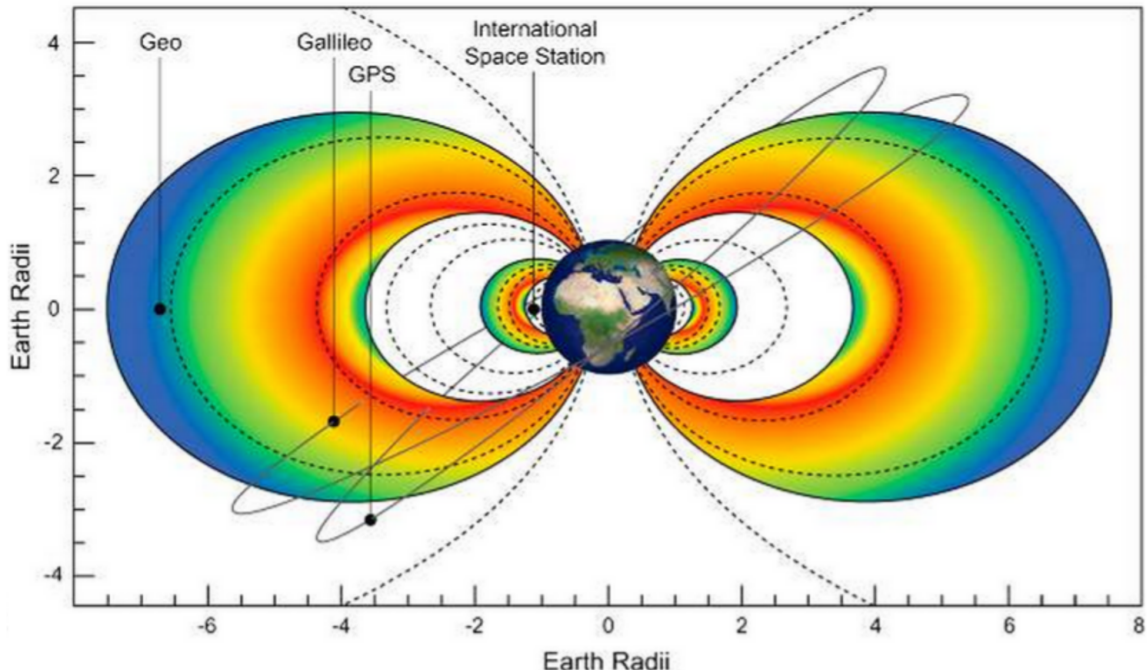


Figure 1.9: The two radiation belts with the locations of various satellites.  
Figure from (Horne et al., 2013).

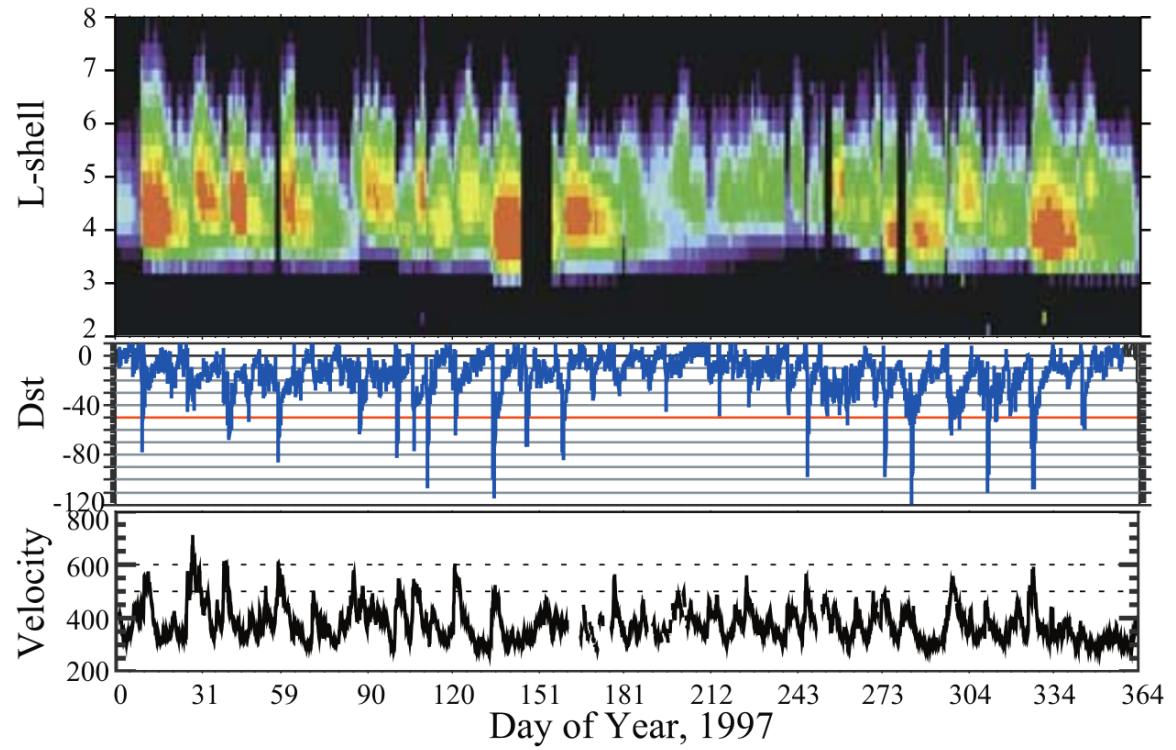


Figure 1.10: The dynamics of the outer radiation belt in 1997 from the POLAR satellite. Top panel shows the 1.2-2.4 MeV electron flux as a function of L and 1997 day of year. The middle panel shows the DST index, and bottom panel shows the solar wind velocity. Figure from (Reeves et al., 2003).

494 belt particles, waves, and wave-particle interactions. The dynamics of the outer  
 495 radiation belt can be understood by considering various competing acceleration and  
 496 loss mechanisms which will be described in the following sections.

497 Radiation Belt Particle Sources and Sinks

498 Adiabatic Heating

499 One of the particle heating and transport mechanisms arises from the Earthward  
 500 convection of particles. The conservation of  $J_1$  implies that the initial and final  $v_\perp$   
 501 depends on the change in the magnetic field amplitude

$$\frac{v_{\perp i}^2}{B_i} = \frac{v_{\perp f}^2}{B_f}. \quad (1.12)$$

502 As a particle convects Earthward,  $B_f > B_i$  thus  $v_\perp$  must increase. The dipole  
 503 magnetic field amplitude can be written as

$$B(L, \theta) = \frac{31.2 \mu\text{T}}{L^3} \sqrt{1 + 3 \cos^2 \theta} \quad (1.13)$$

504 which implies that

$$\frac{v_{\perp f}^2}{v_{\perp i}^2} = \left( \frac{L_i}{L_f} \right)^3. \quad (1.14)$$

505 .

506 In addition, as the particle convects Earthward the distance between the  
 507 particle's mirror points decrease. If  $J_2$  is conserved, the shrinking bounce path implies  
 508 that  $v_{||}$  must increase by

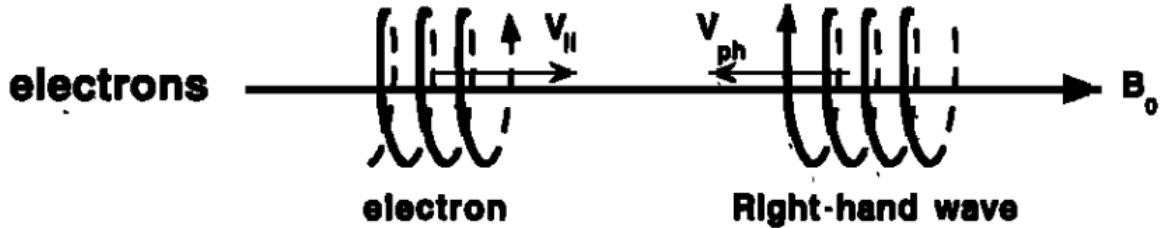
$$\frac{v_{|| f}^2}{v_{|| i}^2} = \left( \frac{L_i}{L_f} \right)^k \quad (1.15)$$

509 where  $k$  ranges from 2 for equatorial pitch angles,  $\alpha_{eq} = 0^\circ$ , to 2.5 for  $\alpha_{eq} = 90^\circ$   
 510 (Baumjohann and Treumann, 1997). Since the rate of adiabatic heating is greater in  
 511 the perpendicular direction than heating in the parallel direction, an initially isotropic  
 512 particle distribution will become anisotropic during its convection. These isotropic  
 513 particles can then become unstable to wave growth and generate waves in order to  
 514 reach equilibrium.

515 Wave Resonance Heating

516 Another mechanism that heats particles is due to particles resonating with  
 517 plasma waves. A few of the electromagnetic wave modes responsible for particle  
 518 acceleration (and deceleration) relevant to radiation belt dynamics are hiss, whistler  
 519 mode chorus (chorus), and electromagnetic ion cyclotron (EMIC) waves. These waves  
 520 are created by the loss cone instability that driven by an anisotropy of electrons  
 521 for chorus waves, and protons for EMIC waves. The level of anisotropy can be  
 522 quantified by the ratio of the perpendicular to parallel particle temperatures ( $T_\perp/T_{||}$ ).  
 523 A particle distribution is unstable when  $T_\perp/T_{||} > 1$  which facilitates wave growth.  
 524 Since electrons gyrate in a right-handed sense, the chorus waves also tend to be right  
 525 hand circularly polarized (Tsurutani and Lakhina, 1997). The same argument applies  
 526 to protons and left hand circularly polarized EMIC waves as well.

527 These circularly polarized waves can resonate with electrons and/or protons  
 528 when their combined motion results in a static  $\vec{E}$ . One example of a resonance  
 529 between a right hand circularly polarized wave and an electron is shown in Fig. 1.21  
 530 and is termed the cyclotron resonance. An electron's  $v_{||}$  and the wave's parallel wave  
 531 vector,  $k_{||}$  are in opposite directions such that the wave frequency  $\omega$  is Doppler shifted  
 532 to an integer multiple of the  $\Omega_e$  at which point the electron feels a static electric  
 533 field and is accelerated or decelerated. This acceleration happens when a resonance



$$\omega + \mathbf{k}_{\parallel} \mathbf{V}_{\parallel} = \Omega^-$$

Figure 1.11: The trajectories of an electron and a right-hand circularly polarized wave during a cyclotron resonance. The electron's  $v_{\parallel}$  and the wave's  $k_{\parallel}$  are in opposite directions such that the wave's frequency is Doppler shifted to an integer multiple of the electron cyclotron frequency. Figure from (Tsurutani and Lakhina, 1997).

534 condition is satisfied between a wave and a particle for which we will now derive an  
 535 illustrative toy model.

536 Assume a uniform magnetic field  $\vec{B} = B_0 \hat{z}$  with a parallel propagating ( $k = k \hat{z}$ ),  
 537 right-hand circularly polarized wave. The wave's electric field as a function of position  
 538 and time can be written as

$$\vec{E} = E_0 (\cos(\omega t - kz) \hat{x} + \sin(\omega t - kz) \hat{y}) \quad (1.16)$$

which is more clearly expressed by taking the dot product to find  $\vec{E}$  in the  $\hat{\theta}$  direction

$$E_{\theta} = \vec{E} \times \hat{\theta} = E_0 \cos(\omega t - kz + \theta). \quad (1.17)$$

539 Now assume that the electron is traveling in the  $-\hat{z}$  direction with a velocity  $\vec{v} = -v_0 \hat{z}$   
 540 so its time dependent position along  $\hat{z}$  is

$$z(t) = -v_0 t \quad (1.18)$$

541 and gyrophase is

$$\theta(t) = -\Omega t + \theta(0) \quad (1.19)$$

542 where the first negative sign comes from the electron's negative charge. Now we put  
543 this all together and express the electric field and the force that the electron will  
544 experience

$$m \frac{dv_\theta}{dt} = qE_\theta = qE_0 \sin((\omega + kv_0 - \Omega)t + \theta(0)). \quad (1.20)$$

545 This is a relatively complex expression, but when the time dependent component,

$$\omega + kv_0 - \Omega = 0, \quad (1.21)$$

546 the electron will be in a static electric field which will accelerate or decelerate the  
547 electron depending on  $\theta_0$ , the phase between the wave and the electron. **Show Bortnik**  
548 **2008 plot?** The expression in Eq. 1.21 is commonly referred to as the resonance  
549 condition and is more generally written as

$$\omega - k_{||}v_{||} = \frac{n\Omega_e}{\gamma} \quad (1.22)$$

550 where  $n$  is the resonance order, and  $\gamma$  is the relativistic correction (e.g. Millan and  
551 Thorne, 2007). In the case of the cyclotron resonance,  $\omega \approx \Omega_e$  thus  $J_1$  is violated.  
552 Since  $J_1$  is violated,  $J_2$  and  $J_3$  are also violated since the conditions required to  
553 violate  $J_2$  and  $J_3$  are less stringent than  $J_1$ . It is important to remember that along  
554 the particle's orbit it will encounter and experience the effects of many waves along  
555 its orbit. The typical MLT extent of a handful of waves that are capable of resonating  
556 with radiation belt electrons are shown in Fig. 1.12.

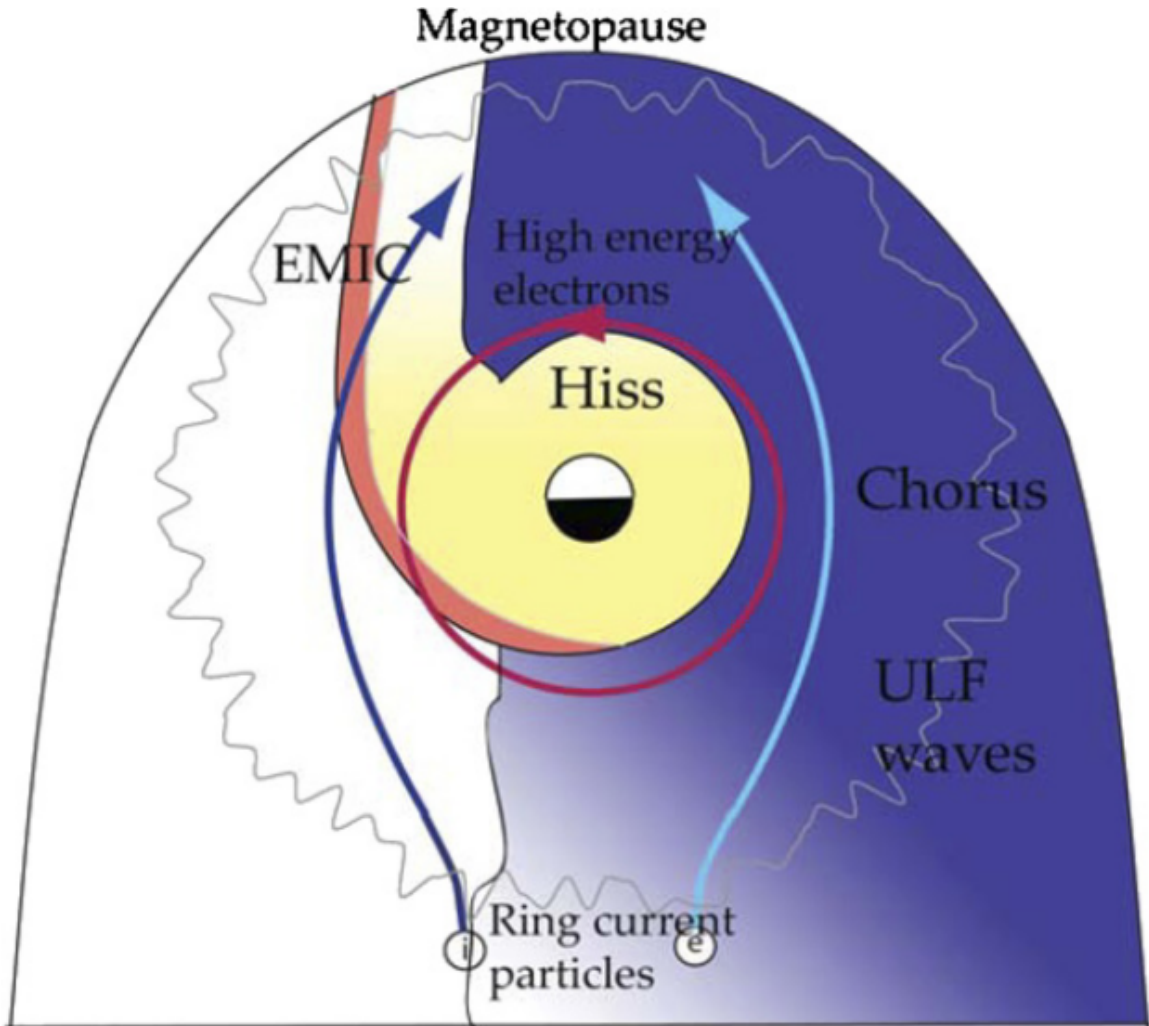


Figure 1.12: Various wave modes in the magnetosphere. Ultra low frequency waves occur through the magnetosphere. Chorus waves are typically observed in the 0-12 midnight-dawn region. EMIC waves are typically observed in the dusk MLT sector. Hiss waves are observed inside the plasmasphere. Figure from Millan and Thorne (2007).

557 Particle Losses

558 Now that we have seen two general mechanisms with which particles are  
 559 accelerated and transported in the magnetosphere, we will now consider a few  
 560 specific mechanisms with which particles are lost to the atmosphere or the solar  
 561 wind. One particle loss mechanism into the solar wind is magnetopause shadowing  
 562 (e.g. Ukhorskiy et al., 2006). Particles are sometimes lost when the ring current is  
 563 strengthened and Earth's magnetic field strength is increased outside of the ring  
 564 current (and reduced on Earth's surface). If the time scale of the ring current  
 565 strengthening is slower than a particle drift,  $J_3$  is conserved. Then in order to  
 566 conserve  $J_3$  while the magnetic field strength is increased, the particle's drift shell  
 567 must move outward to conserve the magnetic flux contained by the drift shell. Then  
 568 if the particle's drift shell expands to the point that it crosses the magnetopause, the  
 569 particle will be lost to the solar wind.

570 **Move to acceleration?** Another particle loss and acceleration mechanism is driven  
 571 by ultra low frequency (ULF) waves and is called radial diffusion. Radial diffusion is  
 572 the transport of particles from high to low phase space density,  $f$ . If the transport is  
 573 radially inward, particles will appear to be accelerated. On the other hand, radially  
 574 outward radial diffusion can transport particles through the magnetopause where  
 575 they will be lost to the solar wind. Reeves et al. (2013) investigated the driver of  
 576 particle acceleration during the October 2012 storm and observationally found that  
 577 inward radial diffusion was not dominant, rather local acceleration via wave-resonance  
 578 heating (i.e. particle diffusion in pitch angle and energy which will be described below)  
 579 appeared to be the dominant acceleration mechanism.

580 The loss mechanism central to this dissertation is pitch angle and energy  
 581 scattering of electrons by waves. Some of the waves that scatter electrons in energy  
 582 and pitch angle in the inner magnetosphere are: plasmaspheric hiss (e.g. Breneman

583 et al., 2015; O'Brien et al., 2014), EMIC waves (e.g. Capannolo et al., 2019; Hendry  
 584 et al., 2017), and chorus waves (e.g. Breneman et al., 2017; Kasahara et al., 2018;  
 585 Ozaki et al., 2019). These wave-particle interactions occur when the resonance  
 586 condition in Eq. 1.22 is satisfied at which point the particle's energy and  $\alpha$  is modified  
 587 by the wave. More details regarding the theory of pitch angle and energy diffusion is  
 588 given in Chapter X. If the wave changes  $\alpha$  towards 0 such that  $\alpha < \alpha_{LC}$ , the particle's  
 589 mirror point lowers to less than 100 km altitude where the particle can be lost due  
 590 collisions with air. One manifestation of pitch angle scattering of particles into the  
 591 loss cone are microbursts: a sub-second durtaison impulse of electrons.

592

### Microbursts

593 Microbursts were first identified in high altitude balloon observations of bremsstrahlung  
 594 X-rays emitted by microburst electrons impacting the atmosphere by Anderson and  
 595 Milton (1964). Since then, other balloons have observed microburst X-ray signatures  
 596 in the upper atmosphere (e.g. Anderson et al., 2017; Barcus et al., 1966; Brown et al.,  
 597 1965; Parks, 1967; Trefall et al., 1966; Woodger et al., 2015). In addition to their X-ray  
 598 signature, microbursts electrons have been directly observed in LEO with spacecraft  
 599 including the Solar Anomalous and Magnetospheric Particle Explorer (SAMPEX),  
 600 Focused Investigation of Relativistic Electron Bursts: Intensity, Range, and Dynamics  
 601 II (FIREBIRD-II), Science Technologies Satellite (STSAT-I) (e.g. Blake et al., 1996;  
 602 Blum et al., 2015; Breneman et al., 2017; Crew et al., 2016; Lee et al., 2012, 2005;  
 603 Lorentzen et al., 2001a,b; Nakamura et al., 1995, 2000; O'Brien et al., 2004, 2003).  
 604 An example microburst time series is shown in Fig. 1.13 and was observed by  
 605 Montana State University's (MSU) FIREBIRD-II CubeSats. The prominent features  
 606 of microbursts in Fig. 1.13 are their  $\pm 1$  second duration, half order of magnitude  
 607 increase in count rate above the falling background, and their approximately 200-800

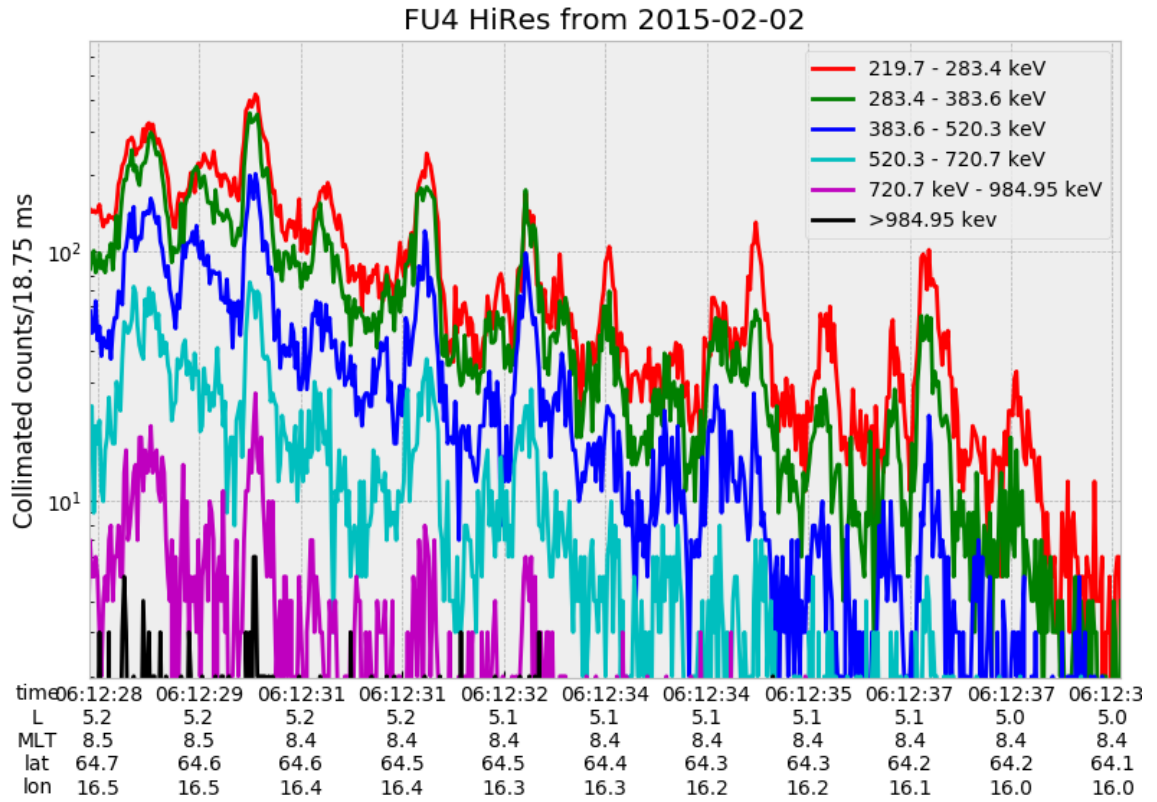


Figure 1.13: An example train of microbursts observed by FIREBIRD-II unit 4 on February 2nd, 2015. The colored curves show the differential energy channel count rates in six channels from  $\approx 200$  keV to greater than 1 MeV. The x-axis labels show auxiliary information such as time of observation and the spacecraft position in L, MLT, latitude and longitude coordinates.

608 keV energy extent.

609 Microbursts are observed on magnetic field footprints that are connected to the  
 610 outer radiation belt (approximately  $4 < L < 8$ ), and are predominately observed in  
 611 the 0-12 MLT sector with an elevated occurrence frequency during magnetospherically  
 612 disturbed times as shown in Fig. 1.14. Microbursts have been previously observed  
 613 over a wide energy range from a few tens of keV (Datta et al., 1997; Parks, 1967) to  
 614 greater than 1 MeV (e.g. Blake et al., 1996; Greeley et al., 2019). The microburst

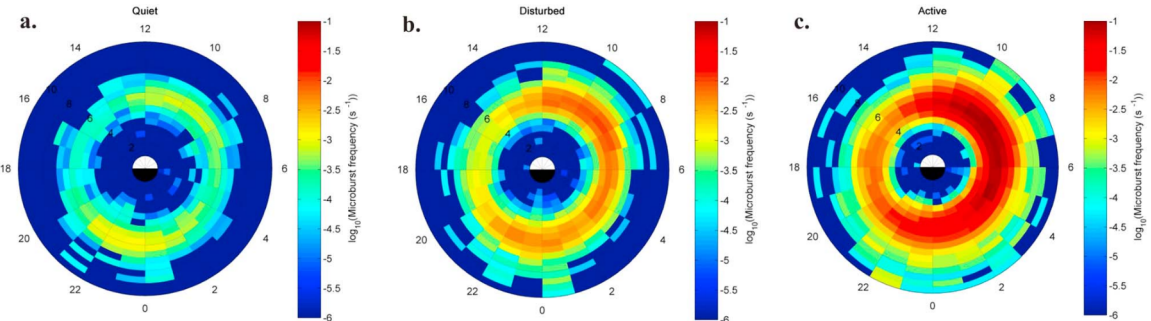


Figure 1.14: Relativistic ( $> 1\text{MeV}$ ) distribution of microburst occurrence rates as a function of  $L$  and MLT. The three panels show the microburst occurrence rate dependence on geomagnetic activity, parameterized by the auroral electrojet (AE) index for (a)  $\text{AE} < 100 \text{nT}$ , (b)  $100 < \text{AE} < 300 \text{nT}$  and (c)  $\text{AE} > 300 \text{nT}$ . Figure from Douma et al. (2017).

615 electron flux ( $J$ ) falls off in energy, and the microburst energy spectra is typically  
 616 well fit to a decaying exponential

$$J(E) = J_0 e^{-E/E_0} \quad (1.23)$$

617 where  $J_0$  is the flux at 0 keV (unphysical free parameter) and  $E_0$  quantifies the  
 618 efficiency of the scattering mechanism in energy (.e.g Datta et al., 1997; Lee et al.,  
 619 2005; Parks, 1967). A small  $E_0$  suggests that mostly low energy particles are scattered  
 620 and a high  $E_0$  suggests that the scattering mechanism scatters low and high energy  
 621 electrons. Reality is a bit more messy and a high  $E_0$  may be a signature of a scattering  
 622 mechanism preferential to high energy electrons, but is hidden by the convolution of  
 623 the source particles available to be scattered (typically with a falling energy spectrum)  
 624 and the energy-dependent scattering efficiency.

625 The short duration of microbursts observed by a single LEO satellite has an  
 626 ambiguity when interpreting what is exactly a microburst. The two possible realities  
 627 are: a microburst is very small and spatially stationary so that the LEO spacecraft

628 passes through it in less than a second. Alternatively, microbursts are spatially large  
 629 with a short duration such that the microburst passes by the spacecraft in a fraction  
 630 of a second. There are a few ways to distinguish between the two possible realities,  
 631 and each one has a unique set of advantages.

632 A high altitude balloon provides essentially a stationary view of the precipitating  
 633 particles under the radiation belt footprints so a short-lived, temporal microburst  
 634 can be unambiguously identified. Spatial structures on the other hand are difficult  
 635 to identify because a balloon is essentially still on drift timescales thus a variation in  
 636 the X-rays can be due to the spatial structure or an increase of precipitating particles  
 637 over the whole area. Furthermore, if the stationary structure is drifting its particles  
 638 are not precipitating into the atmosphere so there is no X-ray signature.

639 Another solution is multi-spacecraft missions that can determine if a microburst  
 640 is spatial or temporal. As will be shown in this dissertation, if a microburst is  
 641 observed simultaneously by two spacecraft then it is temporally transient and has  
 642 a size greater than the spacecraft separation. On the other hand, if two spacecraft  
 643 observe a microburst-like feature in the same location and at different times, then it is  
 644 spatial may be a curtain (Blake and O'Brien, 2016). Both observational methods have  
 645 a unique set of strengths, and this dissertation takes the multi-spacecraft approach  
 646 to identify and study microbursts.

647

### Scope of Research

648 This dissertation furthers our understanding of the microburst scattering  
 649 mechanism by observing the scattering directly, and measuring the microburst sizes  
 650 and comparing them to the size of waves near the magnetic equator where those  
 651 electrons could have been scattered. Chapter X describes a microburst scattering  
 652 event observed by NASA's Van Allen Probes which was studied in the theoretic

653 framework of pitch angle and energy diffusion. The following two chapters will then  
654 study the size of microbursts. Chapter Y describes a bouncing packet microburst  
655 observation made by MSU's FIREBIRD-II mission where the microburst's lower  
656 bound longitudinal and latitudinal sizes were estimated. Then Chapter Z expands  
657 the case study from Ch. Y to a statistical study of microburst sizes using The  
658 Aerospace Corporation's AeroCube-6 (AC6) CubeSats. In this study, a Monte Carlo  
659 and analytic microburst size models were developed to account for the compounding  
660 effects of random microburst sizes and locations. Lastly, Ch. A will summarize the  
661 dissertation work and make concluding remarks regarding outstanding questions in  
662 microburst physics.

663

## CHAPTER TWO

664

EVIDENCE OF MICROBURSTS OBSERVED NEAR THE EQUATORIAL

665

PLANE IN THE OUTER VAN ALLEN RADIATION BELT

666

Contribution of Authors and Co-Authors

667 Manuscript(s) in Chapter(s) 1

668

669 Author: [type author name here]

670 Contributions: [list contributions here, single-spaced]

671 Co-Author: [type co-author name here]

672 Contributions: [list contributions here, single-spaced]

673 Co-Author: [type co-author name here]

674 Contributions: [list contributions here, single-spaced]

675

676

Manuscript Information

677 [Type Author and Co-author(s) Names Here]

678 Geophysical Research Letters

679 Status of Manuscript: Published in a peer-reviewed journal

680 Wiley

681 Volume 45, Issue 16

682

Key Points

- 683     ● First report of direct observation of microbursts at high altitude, near the  
 684       equatorial plane.
- 685     ● Microbursts' duration, flux enhancement, and energy spectra are similar to prior  
 686       observations in LEO.
- 687     ● Microburst generation is not consistent with a single quasi-linear gyroresonant  
 688       interaction with chorus waves.

689

Abstract

690     We present the first evidence of electron microbursts observed near the equatorial  
 691       plane in Earth's outer radiation belt. We observed the microbursts on March 31st,  
 692       2017 with the Magnetic Electron Ion Spectrometer and RBSP Ion Composition  
 693       Experiment on the Van Allen Probes. Microburst electrons with kinetic energies  
 694       of 29-92 keV were scattered over a substantial range of pitch angles, and over time  
 695       intervals of 150-500 ms. Furthermore, the microbursts arrived without dispersion in  
 696       energy, indicating that they were recently scattered near the spacecraft. We have  
 697       applied the relativistic theory of wave-particle resonant diffusion to the calculated  
 698       phase space density, revealing that the observed transport of microburst electrons is  
 699       not consistent with the hypothesized quasi-linear approximation.

700

Introduction

701     Since the Van Allen radiation belts were discovered by Van Allen (1959) and  
 702       Vernov and Chudakov (1960), decades of work has focused on understanding their  
 703       origins and effects on the near-Earth space environment and ionosphere-thermosphere

704 system. The energy content of the outer belt is dominated by energetic electrons,  
 705 with dynamics controlled by a complex interplay between various source and loss  
 706 mechanisms. One important loss and acceleration mechanism is gyroresonant  
 707 diffusion in energy and pitch angle (PA) due to scattering of electrons by plasma  
 708 waves (e.g. Bortnik et al., 2008; Horne and Thorne, 2003; Meredith et al., 2002;  
 709 Millan and Thorne, 2007; Summers et al., 1998; Thorne and Andreoli, 1981; Thorne  
 710 et al., 2005; Walker, 1993).

711 Chorus waves are commonly associated with PA and energy diffusion. These  
 712 waves are typically generated by substorm injections into the inner magnetosphere,  
 713 which lead to a temperature anisotropy of the source electrons with energies up to  
 714 tens of keV (e.g. Horne et al., 2003; Li et al., 2009a). Since these source electrons  
 715 drift eastward, chorus is most frequently observed in the dawn sector, but it has  
 716 been observed at all magnetic local times (MLT) (Li et al., 2009b). Chorus waves  
 717 are believed to generate electron microburst precipitation through wave-particle  
 718 interactions.

719 Microbursts are typically defined as an increase of electron flux in or near the  
 720 atmospheric loss cone that last < 1 s (e.g. Anderson and Milton, 1964; Blake et al.,  
 721 1996; Lorentzen et al., 2001a). Empirical and theoretical analyses indicate that  
 722 microbursts are an important loss process since they can substantially deplete the  
 723 radiation belt electrons on the order of one day (e.g. Breneman et al., 2017; Lorentzen  
 724 et al., 2001b; O'Brien et al., 2004; Thorne et al., 2005). Previously, microbursts have  
 725 been observed in the upper atmosphere in the form of bremsstrahlung X-rays (e.g.  
 726 Anderson et al., 2017; Parks, 1967; Woodger et al., 2015) and directly in low Earth  
 727 orbit (LEO) (e.g. Blake et al., 1996; Blum et al., 2015; Breneman et al., 2017; Crew  
 728 et al., 2016; Lee et al., 2012, 2005; Lorentzen et al., 2001a,b; Mozer et al., 2018;  
 729 Nakamura et al., 1995, 2000; O'Brien et al., 2004, 2003).

730 We observed for the first time, microburst-like signatures near their hypothesized  
 731 origin within the heart of the outer radiation belt. The unique microburst  
 732 observations we report here were possible with the Van Allen Probe-A's (RBSP-  
 733 A) Magnetic Electron Ion Spectrometer's (MagEIS) fast sampling rate ( $\sim$ 11 ms),  
 734 and RBSP Ion Composition Experiment's (RBSPICE) PA coverage. The observed  
 735 microbursts' duration, energy spectra, and energy dispersion signature were similar to  
 736 microbursts previously reported from LEO. Furthermore, we simultaneously observed  
 737 structureless "hiss-like" whistler mode wave power in the lower band chorus frequency  
 738 range (Li et al., 2012). From previous observations in LEO (e.g. Blake et al., 1996),  
 739 it is believed that microbursts result from the impulsive scattering of electrons into  
 740 or near the loss cone, which is on the order of a few tens of degrees in LEO. With this  
 741 assumption, high altitude microburst observations near the magnetic equator should  
 742 be very difficult to make since the atmospheric loss cone there is only a few degrees  
 743 wide. Thus, the loss cone is smaller than the angular resolution of most particle  
 744 detectors. Even when an instrument is observing the loss cone, the instrument's field  
 745 of view will include some portion of the trapped population. The trapped electron flux  
 746 is typically orders of magnitude higher than that in the loss cone, so that microbursts  
 747 scattered into the loss cone will be obscured. We present observational evidence that  
 748 suggests that the sudden impulse of electrons studied here is consistent with the  
 749 creation of microbursts. Furthermore, these microbursts were scattered over a broad  
 750 PA range outside of the loss cone, though the loss cone was not directly observed by  
 751 MagEIS and RBSICE.

752 This paper explores the properties of the observed microbursts by utilizing in-  
 753 situ RBSP measurements of waves and particles. This unique high altitude point of  
 754 view enables us to test whether the observed microburst scattering is consistent with  
 755 a quasi-linear diffusion process. We have tested this hypothesis with in-situ electron

756 phase space density (PSD) measurements and the relativistic theory of wave-particle  
 757 resonant diffusion (Summers et al., 1998; Walker, 1993) to determine if the microburst  
 758 electrons diffused in PA and energy.

759 Spacecraft Instrumentation

760 NASA's RBSP mission (Mauk et al., 2013), launched on August 30th, 2012,  
 761 consists of a pair of identically instrumented spacecraft. Their orbit and instru-  
 762 mentation are uniquely configured to enrich our understanding of the particles and  
 763 waves in the inner magnetosphere. The RBSP spacecraft are in highly elliptical, low-  
 764 inclination orbit, with perigee of  $\sim$ 600 km and apogee of  $\sim$ 30,000 km altitude. Their  
 765 attitude is maintained by spin-stabilization with a period of  $\sim$ 11 s and the spin axis is  
 766 roughly sun-pointing. In this analysis, energetic electron measurements from MagEIS  
 767 (Blake et al., 2013) and RBSPICE (Mitchell et al., 2013) were used, complemented by  
 768 magnetic field and wave measurements from Electric and Magnetic Field Instrument  
 769 and Integrated Science (EMFISIS) (Kletzing et al., 2013).

770 We observed these microbursts with RBSP-A's MagEIS low energy instrument  
 771 (MagEIS-A) which measures 20-240 keV electrons. It has an angular acceptance  
 772 of  $3^\circ - 10^\circ$  in the spacecraft spin plane, and  $20^\circ$  perpendicular to the spin plane.  
 773 MagEIS-A has a high rate data mode which samples at 1000 angular sectors per  
 774 spacecraft spin (11 ms cadence). MagEIS low on RBSP-B on the other hand samples  
 775 at 64 angular sectors per spacecraft spin (172 ms cadence), so it was only used for  
 776 context.

777 To expand the PA coverage of MagEIS-A, we used the RBSPICE-A time-of-  
 778 flight instrument. RBSPICE-A measures electron energies in the range of 19 keV -  
 779 1 MeV with a fan of six telescopes (the sixth telescope is used only for calibration  
 780 and was excluded from this analysis). These telescopes have an overall acceptance

781 angle of  $160^\circ$  by  $12^\circ$  which allows them to simultaneously sample a substantial part  
 782 of the Pitch Angle Distribution (PAD). RBSPICE-A gathers data over 32 sectors  
 783 per spacecraft spin ( $\approx 310$  ms cadence) and each sector is divided into three sub-  
 784 sectors corresponding to three measurement modes (Manweiler and Zwiener, 2018).  
 785 At the time of the observation, the sub-sector used for electron measurements had  
 786 an accumulation time of 77 ms. We used RBSPICE-A's Electron Basic Rate (EBR)  
 787 telemetry data in this analysis which is not averaged, though it is an integral energy  
 788 channel.

789 To understand the dynamics of the local magnetic field, we used the EMFISIS  
 790 instrument. EMFISIS provides measurements of the DC magnetic field with flux gate  
 791 magnetometers. In addition, it measures electromagnetic waves from 10 Hz to 500  
 792 kHz with search coil magnetometers. The spectral matrix and burst data products  
 793 used in this analysis were from the EMFISIS waveform receiver (WFR) (10 Hz - 12  
 794 kHz) and the high frequency receiver (10 kHz - 500 kHz). Burst data were selectively  
 795 captured at a 35 kHz sample rate, and the survey mode spectral matrix data was  
 796 captured every 6s.

797

### Observations

798 MagEIS-A and RBSPICE-A observed the microburst-like signatures on March  
 799 31st, 2017 at  $L^* \approx 6$  and  $MLT \approx 19$ , calculated with the Tsyganenko 2004 magnetic  
 800 field model (Tsyganenko and Sitnov, 2005). The magnetosphere was in the recovery  
 801 phase of a storm, with minimum Dst of -75 nT observed on March 27th. The local  
 802 electron number density was on the order of  $1 \text{ cm}^{-3}$  at this time, so both RBSP  
 803 spacecraft were located outside the plasmasphere. The two spacecraft were separated  
 804 by 1700 km, at magnetic latitudes  $\lambda \approx -19^\circ$  and  $\lambda \approx -18^\circ$  for RBSP-A and RBSP-B,  
 805 respectively.

806 MagEIS-A observed microburst electron flux ( $J$ ) at energies  $\geq 92$  keV around  
 807 11:17 UT as shown in panel (a) in Fig. 2.1. For directional information, panel (b)  
 808 in Fig. 2.1 shows flux as a function of local pitch angle ( $\alpha_L$ ) and time for 46-66 keV  
 809 electrons. Electrons that traveled towards the northern hemisphere had  $\alpha_L < 90^\circ$  and  
 810 southern hemisphere had  $\alpha_L > 90^\circ$ . The interval between the two vertical dashed  
 811 black lines contain the four microbursts examined in this study. We observed these  
 812 microbursts at  $\alpha_L < 50^\circ$ , but MagEIS-A did not sample into the  $0^\circ$  loss cone.

813 Figure 2.1 panel (c) shows the EMFISIS WFR data from RBSP-A. Between  
 814 11:17:05 and 11:17:10 UT, we observed an isolated burst of whistler mode wave power  
 815 in the frequency range  $0.1 < \omega < 0.3 \Omega_{ce0}$ , where  $\Omega_{ce0}$  is the equatorial electron  
 816 gyrofrequency. No individual rising or falling tone elements were observed during  
 817 this period, and the waves appeared more “hiss-like” (e.g. Li et al., 2012). This wave  
 818 was near-parallel propagating (evidence shown in Appendix A) and about 10 minutes  
 819 later, weak chorus rising tone elements were observed (not shown).

820 Panels (d)-(f) in Fig. 2.1 are in the same format as panels (a)-(c), but for RBSP-  
 821 B. An injection or boundary was observed with RBSP-B at 11:16:50 UT and RBSP-A  
 822 observed a similar feature soon after 11:18 UT (not shown).

823 A zoomed-in version of Fig. 2.1 panels (a) and (b) is shown in Fig. 2.2. Panel  
 824 (a) shows the four microburst-like signatures observed between 11:17:10 and 11:17:12  
 825 UT, at energies up to 92 keV. The observed duration of the microbursts was 150  
 826 - 500 ms, and they did not arrive dispersed in energy, which indicates that they  
 827 were recently scattered near the spacecraft location. We use IRBEM-Lib, a library  
 828 dedicated to radiation belt modeling (Boscher et al., 2012), to calculate the mirror  
 829 point altitudes, which were found to be above LEO. Panel (b) shows the RBSPICE-  
 830 A EBR time series with the group of microbursts observed at the same time as  
 831 in panel (a). To understand the timing relationship between the MagEIS-A and

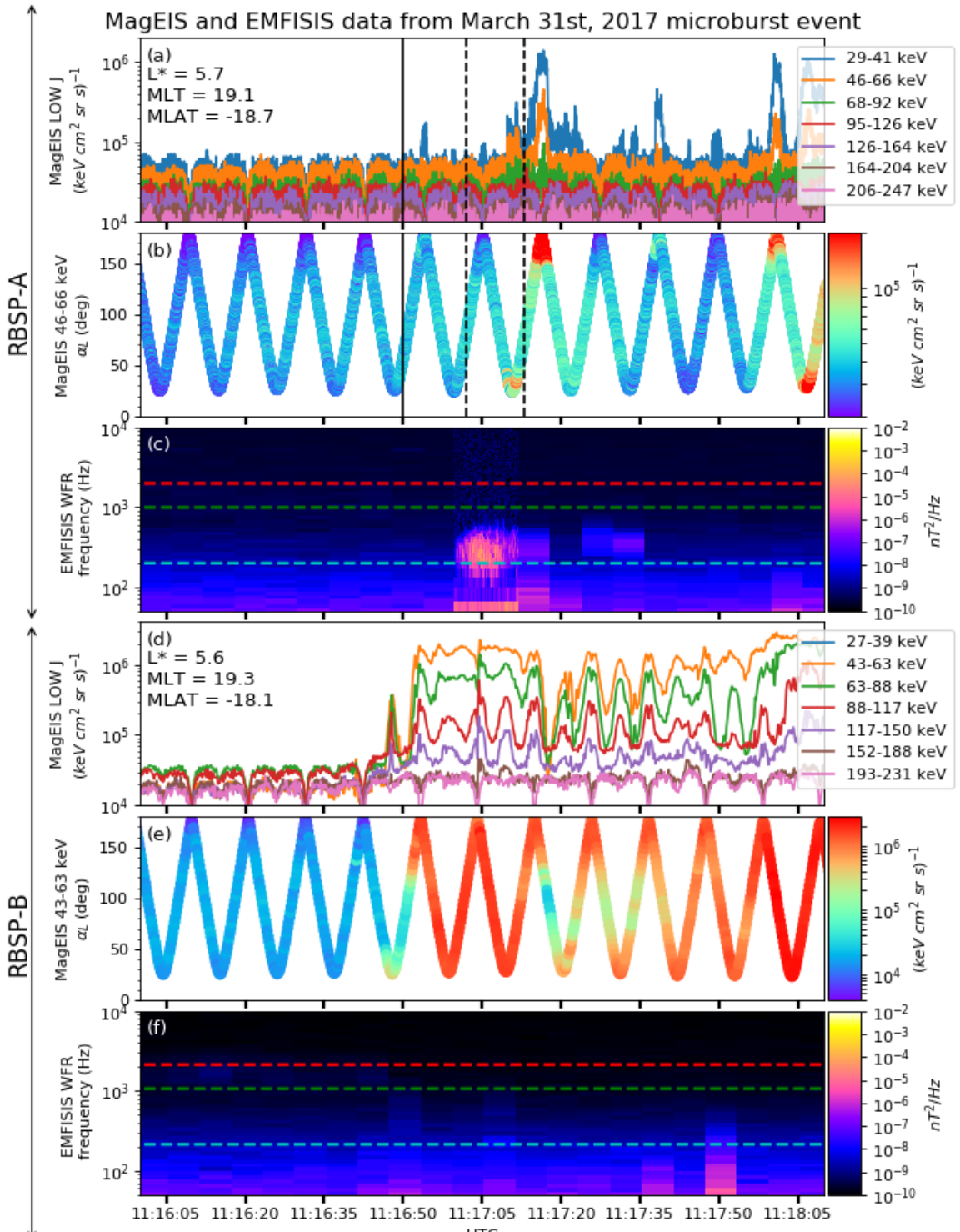


Figure 2.1: Electron and wave conditions from the MagEIS-A and EMFISIS WFR sensors for the microburst time interval. Panels (a), (b), and (c) are from RBSP-A with its position information annotated in panel (a). Panels (d), (e), and (f) are from RBSP-B with its position information annotated in panel (d). Panel (a) is the MagEIS-A high rate timeseries. Panels (b) and (e) show the evolution of the MagEIS-A  $J$  as a function of  $\alpha_L$  from the  $\sim 40$  to  $\sim 60$  keV channel. Every 10th point is shown in panel (b). The solid black line in panels (a) and (b) mark the end of the time period used for the PSD fit extrapolation analysis explained in section

832 RBSPICE-A observations, we marked the times when MagEIS-A observed the four  
 833 microbursts by vertical black arrows in panels (a) and (b). MagEIS-A observed the  
 834 first microburst  $\sim 0.5$  s before RBSPICE-A. The bounce period of locally mirroring,  
 835 100 keV electrons was  $\sim 0.8$  s, so this was unlikely to have been a returning bounce.  
 836 This evidence confirms that these microburst signatures are packets of electrons and  
 837 not a boundary moving back and forth at RBSP-A's location. To understand the  
 838 PA extent of these microbursts, panel (c) shows the 29-41 keV MagEIS-A  $J$  and  
 839 RBSPICE-A EBR as a function of  $\alpha_L$  and time. The microburst  $J$  was observed  
 840 by MagEIS-A between  $25^\circ < \alpha_L < 50^\circ$  and RBSPICE-A between  $100^\circ < \alpha_L < 160^\circ$ ,  
 841 with the highest intensities close to  $\alpha_L = 90^\circ$ . RBSPICE-A observed a 10-80%  
 842 enhancement in count rate over those PAs with the evidence presented in Appendix  
 843 A.

844 Analysis

845 First, we estimated the microburst energy spectra. For each microburst shown in  
 846 Fig. 2.2, its flux was averaged and baseline subtracted using the method from O'Brien  
 847 et al. (2004) and then fit with an exponential function. The calculated exponential  
 848 E-folding energy was found to vary between 25 and 35 keV, which is consistent with  
 849 spectra derived from prior measurements (Datta et al., 1997; Lee et al., 2012, 2005).

850 We then tested the hypothesis that the microburst electrons were transported  
 851 in energy and PA by a single chorus wave. We used a procedure similar to sections  
 852 3.1 and 4.5 in Meredith et al. (2002) which we describe below.

853 Microburst and Source PSD

854 We estimated the electron PSD,  $f(p_\perp, p_\parallel)$  where  $p_\perp$  and  $p_\parallel$  are the perpendicular  
 855 and parallel components of the electron momentum relative to the local magnetic field,

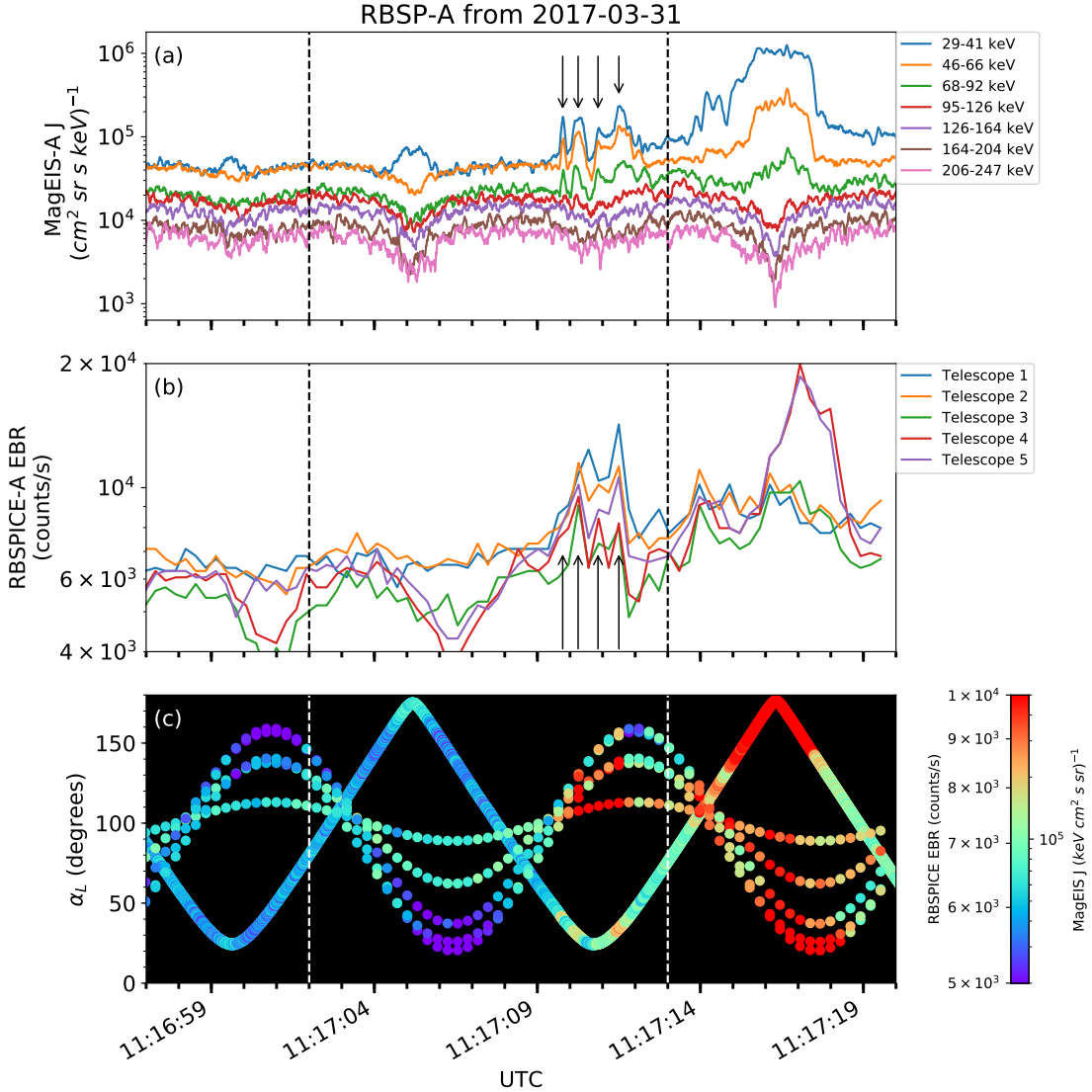


Figure 2.2: Panel (a) shows the MagEIS-A high rate timeseries. Panel (b) shows the RBSPIKE EBR count rate timeseries for  $\zeta = 19$  keV electrons. The microbursts were observed between 11:17:10 - 11:17:12 UT and are indicated with the vertical black arrows in panels (a) and (b) for MagEIS-A times. Panel (c) shows the RBSPIKE EBR (family of relatively sparse sampled curves) and MagEIS-A  $J$  from the 29-41 keV energy channel (single curve) as a function of  $\alpha_L$ . The vertical dashed lines show the time interval for the PSD analysis.

for the microburst time period. MagEIS-A  $J(E, \alpha_L)$  was averaged between 11:17:02 and 11:17:13 UT and binned by  $\alpha_L$  into  $5^\circ$  bins. Then, we assumed the conservation of the first adiabatic invariant and mapped  $\alpha_L$  to equatorial PA,  $\alpha_{eq}$ . The binned  $J(E, \alpha_{eq})$  was then converted to  $f(p_\perp, p_\parallel)$  via

$$f(p_\perp, p_\parallel) = \frac{J(E, \alpha_{eq})}{p^2}, \quad (2.1)$$

where  $p = \sqrt{p_\perp^2 + p_\parallel^2}$ . Lastly,  $\alpha_{eq}$  was used to separate  $p$  into  $p_\perp$  and  $p_\parallel$  via

$$\frac{p_\parallel}{m_e c} = \frac{\sqrt{E(E + 2E_0)} \cos(\alpha_{eq})}{E_0} \quad (2.2)$$

$$\frac{p_\perp}{m_e c} = \frac{\sqrt{E(E + 2E_0)} \sin(\alpha_{eq})}{E_0} \quad (2.3)$$

where  $c$  is the speed of light,  $E$  is the kinetic energy,  $m_e$  is the electron mass, and  $E_0$  is the electron rest energy. The observed  $f(p_\perp, p_\parallel)$  in dimensionless momentum space is shown in Fig. 2.3 in all panels between the  $p_\parallel$  axis and the white dotted lines. The bright spot in  $f(p_\perp, p_\parallel)$  in the upper  $p_\parallel$  plane represents the four microbursts. Along with the observed PSD, we use Fig. 2.3 to explore the various PSD extrapolation and diffusion model assumptions which are described below.

We proceed under the assumption that the source of the microburst electrons is not likely to be at the latitude of the observation, and is closer to the magnetic equator. To look for a source of microburst electrons, we extrapolate the unobserved  $f(p_\perp, p_\parallel)$  of electrons with  $|\lambda_m| < 19^\circ$  using two cases with a  $90^\circ$ -peaked PAD of the form

$$f(E, \alpha_{eq}) = f_0(E) \sin^n(\alpha_{eq}) \quad (2.4)$$

where  $f_0(E)$  is a scaling parameter and  $n$  is a power parameter. Similarly to the

868 in-situ  $f(p_{\perp}, p_{||})$ , the  $f(E, \alpha_{eq}) \mapsto f(p_{\perp}, p_{||})$  conversion was applied.

869 In the first case, we fitted Eq. 2.4 to the quiet time  $J(E, \alpha_{eq})$  from 11:15:00 to  
 870 11:16:50 UT (end time shown as the black vertical line in Fig. 2.1). The fitted  
 871 PAD was relatively flat with  $0.4 < n < 0.5$  and highest magnitude of  $f_0$  was  
 872  $0.05 \text{ cm}^3/(\text{MeV} \text{ s})^3$ . This extrapolated  $f(p_{\perp}, p_{||})$  is shown in Fig. 2.3 panels (A) and  
 873 (E), between the dotted white lines for scattering at  $\lambda = 0^\circ$  and  $20^\circ$ , respectively.  
 874 To confirm the relatively low  $n$  parameter, we found times where RBSP-A was in  
 875 a similar L-MLT location, but closer to the magnetic equator. At 2 and 19 UT on  
 876 the same day, we fit the  $J(E, \alpha_{eq})$ , and the fit parameters were very similar to the  
 877 pre-microburst  $f(p_{\perp}, p_{||})$  at 11 UT. Thus it is a reasonable assumption that  $f(p_{\perp}, p_{||})$   
 878 was relatively flat near the equator.

879 In the other case, we estimate how large  $n$  would have to be in order to find  
 880 sufficient PSD in MagEIS-A's energy range to be a source of the microburst electrons.  
 881 We used  $n \in \{1, 2, 4\}$  and we forced the  $f_0(E)$  parameter to match the observed  
 882  $f(p_{\perp}, p_{||})$  at the most equatorial PAs observed by MagEIS-A. These extrapolations  
 883 are shown in columns 2-4 in Fig. 2.3. There was enough source PSD anywhere in  
 884 MagEIS-A's energy range only if  $n \geq 2$ .

885 Motion of resonant electrons in phase space

To calculate the motion of resonant electrons in momentum space, we used the relativistic theory of wave-particle resonant diffusion developed by Walker (1993) and Summers et al. (1998) and applied in Meredith et al. (2002). The chorus wave can modify  $f(p_{\perp}, p_{||})$  when a resonance condition is satisfied. The cyclotron resonance condition between an electron with velocity  $v = \sqrt{v_{||}^2 + v_{\perp}^2}$  and a parallel propagating

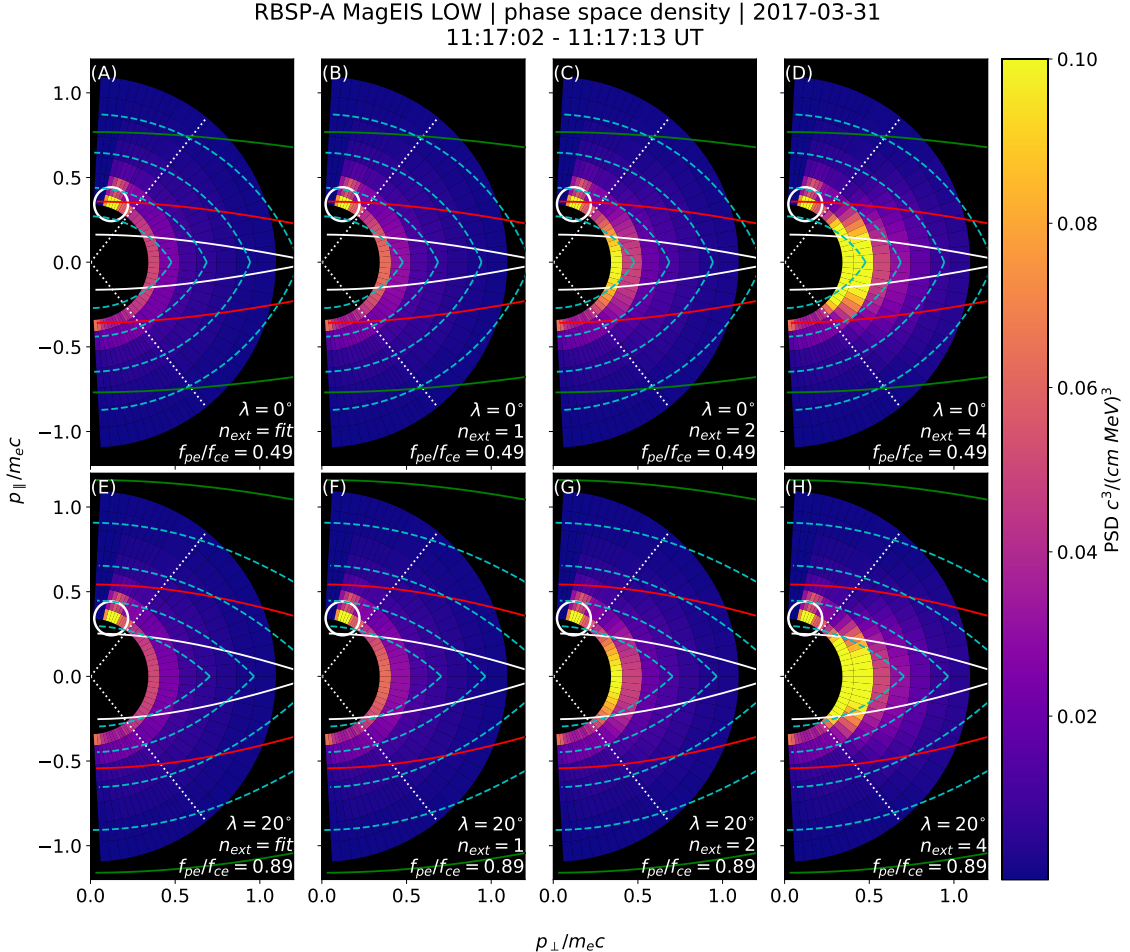


Figure 2.3: The colored annulus represents  $f(p_{\perp}, p_{\parallel})$  in normalized momentum space, parallel and perpendicular to the background magnetic field. The microburst  $f(p_{\perp}, p_{\parallel})$  is highlighted with the white circle. The columns show different powers of the sine extrapolation, and rows show the different magnetic latitudes of the scattering. The white dotted traces represent the boundary between the data and extrapolation. The green, red, and white solid traces are the resonance curves for  $\omega = 0.2\Omega_{ce}$ ,  $0.4\Omega_{ce}$ ,  $0.6\Omega_{ce}$ , respectively. The cyan dashed traces are the diffusion curves for a  $\omega = 0.4\Omega_{ce}$  wave (waves of other frequency have similar diffusion curves). The magnetic latitude of the scattering, the ratio of the plasma to the cyclotron frequency, and the power of the sine extrapolation is annotated in each panel. For the resonance and diffusion curves, the density model assumed a  $n_L = 1 e^-/cm^3$  and  $\psi = -1$ .

wave of frequency  $\omega$  and wave number  $k_{\parallel}$  is given by

$$\omega - v_{\parallel} k_{\parallel} = \frac{\Omega_{ce}}{\gamma}, \quad (2.5)$$

where  $\Omega_{ce}$  is the electron gyrofrequency at the scattering location, and  $\gamma$  is the relativistic correction. Assuming the cold plasma approximation,

$$k_{\parallel} = \frac{\omega}{c} \sqrt{1 - \frac{\omega_{pe}^2}{\omega(\omega - |\Omega_{ce}|)}}, \quad (2.6)$$

where  $\omega_{pe}$  is the plasma frequency. For a particular set of parameters, Eq. 2.5 defines a curve in momentum space that describes which electrons will resonate with a monochromatic wave.

To calculate  $k_{\parallel}$ , we approximated the electron number density,  $n_e(\lambda)$  locally and at the magnetic equator. Locally, the plasma density was approximately  $n_e(\lambda = -20^\circ) = n_L \approx 1 \text{ cm}^{-3}$ . We used magnetospheric seismology techniques (e.g. Takahashi and Denton, 2007) to parameterize  $n_e(\lambda)$  elsewhere along the field line with

$$n_e(\lambda) = n_e(0) \left( \frac{LR_e}{R(\lambda)} \right)^{\psi} \quad (2.7)$$

where  $R_e$  is the Earth's radius,  $R(\lambda)$  is the radial distance from the Earth to the spacecraft, and  $\psi$  is the exponent parameter. Assuming a dipole magnetic field for which  $R(\lambda) = LR_e \cos^2 \lambda$  (e.g. Schulz and Lanzerotti, 1974), we can express Eq. 2.7 in terms of  $n_L$  via

$$n_e(\lambda) = n_L \left( \frac{\cos \lambda_L}{\cos \lambda} \right)^{2\psi} \quad (2.8)$$

where we used  $\psi = -1$  (higher density at the magnetic equator) in this analysis. We chose this exponent parameter because it is a realistic best case scenario for the

896 electrons to be transported along the diffusion curves (described below).

Walker (1993) and Summers et al. (1998) argued that a resonant electron will move along diffusion curves in momentum space. A diffusion curve is derived as follows. In the reference frame moving with a monochromatic chorus wave's phase velocity (wave frame), the chorus wave is stationary and there is no electric field. Thus in the wave frame, the electron's kinetic energy is conserved, and the electron's velocity in the wave frame can be expressed in differential form as

$$v_{\parallel}dv_{\parallel} + v_{\perp}dv_{\perp} = 0. \quad (2.9)$$

After a Lorentz transformation of Eq. 2.9 into the magnetosospheric frame, kinetic energy will no longer be conserved. After integration and manipulation of Eq. 2.9, we obtain:

$$\left(1 - \frac{u_0^2 v_0^2}{c^4}\right)v_{\parallel}^2 - 2u_0\left(1 - \frac{v_0^2}{c^2}\right)v_{\parallel} + \left(1 - \frac{u_0^2}{c^2}\right)v_{\perp}^2 = v_0^2 - u_0^2 \quad (2.10)$$

897 where  $u_0 = \omega/k_{\parallel}$  is the phase velocity, and  $v_0$  is a constant of integration (Summers  
898 et al., 1998; Walker, 1993). Equation 2.10 defines a family of diffusion curves in  
899 momentum space on which resonant electrons will move. The distance that an  
900 electron moves along a diffusion curve is a function of wave and plasma parameters,  
901 and is estimated from the magnitude of the diffusion coefficients and the resonance  
902 time.

### 903 Comparing the microburst PSD to diffusion theory

904 Superposed on the PSD plots in Fig. 2.3 are resonance curves for chorus waves  
905 of  $\omega = 0.2\Omega_{ce}$ ,  $0.4\Omega_{ce}$ ,  $0.6\Omega_{ce}$  and a few diffusion curves for a  $\omega = 0.4\Omega_{ce}$  wave.  
906 These curves were parameterized by  $\lambda$  using a dipole magnetic field for  $\lambda = 0^\circ$

(Fig. 2.3, panels A-D) and  $\lambda = 20^\circ$  (Fig. 2.3, panels E-H). If the transport of microburst electrons is consistent with gyro-resonant diffusion, a diffusion curve that passes through the microburst  $f(p_\perp, p_\parallel)$  must also pass through another region with at least the same magnitude PSD ( $f(p_\perp, p_\parallel) \geq 0.1 \text{ c}^3/(\text{cm MeV})^3$ ) e.g. Fig. 2.3, panel (D). With this constraint, an artificially high extrapolated  $f(p_\perp, p_\parallel)$  with  $n > 2$  (5 times larger than calculated from the fits) must be assumed for there to have been a sufficient source of PSD anywhere in MagEIS-A's energy range.

We now show that by comparing MagEIS observations with theory, that the minimum wave amplitude necessary to scatter these electrons is much higher than was observed by EMFISIS-A. If we assume a unrealistic PAD with enough PSD just equatorward of RBSP-A, we can use MagEIS-A observations to calculate the minimum  $\Delta\alpha_{eq}$  that the electrons were transported. We then used diffusion theory to calculate the necessary wave amplitude. For microbursts with larger PAs, MagEIS-A observed a transport of  $\Delta\alpha_{eq} = 9^\circ$  and for microbursts with smaller PAs, the observed transport was  $\Delta\alpha_{eq} = 24^\circ$ . The required wave amplitude was calculated with Eq. 3 from Thorne and Andreoli (1981) assuming a maximum resonance period of a quarter bounce. The observed change in PA requires a wave amplitude  $0.2 < |B_w| < 0.5 \text{ nT}$ . For a few brief moments, the EMFISIS-A WFR waveform data showed  $0.1 < |B_w| < 0.15 \text{ nT}$ , so a transport of  $9^\circ$  is plausible, but not likely for  $24^\circ$ .

Another source of microburst electrons may be from energies below MagEIS-A's range. The Helium, Oxygen, Proton, and Electron mass spectrometer (Funsten et al., 2013) on RBSP-A observed  $f(p_\perp, p_\parallel) \geq 0.1 \text{ c}^3/(\text{cm MeV})^3$  for  $\pm 23 \text{ keV}$  electrons at this time. We then assumed the wave amplitude derived above to predict the transport in energy. We used the fact that the momentum and pitch angle diffusion coefficients,  $D_{pp}$  and  $D_{\alpha\alpha}$  are related via  $D_{pp}/p^2 \sim D_{\alpha\alpha}$  or equivalently,  $\Delta p/p \sim \Delta\alpha$ . The observed PA transport corresponds to an energy transport of  $6 < \Delta E < 16$

keV. Therefore, this wave can transport 23 keV electrons from smaller pitch angles to larger pitch angles and would be observed in the 29 – 41 keV MagEIS-A channel. However, this wave is insufficient to transport electrons to the 68 – 92 keV channel in one interaction. Therefore we conclude that quasi-linear diffusion cannot explain the observed microbursts.

938

### Discussion and Conclusions

These novel observations of impulsive electron signatures reported here fall well within the broad definition of a microburst as described in section 3. Their properties were similar to microbursts observed in LEO, with an E-folding energy of  $25 < E_0 < 35$  keV (Datta et al., 1997; Lee et al., 2012, 2005), duration of 150-500 ms (Lorentzen et al., 2001a), observed upper energy limit of 92 keV, and a lack of clear energy dispersion (Breneman et al., 2017). With MagEIS-A’s high time and energy resolution, we conclude that these dispersionless microbursts were recently scattered near the spacecraft. Furthermore, RBSPICE-A’s PA coverage suggests that these electrons were scattered over a substantial range of PAs, with the highest intensities near  $\alpha_L = 90^\circ$ . Overall, our observational evidence suggests that on time scales shorter than one bounce period, the chorus wave effectively accelerated trapped electrons over a broad PA range.

In the theoretical framework of wave-particle resonant diffusion applied to the observed PSD in section 3, we determine that the observed scattering is not consistent with the quasi-linear approximation. The nearest source of sufficient PSD is too far away in phase space to have been transported by the hypothesized quasi-linear process over a timescale shorter than one bounce period (one interaction). A similar conclusion was made by Mozer et al. (2018) who used quasi-linear theory constrained by RBSP wave measurements. They successfully modeled the one second average

958 precipitating flux observed with AeroCube-6 (AC-6) CubeSats during a conjunction,  
 959 but they were unable to model the AC-6 fluxes on smaller time scales.

960 To put these microburst observations into a wider magnetospheric perspective,  
 961 we observed them during the recovery phase of a minimum Dst of -75 nT storm, a  
 962 statistically favorable time period for microbursts (O'Brien et al., 2003). Furthermore,  
 963 during the same storm on March 27th, the Arase spacecraft observed highly correlated  
 964 lower band chorus with 10-50 keV electron precipitation inside the loss cone. At  
 965 that time, Arase's magnetic field footprint was near The Pas All-Sky Imager (part  
 966 of the THEMIS mission) which simultaneously observed pulsating auroral patches  
 967 (Kasahara et al., 2018). While microbursts and pulsating auroral patches have not  
 968 been clearly connected, they are both believed to be a product of electron scattering  
 969 by whistler mode waves (e.g. Lorentzen et al., 2001a; Nishimura et al., 2011; O'Brien  
 970 et al., 2003; Ozaki et al., 2012).

971 The combined capabilities of the various RBSP wave and particle instruments  
 972 enable comprehensive studies of wave-particle scattering and the resulting microburst  
 973 precipitation. From a preliminary search by the authors, other microburst-like  
 974 signatures have been found with RBSP. Similar to previous studies (e.g. Blum et al.,  
 975 2015; O'Brien et al., 2003), a statistical study of high-altitude microbursts in L-MLT  
 976 space needs to be conducted before we can verify that these microbursts are the  
 977 counterpart of the microbursts observed in LEO and the upper atmosphere.

978

### Acknowledgments

979 The authors acknowledge the technicians, engineers, and scientists who made the  
 980 RBSP and AC-6 missions possible. One author (Shumko) would like to acknowledge  
 981 Dana Longcope for his help in understanding the quasi-linear diffusion theory. Dr.  
 982 Gkioulidou was supported by JHU/APL subcontract 131803 to the NJIT under NASA

983 Prime contract NNN06AA01C. EMFISIS work was supported by JHU/APL contract  
984 no. 921647 under NASA Prime contract No. NAS5-01072. The MagEIS instrument  
985 was funded by NASA's Prime contract no. NAS5-01072. The level 3 MagEIS-A  
986 "high rate" data is available in the Supporting Information, level 1 RBSPICE EBR  
987 data is archived at <http://rbspicea.ftecs.com/>, and the EMFISIS level 2 spectral  
988 matrix and burst data as well as the level 3 magnetometer data is archived at  
989 <http://emfisis.physics.uiowa.edu/data/index>. The IRBEM Library can be obtained  
990 at [irbem.sf.net](http://irbem.sf.net).

## CHAPTER THREE

991  
992 MICROBURST SCALE SIZE DERIVED FROM MULTIPLE BOUNCES OF A  
993 MICROBURST SIMULTANEOUSLY OBSERVED WITH THE FIREBIRD-II  
994 CUBESATS

995 Contribution of Authors and Co-Authors

996 Manuscript(s) in Chapter(s) 1

997

998 Author: [type author name here]

999 Contributions: [list contributions here, single-spaced]

1000 Co-Author: [type co-author name here]

1001 Contributions: [list contributions here, single-spaced]

1002 Co-Author: [type co-author name here]

1003 Contributions: [list contributions here, single-spaced]

1004

1005

Manuscript Information

1006 [Type Author and Co-author(s) Names Here]

1007 Geophysical Research Letters

1008 Status of Manuscript: Published in a peer-reviewed journal

1009 Wiley

1010 Volume 45, Issue 17

1011

Key Points

1012

- Multiple bounces from a microburst were observed by the two FIREBIRD-II CubeSats at LEO.
- The lower bounds on the microburst scale size at LEO were  $29 \pm 1$  km (latitudinal) and  $51 \pm 11$  km (longitudinal).
- Deduced lower bound equatorial scale size was similar to the whistler-mode chorus source scale.

1018

Abstract

1019

We present the observation of a spatially large microburst with multiple bounces made simultaneously by the FIREBIRD-II CubeSats on February 2nd, 2015. This is the first observation of a microburst with a subsequent decay made by two co-orbiting but spatially separated spacecraft. From these unique measurements, we place estimates on the lower bounds of the spatial scales as well as quantify the electron bounce periods. The microburst's lower bound latitudinal scale size was  $29 \pm 1$  km and the longitudinal scale size was  $51 \pm 1$  km in low earth orbit. We mapped these scale sizes to the magnetic equator and found that the radial and azimuthal scale sizes were at least  $500 \pm 10$  km and  $530 \pm 10$  km, respectively. These lower bound equatorial scale sizes are similar to whistler-mode chorus wave source scale sizes, which supports the hypothesis that microbursts are a product of electron scattering by chorus waves. Lastly, we estimated the bounce periods for 200-800 keV electrons and found good agreement with four common magnetic field models.

1032

Introduction

1033       The dynamics of radiation belt electrons are complex, and are driven by  
 1034 competition between source and loss processes. A few possible loss processes are  
 1035 radial diffusion (Shprits and Thorne, 2004), magnetopause shadowing (Ukhorskiy  
 1036 et al., 2006), and pitch angle and energy diffusion due to scattering of electrons by  
 1037 plasma waves (e.g. Abel and Thorne, 1998; Horne and Thorne, 2003; Meredith et al.,  
 1038 2002; Mozer et al., 2018; Selesnick et al., 2003; Summers et al., 1998; Thorne et al.,  
 1039 2005). There are a variety of waves that cause pitch angle scattering, including  
 1040 electromagnetic ion cyclotron waves, plasmaspheric hiss, and chorus (Millan and  
 1041 Thorne, 2007; Thorne, 2010). Chorus predominantly occurs in the dawn sector (6-12  
 1042 magnetic local times (MLT)) (Li et al., 2009b) where it accelerates electrons with  
 1043 large equatorial pitch angles and scatters electrons with small equatorial pitch angles  
 1044 (Horne and Thorne, 2003). Some of these electrons may be impulsively scattered  
 1045 into the loss cone, where they result in short-duration ( $\sim 100$  ms) enhancements in  
 1046 precipitating flux called microbursts.

1047       Anderson and Milton (1964) coined the term microburst to describe high altitude  
 1048 balloon observations of  $\sim 100$  ms duration enhancements of bremsstrahlung X-  
 1049 rays emitted from scattered microburst electrons impacting the atmosphere. Since  
 1050 then, non-relativistic (less than a few hundred keV) microbursts have been routinely  
 1051 observed with other balloon missions (e.g. Anderson et al., 2017; Parks, 1967; Woodger  
 1052 et al., 2015). A review of the literature shows no reports of microbursts above a few  
 1053 hundred keV observed by balloons (Millan et al., 2002; Woodger et al., 2015). This  
 1054 lack of observation may be explained by relatively weaker pitch angle scattering of  
 1055 relativistic electrons by chorus (Lee et al., 2012).

1056       In addition to the X-ray signature for bursts of electron precipitation, the

1057 precipitating relativistic and non-relativistic electrons have been measured in situ by  
 1058 spacecraft orbiting in low earth orbit (LEO). Hereinafter, we refer to these electron  
 1059 signatures observed by LEO spacecraft also as microbursts. Microbursts have been  
 1060 observed with, e.g. the Solar Anomalous and Magnetospheric Particle Explorer's  
 1061 (SAMPEX)  $\gtrsim$  150 keV and  $\gtrsim$  1 MeV channels (Blake et al., 1996; Blum et al., 2015;  
 1062 Lorentzen et al., 2001a,b; Nakamura et al., 1995, 2000; O'Brien et al., 2004, 2003) and  
 1063 Focused Investigation of Relativistic Electron Bursts: Intensity, Range, and Dynamics  
 1064 (FIREBIRD-II) with its  $\gtrsim$  200 keV energy channels (Anderson et al., 2017; Breneman  
 1065 et al., 2017; Crew et al., 2016).

1066 Understanding microburst precipitation and its scattering mechanism is impor-  
 1067 tant to radiation belt dynamics. The scattering mechanism has been observationally  
 1068 studied by e.g. Lorentzen et al. (2001b) who found that microbursts and chorus  
 1069 waves predominantly occur in the dawn sector and Breneman et al. (2017) made  
 1070 a direct observational link between individual microbursts and chorus elements.  
 1071 Microbursts have been modeled and empirically estimated to be capable of depleting  
 1072 the relativistic electron population in the outer radiation belt on the order of a day  
 1073 (Breneman et al., 2017; O'Brien et al., 2004; Shprits et al., 2007; Thorne et al., 2005).  
 1074 An important parameter in this estimation of instantaneous radiation belt electron  
 1075 losses due to microbursts is their scale size. Parks (1967) used balloon measurements  
 1076 of bremsstrahlung X-rays to estimate the high altitude scale size of predominantly low  
 1077 energy microbursts to be  $40 \pm 14$  km. In Blake et al. (1996) a microburst with multiple  
 1078 bounces was observed by SAMPEX, and the microburst's latitudinal scale size in LEO  
 1079 was estimated to have been "at least a few tens of kilometers". Blake et al. (1996)  
 1080 concluded that typically microbursts are less than a few tens of electron gyroradii in  
 1081 size (at  $L = 5$  at LEO, the gyroradii of 1 MeV electrons is on the order of 100 m).  
 1082 Dietrich et al. (2010) used SAMPEX along with ground-based very low frequency

1083 stations to conclude that during one SAMPEX pass, the observed microbursts had  
1084 scale sizes less than 4 km.

1085 Since February 1st, 2015, microbursts have been observed by FIREBIRD-II, a  
1086 pair of CubeSats in LEO. Soon after launch, when the two FIREBIRD-II spacecraft  
1087 were at close range, a microburst with a scale size greater than 11 km was observed  
1088 (Crew et al., 2016). On the same day, FIREBIRD-II simultaneously observed a  
1089 microburst with multiple bounces. The microburst decay was observed over a period  
1090 of a few seconds, while the spacecraft were traveling predominantly in latitude. Here  
1091 we present the analysis and results of the latitude and longitude scale sizes and  
1092 bounce periods of the first microburst with multiple bounces observed with the two  
1093 FIREBIRD-II spacecraft.

1094 Spacecraft and Observation

1095 The FIREBIRD missions are comprised of a pair of identically-instrumented  
1096 1.5U CubeSats (15 x 10 x 10 cm) that are designed to measure electron precipitation  
1097 in LEO (Klumpar et al., 2015; Spence et al., 2012). The second mission, termed  
1098 FIREBIRD-II, was launched on January 31st 2015. The two FIREBIRD-II CubeSats,  
1099 identified as Flight Unit 3 (FU3) and Flight Unit 4 (FU4), were placed in a 632 km  
1100 apogee, 433 km perigee, and 99° inclination orbit (Crew et al., 2016). FU3 and FU4  
1101 are orbiting in a string of pearls configuration with FU4 ahead, to resolve the space-  
1102 time ambiguity of microbursts. Each FIREBIRD-II unit has two solid state detectors:  
1103 one is mounted essentially at the spacecraft surface, covered only by a thin foil acting  
1104 as a sun shade, with a field of view of 90° (surface detector), and the other is beneath  
1105 a collimator which restricts the field of view to 54° (collimated detector). Only FU3  
1106 has a functioning surface detector, so this analysis utilizes the collimated detectors.  
1107 FU3's surface and collimated detectors, as well as FU4's collimated detector observe

1108 electron fluxes in six energy channels from  $\sim 230$  keV to  $> 1$  MeV. FIREBIRD-II's  
 1109 High Resolution (HiRes) electron flux data is gathered with an adjustable sampling  
 1110 period of 18.75 ms by default and can be as fast as 12.5 ms.

1111 On February 2nd, 2015 at 06:12 UT, both FIREBIRD-II spacecraft simulta-  
 1112 neously observed an initial microburst, followed by subsequent periodic electron  
 1113 enhancements of diminishing amplitude shown in Fig. 3.1. This is thought to be  
 1114 the signature of a single burst of electrons, some of which precipitate, but the rest  
 1115 mirror near the spacecraft then bounce to the conjugate hemisphere where they mirror  
 1116 again and the subsequent bounces produce a train of decaying peaks (Blake et al.,  
 1117 1996; Thorne et al., 2005). This bounce signature occurred during the transition  
 1118 between the main and recovery phases of a storm with a minimum Dst of -44 nT  
 1119 ( $K_p = 4$ , and  $AE \approx 400$  nT). At this time, the HiRes data was sampled at 18.75 ms.  
 1120 Five peaks were observed by both spacecraft. The fifth peak observed by FU4 was  
 1121 comparable to the Poisson noise and was not used in this analysis. This microburst  
 1122 was observed from the first energy channel ( $\approx 200 - 300$  keV), to the fourth energy  
 1123 channel ( $\approx 500 - 700$  keV), and FU3's surface detector observed the microburst up  
 1124 to the fifth energy channel (683 - 950 keV).

1125 The HiRes data in Fig. 3.1 shows signs of energy dispersion, characterized by  
 1126 higher energy electrons arriving earlier than the lower energies. This time of flight  
 1127 energy dispersion tends to smear out the initial sharp burst upon each subsequent  
 1128 bounce. The first peak does not appear to be dispersed, and subsequent peaks show  
 1129 a dispersion trend consistent across energy channels. The black vertical bars have  
 1130 been added to Fig. 3.1 to highlight this energy dispersion. This dispersion signature  
 1131 and amplitude decay implies that the first peak was observed soon after the electrons  
 1132 were scattered, followed by decaying bounces.

1133 At this time, in magnetic coordinates, FIREBIRD-II was at McIlwain  $L = 4.7$

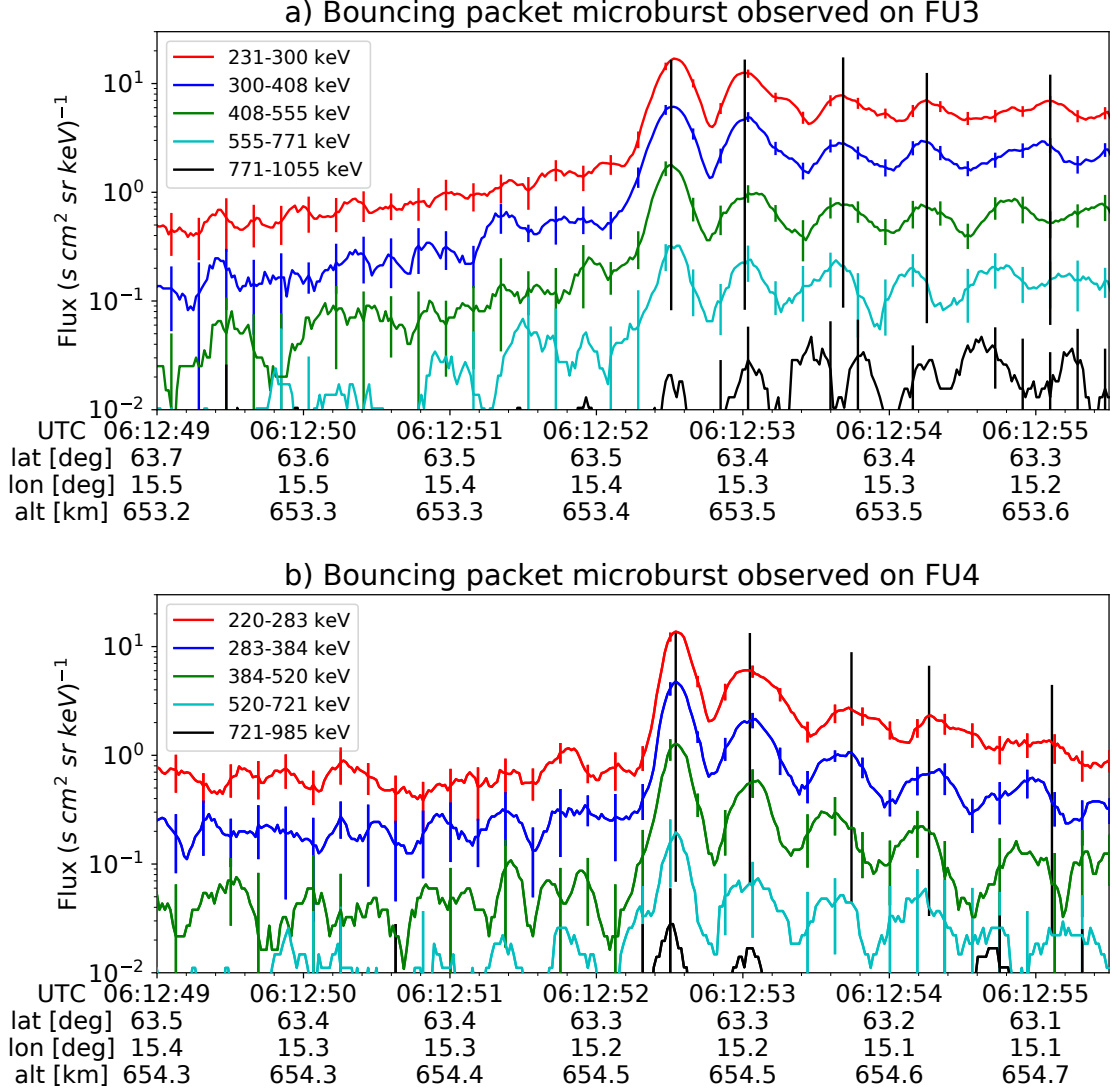


Figure 3.1: HiRes data of the microburst observed at February 2nd, 2015 at 06:12:53 UT, smoothed with a 150 ms rolling average. The subsequent bounces showed some energy dispersion. As discussed in Appendix B, a time correction of -2.28 s was applied to FU3. While the flux from five energy channels is shown, only channels with reasonable counting statistics were used for the spatial scale analysis. Vertical colored bars show the  $\sqrt{N}$  error every 10th data point and vertical black bars are lined up with the peaks in the 220-283 keV energy channel to help identify dispersion.

and MLT = 8.3, calculated with the Tsyganenko 1989 (T89) magnetic field model (Tsyganenko, 1989) using IRBEM-Lib (Boscher et al., 2012). Geographically, they were above Sweden, latitude = 63°N, longitude = 15°E, altitude = 650 km. This geographic location is magnetically conjugate to the east of the so-called South Atlantic Anomaly (SAA). The SAA is the location where the mirror points of electrons tend to occur at locations deeper in the atmosphere owing to the offset of the dipole magnetic field from the Earth's center. Electrons with pitch angles within the drift loss cone (DLC) will encounter the SAA and be removed from their eastward longitudinal drift paths (Comess et al., 2013; Dietrich et al., 2010). FU3 and FU4 are therefore both in regions where the particles in the DLC have recently precipitated, leaving only particles that were recently scattered. At the spacecraft location, locally mirroring electrons would have mirrored at 95 km in the opposite hemisphere, with more field aligned electrons mirroring at even lower altitudes. From the analysis done by Fang et al. (2010), the peak in the total ionization rate in the atmosphere for 100 keV electrons is around 80 km altitude, while the total ionization rate from 1 MeV electrons peaks around 60 km altitude. It is, therefore, expected that a fraction of the microburst electrons will survive each encounter with the atmosphere. By plotting the peak flux as a function of bounce (not shown), it was found that 40 - 60 % of the microburst electrons were lost on the first bounce, similar to the 33% loss per bounce observed for a bouncing microburst observed by SAMPEX (Thorne et al., 2005).

1154

### Analysis

At the beginning of the FIREBIRD-II mission, two issues prevented the proper analysis of the microburst's spatial scale size: the spacecraft clocks were not synchronized, and their relative positions were not accurately known. We addressed these issues with a cross-correlation time lag analysis described in detail in Appendix

1159 B. From this analysis, the time correction was  $2.28 \pm 0.12$  s (applied to Fig. 3.1) and  
 1160 the separation was  $19.9 \pm 0.9$  km at the time of the microburst observation.

1161 Electron Bounce Period

1162 We used this unique observation of bouncing electrons to calculate the bounce  
 1163 period,  $t_b$  as a function of energy and compare it to the energy-dependent  $t_b$  curves  
 1164 derived from four magnetic field models, the results of which are shown in Fig. 3.2.  
 1165 The observed  $t_b$  and uncertainties were calculated by fitting the baseline-subtracted  
 1166 HiRes flux. The baseline flux used in this analysis is given in O'Brien et al. (2004)  
 1167 as the flux at the 10th percentile over a specified time interval, which in this analysis  
 1168 was taken to be 0.5 seconds. The flux was fitted with a superposition of Gaussians  
 1169 for each energy channel, and the uncertainty in flux was calculated using the Poisson  
 1170 error from the microburst and baseline fluxes summed in quadrature. Using the fit  
 1171 parameters, the mean  $t_b$  for the lowest four energy channels is shown in Fig. 3.2. The  
 1172 trend of decreasing  $t_b$  as a function of energy is evident in Fig. 3.2, which further  
 1173 supports the assumption that the subsequent peaks are bounces, and not a train of  
 1174 microbursts scattered by bouncing chorus.

1175 The decaying peaks in the 231-408 keV electron flux observed by FU3's lowest  
 1176 two energy channels (see Fig. 3.1) were right-skewed. One explanation is that there  
 1177 was in-channel energy dispersion within those channels. Since  $t_b$  of higher energy  
 1178 electrons is shorter, a right-skewed peak implies that higher energy electrons were  
 1179 more abundant within that channel e.g. in FU3's 231-300 keV channel, the 300 keV  
 1180 electrons will arrive sooner than the 231 keV electrons, but will they will be binned  
 1181 in the same channel. A Gaussian fit cannot account for this in-channel dispersion,  
 1182 and as a first order correction, minima between peaks was used to calculate  $t_b$ , and  
 1183 is shown in Fig. 3.2. The observed energy-dependent dispersion shown in Fig. 3.2

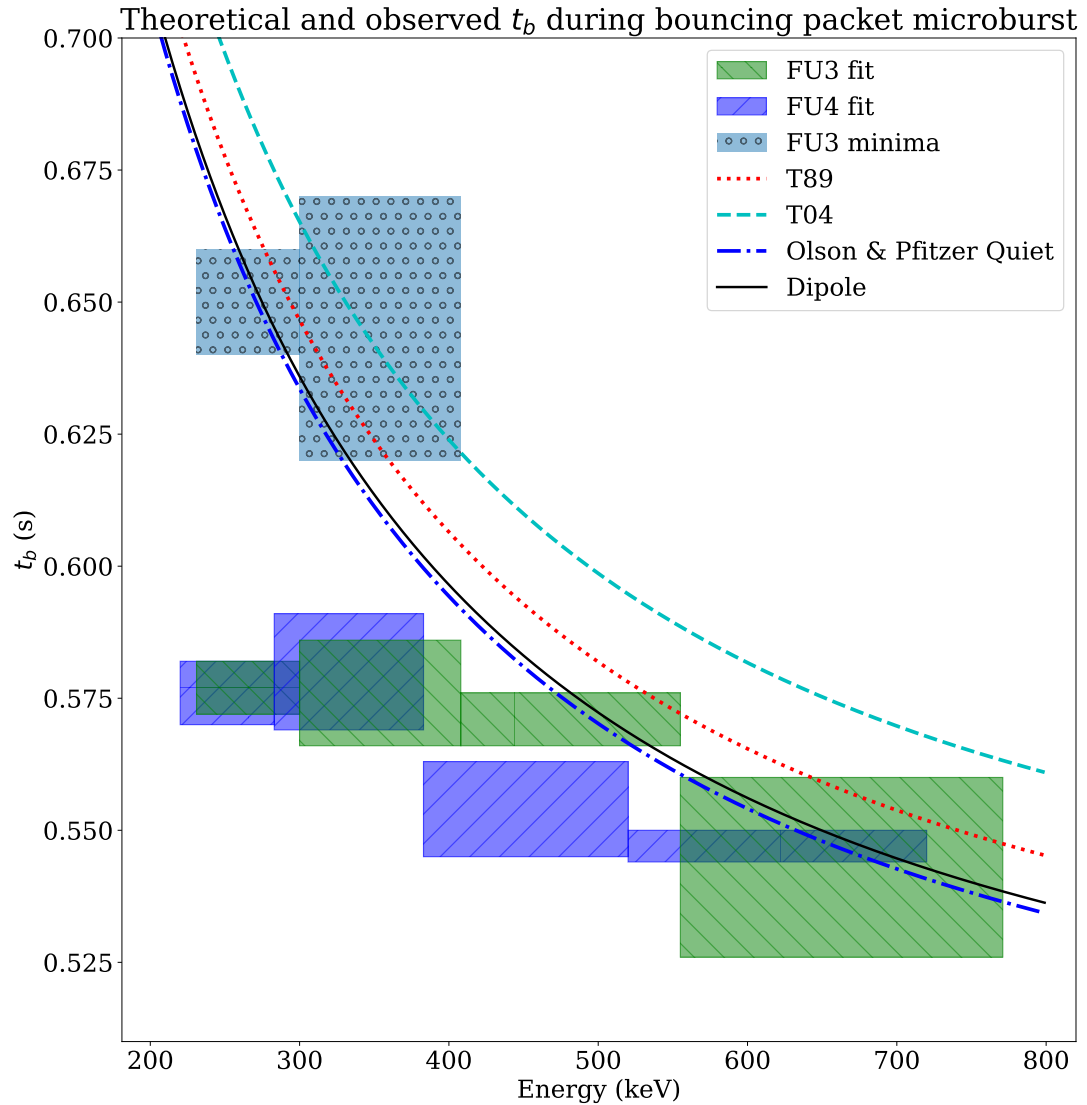


Figure 3.2: Observed and theoretical  $t_b$  for electrons of energies from 200 to 770 keV. The solid black line is  $t_b$  in a dipole magnetic field, derived in Schulz and Lanzerotti (1974). The red dotted and cyan dashed lines are the  $t_b$  derived using the T89, and T04 magnetic field models with IRBEM-Lib. Lastly, the blue dot-dash curve is the  $t_b$  derived using the Olson & Pfitzer Quiet model. The green and purple rectangles represent the observed  $t_b$  for FU3 and FU4 using a Gaussian fit, respectively. The blue rectangles represent the observed  $t_b$  calculated with the minima between the bounces. The width of the boxes represent the width of those energy channels, and the height represents the uncertainty from the fit.

1184 is consistent with higher energy peaks returning sooner. This dispersion consistency  
 1185 further supports the assumption that the subsequent peaks are bounces, and not a  
 1186 train of microbursts scattered by bouncing chorus.

1187 To compare the observed and modeled  $t_b$ , we superposed  $t_b$  curves for various  
 1188 models including an analytical solution in a dipole (Schulz and Lanzerotti, 1974), and  
 1189 numerical models: T89, Tsyganenko 2004 (T04) (Tsyganenko and Sitnov, 2005), and  
 1190 Olson & Pfitzer Quiet (Olson and Pfitzer, 1982) in Fig. 3.2. The numerical  $t_b$  curves  
 1191 were calculated using a wrapper for IRBEM-Lib. This code traces the magnetic field  
 1192 line between mirror points, and calculates  $t_b$  assuming conservation of energy and the  
 1193 first adiabatic invariant for electrons mirroring at FIREBIRD-II. With the empirical  
 1194  $t_b$ , the models agree within FIREBIRD-II's uncertainties, but the T04 model has the  
 1195 largest discrepancy compared to the other models.

1196 Microburst Energy Spectra

1197 Next, we investigated the energy spectra of this microburst. The energy spectra  
 1198 was modeled with an exponential that was fit to the peak flux derived from the  
 1199 Gaussian fit parameters in section 3 to all but the highest energy channel. We found  
 1200 that the E-folding energy,  $E_0 \sim 100$  keV. This spectra is similar to spectra show  
 1201 by Lee et al. (2005) from STSAT-1 and Datta et al. (1997) from sounding rocket  
 1202 measurements. The energy spectra is soft for a typical microburst observed with  
 1203 FIREBIRD-II and there was no statistically significant change in  $E_0$  for subsequent  
 1204 bounces.

1205 Microburst Scale Sizes

1206 Lastly, after we applied the time and separation corrections detailed in Appendix  
 1207 B, we mapped the locations of FU3 and FU4 in Fig. 3.3. The locations where FU3 saw  
 1208 peaks 1-5 and where FU4 saw peaks 1-4 are shown as P1-5 and P1-4, respectively.

1209 The lower bound on the latitudinal extent of the microburst was the difference in  
 1210 latitude between P1 on FU3 and P4 on FU4 and was found to be  $29 \pm 1$  km. The  
 1211 uncertainty was estimated from the spacecraft separation uncertainty described in  
 1212 Appendix B. This scale size is the largest reported by FIREBIRD-II.

1213 In section 3, we showed that the observed decaying peaks were likely due to  
 1214 bouncing, so we assume that the observed electrons in subsequent bounces were the  
 1215 drifted electrons from the initial microburst. Under this assumption, the scattered  
 1216 electrons observed in the last bounce by FIREBIRD-II, must have drifted east from  
 1217 their initial scattering longitude, allowing us to calculate the minimum longitudinal  
 1218 scale size. Following geometrical arguments, the distance that electrons drift east in  
 1219 a single bounce is a product of the circumference of the drift shell foot print, and the  
 1220 fraction of the total drift orbit traversed in a single bounce and is given by,

$$d_{az} = 2\pi(R_E + A) \cos(\lambda) \frac{t_b}{\langle T_d \rangle} \quad (3.1)$$

where  $R_E$  is the Earth's radius,  $A$  is the spacecraft altitude,  $\lambda$  is the magnetic latitude,  
 $t_b$  is the electron bounce period, and  $\langle T_d \rangle$  is the electron drift period. Parks (2003)  
derived  $\langle T_d \rangle$  to be,

$$\langle T_d \rangle \approx \begin{cases} 43.8/(L \cdot E) & \text{if } \alpha_0 = 90^\circ \\ 62.7/(L \cdot E) & \text{if } \alpha_0 = 0^\circ \end{cases} \quad (3.2)$$

1221 where  $E$  is the electron energy in MeV,  $L$  is the L shell, and  $\alpha_0$  is the equatorial pitch  
 1222 angle. Electrons mirroring at FIREBIRD-II have  $\alpha_0 \approx 3.7^\circ$  and so the  $\alpha_0 = 0^\circ$  limit  
 1223 was used.

1224 The microburst's longitudinal scale size is defined as the distance the highest  
 1225 energy electrons drifted in the time between the observations of the first and last  
 1226 peaks. This scale size is given by  $D_{az} = n d_{az}$  where  $n$  is the number of bounces

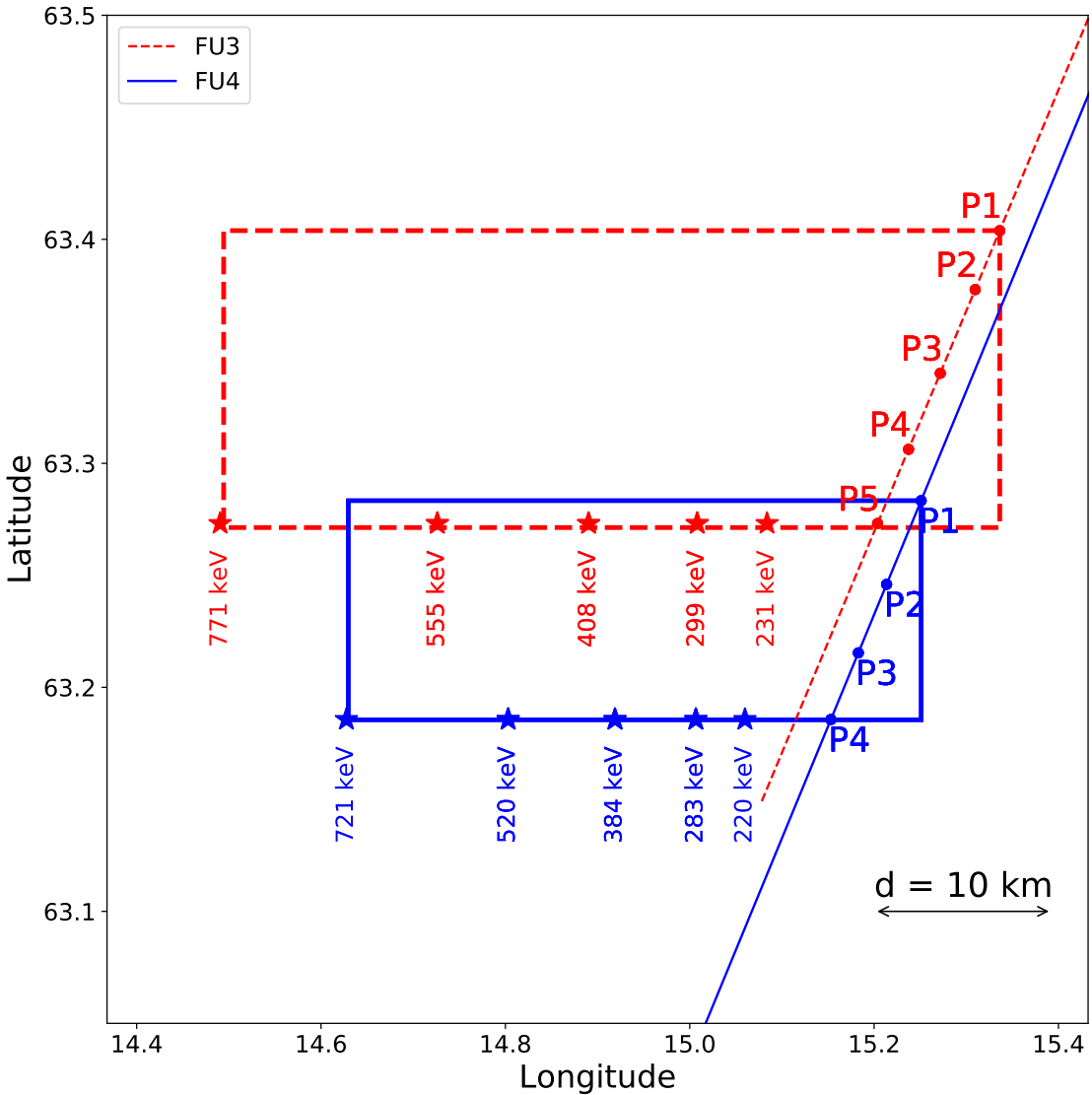


Figure 3.3: The topology of the FIREBIRD-II orbit and the multiple bounces of the microburst projected onto latitude and longitude with axis scaled to equal distance. Attributes relating to FU3 shown in red dashed lines, and FU4 with blue solid lines. The spacecraft path is shown with the diagonal lines, starting at the upper right corner. The labels P1-4 for FU4 and P1-5 for FU3 indicate where the spacecraft were when the  $N^{\text{th}}$  peak was seen in the lowest energy channel in the HiRes data. The stars with the accompanying energy labels represent the locations of the electrons with that energy that started at time of P1, and were seen at the last peak on each spacecraft. The rectangles represent the lower bound of the microburst scale size, assuming that the majority of the electrons were in the upper boundary of energy channel 4.

1227 observed. The stars in Fig. 3.3 (with labels corresponding to energy channel  
 1228 boundaries) represent the locations when the microburst was observed at P1, such  
 1229 that an electron of that energy would drift eastward to be seen at P5 for FU3 and P4  
 1230 for FU4. Since FU3 observed more peaks it observed the larger longitudinal scale size  
 1231 which is shown with the red dashed box in Fig. 3.3. FU3's fourth energy channel's  
 1232 bounds are 555 keV and 771 keV, which correspond to longitudinal distances of  $39 \pm 1$   
 1233 km and  $51 \pm 1$ , respectively. The uncertainty was estimated by propagating the  
 1234 uncertainty in the bounce time Eq. 3.1. While the observed minimum longitudinal  
 1235 scale size is dependent on FIREBIRD-II's energy channels, the true scale size may  
 1236 not be.

1237 To investigate how the microburst scale size compares to the scale sizes of chorus  
 1238 waves near the magnetic equator, the microburst's longitudinal and latitudinal scale  
 1239 sizes and their uncertainties in LEO were mapped to the magnetic equator with T89.  
 1240 The radial scale size (latitudinal scale mapped from LEO) was greater than  $500 \pm 10$   
 1241 km. The azimuthal scale size (longitudinal scale mapped from LEO) of 555 keV  
 1242 electrons was greater than  $450 \pm 10$  km and for the 771 keV electrons it was greater  
 1243 than  $530 \pm 10$  km. The lower bound microburst scale size is similar to the chorus  
 1244 scale sizes derived by Agapitov et al. (2017, 2011), and is discussed below.

1245

### Discussion and Conclusions

1246 We presented the first observation of a large microburst with multiple bounces  
 1247 made possible by the twin FIREBIRD-II CubeSats. The microburst's lower bound  
 1248 LEO latitudinal and longitudinal scale sizes of  $29 \pm 1$  km and  $51 \pm 1$  km make  
 1249 it one of the largest observed. The microburst's LEO scale size was larger than  
 1250 the latitudinal scale sizes of typical  $\gtrsim 1$  MeV microbursts reported in Blake et al.  
 1251 (1996), approximately 10 times larger than reported in Dietrich et al. (2010), and

1252 approximately 2.6 times larger than other simultaneous microbursts observed by  
 1253 FIREBIRD-II (Crew et al., 2016). Lastly, the scale sizes derived here were similar to  
 1254 the scale sizes of  $\sim$  15 keV microbursts observed with a high altitude balloon (Parks,  
 1255 1967). No energy dependence on the minimum latitudinal scale size was observed,  
 1256 while the observed energy dependence of the minimum longitudinal scale size is an  
 1257 artifact of the technique we used to estimate their drift motion.

1258 The microburst scale size obtained in Section 3 and scaled to the geomagnetic  
 1259 equator can be compared with the scales of chorus waves presumably responsible for  
 1260 the rapid burst electron precipitation. Early direct estimates of the chorus source  
 1261 scales were made by the coordinated measurement by ISEE-1, 2. The wave power  
 1262 correlation scale was estimated to be about several hundred kilometers across the  
 1263 background magnetic field (Gurnett et al., 1979). Furthermore, Santolik et al. (2003)  
 1264 determined the correlation lengths of chorus-type whistler waves to be around 100  
 1265 km based on multipoint CLUSTER Wide Band Data measurements near the chorus  
 1266 source region at  $L \approx 4$ , during the magnetic storm of 18 April 2002. Agapitov et al.  
 1267 (2017, 2011, 2010) recently showed that the spatial extent of chorus source region can  
 1268 be larger, ranging from 600 km in the outer radiation belt to more than 1000 km in  
 1269 the outer magnetosphere. The lower bound azimuthal and latitudinal scales obtained  
 1270 in Section 3 and scaled to the magnetic equator, are similar to the whistler-mode  
 1271 chorus source scale sizes reported in Agapitov et al. (2017, 2011).

1272 No wave measurements from nearby spacecraft were available at this time.  
 1273 Nevertheless, during the hours before and after this observation, the Van Allen Probes'  
 1274 (Mauk et al., 2013) Electric and Magnetic Field Instrument and Integrated Science  
 1275 (Kletzing et al., 2013) observed strong wave power in the lower band chorus frequency  
 1276 range, inside the outer radiation belt between 22 and 2 MLT. Furthermore, AE  $\sim 400$   
 1277 nT at this time, and relatively strong chorus waves were statistically more likely to

1278 be present at FIREBIRD-II's MLT (Li et al., 2009b).

1279 The empirically estimated and modeled  $t_b$  in this study agree within FIREBIRD-  
 1280 II's uncertainties, confirming that the energy-dependent dispersion was due to  
 1281 bouncing. The  $t_b$  curves are a proxy for field line length, and this agreement implies  
 1282 that they are comparable. This is expected since the magnetosphere is not drastically  
 1283 compressed at 8 MLT, but we expect a larger discrepancy near midnight, where the  
 1284 magnetosphere is more stretched and difficult to accurately model. In future studies,  
 1285 this analysis can be used as a diagnostic tool to validate field line lengths, and improve  
 1286 magnetic field models.

1287 The similarity of the microburst and chorus source region scale sizes, as well  
 1288 as magnetospheric location and conditions, further support the causal relationship  
 1289 between microbursts and chorus.

1290

### Acknowledgments

1291 This work was made possible with help from the FIREBIRD team, and the  
 1292 members of the Space Sciences and Engineering Laboratory at Montana State  
 1293 University for their hard work to make this mission a success. In addition, M.  
 1294 Shumko acknowledges Drew Turner for his suggestions regarding the bounce period  
 1295 calculations, and Dana Longcope for his proofreading feedback. The FIREBIRD-II  
 1296 data are available at [http://solar.physics.montana.edu/FIREBIRD\\_II/](http://solar.physics.montana.edu/FIREBIRD_II/). This analysis  
 1297 is supported by the National Science Foundation under Grant Numbers 0838034 and  
 1298 1339414. Furthermore, the work of O. Agapitov was supported by the NASA grant  
 1299 NNX16AF85G.

1300

## CONCLUSION

1301        L<sup>A</sup>T<sub>E</sub>X produces documents that look great, automatically handles references and  
1302        citations, and easily incorporates figures and tables. This is not a guide to L<sup>A</sup>T<sub>E</sub>X but  
1303        rather an introduction to the MSU style. If you want more information about L<sup>A</sup>T<sub>E</sub>X  
1304        many introductory guides can be found online.

- 1306 Abel, B. and Thorne, R. M. (1998). Electron scattering loss in earth's inner  
1307 magnetosphere: 1. dominant physical processes. *Journal of Geophysical Research: Space Physics*, 103(A2):2385–2396.
- 1309 Agapitov, O., Blum, L. W., Mozer, F. S., Bonnell, J. W., and Wygant, J. (2017).  
1310 Chorus whistler wave source scales as determined from multipoint van allen probe  
1311 measurements. *Geophysical Research Letters*, pages n/a–n/a. 2017GL072701.
- 1312 Agapitov, O., Krasnoselskikh, V., Dudok de Wit, T., Khotyaintsev, Y., Pickett,  
1313 J. S., Santolik, O., and Rolland, G. (2011). Multispacecraft observations of chorus  
1314 emissions as a tool for the plasma density fluctuations' remote sensing. *Journal of Geophysical Research: Space Physics*, 116(A9):n/a–n/a. A09222.
- 1316 Agapitov, O., Krasnoselskikh, V., Zaliznyak, Y., Angelopoulos, V., Le Contel, O.,  
1317 and Rolland, G. (2010). Chorus source region localization in the earth's outer  
1318 magnetosphere using themis measurements. *Annales Geophysicae*, 28(6):1377–  
1319 1386.
- 1320 Anderson, B., Shekhar, S., Millan, R., Crew, A., Spence, H., Klumpar, D., Blake, J.,  
1321 O'Brien, T., and Turner, D. (2017). Spatial scale and duration of one microburst  
1322 region on 13 August 2015. *Journal of Geophysical Research: Space Physics*.
- 1323 Anderson, K. A. and Milton, D. W. (1964). Balloon observations of X rays in the  
1324 auroral zone: 3. High time resolution studies. *Journal of Geophysical Research*,  
1325 69(21):4457–4479.
- 1326 Barcus, J., Brown, R., and Rosenberg, T. (1966). Spatial and temporal character of  
1327 fast variations in auroral-zone x rays. *Journal of Geophysical Research*, 71(1):125–  
1328 141.
- 1329 Baumjohann, W. and Treumann, R. A. (1997). *Basic space plasma physics*. World  
1330 Scientific.
- 1331 Blake, J., Carranza, P., Claudepierre, S., Clemons, J., Crain, W., Dotan, Y.,  
1332 Fennell, J., Fuentes, F., Galvan, R., George, J., et al. (2013). The magnetic electron  
1333 ion spectrometer (MagEIS) instruments aboard the radiation belt storm probes  
1334 (RBSP) spacecraft. *Space Science Reviews*, 179(1-4):383–421.
- 1335 Blake, J.,Looper, M., Baker, D., Nakamura, R., Klecker, B., and Hovestadt, D.  
1336 (1996). New high temporal and spatial resolution measurements by sampex of the  
1337 precipitation of relativistic electrons. *Advances in Space Research*, 18(8):171 – 186.
- 1338 Blake, J. B. and O'Brien, T. P. (2016). Observations of small-scale latitudinal  
1339 structure in energetic electron precipitation. *Journal of Geophysical Research: Space Physics*, 121(4):3031–3035. 2015JA021815.

- 1341 Blum, L., Li, X., and Denton, M. (2015). Rapid MeV electron precipitation as  
 1342 observed by SAMPEX/HILT during high-speed stream-driven storms. *Journal of*  
 1343 *Geophysical Research: Space Physics*, 120(5):3783–3794. 2014JA020633.
- 1344 Bortnik, J., Thorne, R., and Inan, U. S. (2008). Nonlinear interaction of energetic  
 1345 electrons with large amplitude chorus. *Geophysical Research Letters*, 35(21).
- 1346 Boscher, D., Bourdarie, S., O'Brien, P., Guild, T., and Shumko, M. (2012). Irbem-lib  
 1347 library.
- 1348 Breneman, A., Crew, A., Sample, J., Klumpar, D., Johnson, A., Agapitov, O.,  
 1349 Shumko, M., Turner, D., Santolik, O., Wygant, J., et al. (2017). Observations  
 1350 directly linking relativistic electron microbursts to whistler mode chorus: Van allen  
 1351 probes and FIREBIRD II. *Geophysical Research Letters*.
- 1352 Breneman, A. W., Halford, A., Millan, R., McCarthy, M., Fennell, J., Sample, J.,  
 1353 Woodger, L., Hospodarsky, G., Wygant, J. R., Cattell, C. A., et al. (2015). Global-  
 1354 scale coherence modulation of radiation-belt electron loss from plasmaspheric hiss.  
 1355 *Nature*, 523(7559):193.
- 1356 Brown, R., Barcus, J., and Parsons, N. (1965). Balloon observations of auroral zone  
 1357 x rays in conjugate regions. 2. microbursts and pulsations. *Journal of Geophysical*  
 1358 *Research (U.S.)*.
- 1359 Capannolo, L., Li, W., Ma, Q., Shen, X.-C., Zhang, X.-J., Redmon, R., Rodriguez,  
 1360 J., Engebretson, M., Kletzing, C., Kurth, W., et al. (2019). Energetic electron  
 1361 precipitation: multi-event analysis of its spatial extent during emic wave activity.  
 1362 *Journal of Geophysical Research: Space Physics*.
- 1363 Claudepierre, S., O'Brien, T.,Looper, M., Blake, J., Fennell, J., Roeder, J.,  
 1364 Clemons, J., Mazur, J., Turner, D., Reeves, G., et al. (2019). A revised look  
 1365 at relativistic electrons in the earth's inner radiation zone and slot region. *Journal*  
 1366 *of Geophysical Research: Space Physics*, 124(2):934–951.
- 1367 Comess, M., Smith, D., Selesnick, R., Millan, R., and Sample, J. (2013). Duskside  
 1368 relativistic electron precipitation as measured by sampex: A statistical survey.  
 1369 *Journal of Geophysical Research: Space Physics*, 118(8):5050–5058.
- 1370 Crew, A. B., Spence, H. E., Blake, J. B., Klumpar, D. M., Larsen, B. A., O'Brien,  
 1371 T. P., Driscoll, S., Handley, M., Legere, J., Longworth, S., Mashburn, K.,  
 1372 Mosleh, E., Ryhajlo, N., Smith, S., Springer, L., and Widholm, M. (2016). First  
 1373 multipoint in situ observations of electron microbursts: Initial results from the  
 1374 NSF FIREBIRD II mission. *Journal of Geophysical Research: Space Physics*,  
 1375 121(6):5272–5283. 2016JA022485.

- 1376 Datta, S., Skoug, R., McCarthy, M., and Parks, G. (1997). Modeling of microburst  
 1377 electron precipitation using pitch angle diffusion theory. *Journal of Geophysical*  
 1378 *Research: Space Physics*, 102(A8):17325–17333.
- 1379 Dietrich, S., Rodger, C. J., Clilverd, M. A., Bortnik, J., and Raita, T. (2010).  
 1380 Relativistic microburst storm characteristics: Combined satellite and ground-based  
 1381 observations. *Journal of Geophysical Research: Space Physics*, 115(A12).
- 1382 Douma, E., Rodger, C. J., Blum, L. W., and Clilverd, M. A. (2017). Occurrence  
 1383 characteristics of relativistic electron microbursts from SAMPEX observations.  
 1384 *Journal of Geophysical Research: Space Physics*, 122(8):8096–8107. 2017JA024067.
- 1385 Dungey, J. W. (1961). Interplanetary magnetic field and the auroral zones. *Phys.*  
 1386 *Rev. Lett.*, 6:47–48.
- 1387 Fang, X., Randall, C. E., Lummerzheim, D., Wang, W., Lu, G., Solomon, S. C., and  
 1388 Frahm, R. A. (2010). Parameterization of monoenergetic electron impact ionization.  
 1389 *Geophysical Research Letters*, 37(22).
- 1390 Funsten, H., Skoug, R., Guthrie, A., MacDonald, E., Baldonado, J., Harper, R.,  
 1391 Henderson, K., Kihara, K., Lake, J., Larsen, B., et al. (2013). Helium, Oxygen,  
 1392 Proton, and Electron (HOPE) mass spectrometer for the radiation belt storm  
 1393 probes mission. *Space Science Reviews*, 179(1-4):423–484.
- 1394 Greeley, A., Kanekal, S., Baker, D., Klecker, B., and Schiller, Q. (2019). Quantifying  
 1395 the contribution of microbursts to global electron loss in the radiation belts. *Journal*  
 1396 *of Geophysical Research: Space Physics*.
- 1397 Gurnett, D., Anderson, R., Scarf, F., Fredricks, R., and Smith, E. (1979). Initial  
 1398 results from the isee-1 and-2 plasma wave investigation. *Space Science Reviews*,  
 1399 23(1):103–122.
- 1400 Hendry, A. T., Rodger, C. J., and Clilverd, M. A. (2017). Evidence of sub-mev  
 1401 emic-driven electron precipitation. *Geophysical Research Letters*, 44(3):1210–1218.
- 1402 Hoots, F. R. and Roehrich, R. L. (1980). Models for propagation of norad element  
 1403 sets. Technical Report 3, Spacetrack.
- 1404 Horne, R., Glauert, S., Meredith, N., Boscher, D., Maget, V., Heynderickx, D., and  
 1405 Pitchford, D. (2013). Space weather impacts on satellites and forecasting the earth's  
 1406 electron radiation belts with spacecast. *Space Weather*, 11(4):169–186.
- 1407 Horne, R., Thorne, R., Meredith, N., and Anderson, R. (2003). Diffuse auroral  
 1408 electron scattering by electron cyclotron harmonic and whistler mode waves during  
 1409 an isolated substorm. *Journal of Geophysical Research: Space Physics*, 108(A7).

- 1410 Horne, R. B. and Thorne, R. M. (2003). Relativistic electron acceleration and  
 1411 precipitation during resonant interactions with whistler-mode chorus. *Geophysical*  
 1412 *Research Letters*, 30(10). 1527.
- 1413 Horne, R. B., Thorne, R. M., Shprits, Y. Y., Meredith, N. P., Glauert, S. A., Smith,  
 1414 A. J., Kanekal, S. G., Baker, D. N., Engebretson, M. J., Posch, J. L., et al.  
 1415 (2005). Wave acceleration of electrons in the van allen radiation belts. *Nature*,  
 1416 437(7056):227.
- 1417 Kasahara, S., Miyoshi, Y., Yokota, S., Mitani, T., Kasahara, Y., Matsuda, S.,  
 1418 Kumamoto, A., Matsuoka, A., Kazama, Y., Frey, H., et al. (2018). Pulsating  
 1419 aurora from electron scattering by chorus waves. *Nature*, 554(7692):337.
- 1420 Kletzing, C., Kurth, W., Acuna, M., MacDowall, R., Torbert, R., Averkamp, T.,  
 1421 Bodet, D., Bounds, S., Chutter, M., Connerney, J., et al. (2013). The electric and  
 1422 magnetic field instrument suite and integrated science (EMFISIS) on RBSP. *Space*  
 1423 *Science Reviews*, 179(1-4):127–181.
- 1424 Klumpar, D., Springer, L., Mosleh, E., Mashburn, K., Berardinelli, S., Gunderson,  
 1425 A., Handly, M., Ryhajlo, N., Spence, H., Smith, S., Legere, J., Widholm, M.,  
 1426 Longworth, S., Crew, A., Larsen, B., Blake, J., and Walmsley, N. (2015). Flight  
 1427 system technologies enabling the twin-cubesat firebird-ii scientific mission.
- 1428 Lee, J. J., Parks, G. K., Lee, E., Tsurutani, B. T., Hwang, J., Cho, K. S., Kim, K.-H.,  
 1429 Park, Y. D., Min, K. W., and McCarthy, M. P. (2012). Anisotropic pitch angle  
 1430 distribution of 100 keV microburst electrons in the loss cone: measurements from  
 1431 STSAT-1. *Annales Geophysicae*, 30(11):1567–1573.
- 1432 Lee, J.-J., Parks, G. K., Min, K. W., Kim, H. J., Park, J., Hwang, J., McCarthy,  
 1433 M. P., Lee, E., Ryu, K. S., Lim, J. T., Sim, E. S., Lee, H. W., Kang, K. I., and  
 1434 Park, H. Y. (2005). Energy spectra of 170–360 keV electron microbursts measured  
 1435 by the korean STSAT-1. *Geophysical Research Letters*, 32(13). L13106.
- 1436 Li, W., Thorne, R., Angelopoulos, V., Bonnell, J., McFadden, J., Carlson, C.,  
 1437 LeContel, O., Roux, A., Glassmeier, K., and Auster, H. (2009a). Evaluation of  
 1438 whistler-mode chorus intensification on the nightside during an injection event  
 1439 observed on the THEMIS spacecraft. *Journal of Geophysical Research: Space*  
 1440 *Physics*, 114(A1).
- 1441 Li, W., Thorne, R., Bortnik, J., Tao, X., and Angelopoulos, V. (2012). Characteristics  
 1442 of hiss-like and discrete whistler-mode emissions. *Geophysical Research Letters*,  
 1443 39(18).
- 1444 Li, W., Thorne, R. M., Angelopoulos, V., Bortnik, J., Cully, C. M., Ni, B., LeContel,  
 1445 O., Roux, A., Auster, U., and Magnes, W. (2009b). Global distribution of whistler-  
 1446 mode chorus waves observed on the THEMIS spacecraft. *Geophysical Research*  
 1447 *Letters*, 36(9). L09104.

- 1448 Li, X., Selesnick, R., Schiller, Q., Zhang, K., Zhao, H., Baker, D. N., and Temerin,  
 1449 M. A. (2017). Measurement of electrons from albedo neutron decay and neutron  
 1450 density in near-earth space. *Nature*, 552(7685):382.
- 1451 Lorentzen, K. R., Blake, J. B., Inan, U. S., and Bortnik, J. (2001a). Observations  
 1452 of relativistic electron microbursts in association with VLF chorus. *Journal of*  
 1453 *Geophysical Research: Space Physics*, 106(A4):6017–6027.
- 1454 Lorentzen, K. R.,Looper, M. D., and Blake, J. B. (2001b). Relativistic electron  
 1455 microbursts during the GEM storms. *Geophysical Research Letters*, 28(13):2573–  
 1456 2576.
- 1457 Lyons, L. R. and Thorne, R. M. (1973). Equilibrium structure of radiation belt  
 1458 electrons. *Journal of Geophysical Research*, 78(13):2142–2149.
- 1459 Manweiler, J. W. and Zwiener, H. M. (2018). Science Operations Center (SOC)  
 1460 RBSPICE Science Data Handbook Revision: e. Technical report, Fundamental  
 1461 Technologies, LLC.
- 1462 Mauk, B., Fox, N. J., Kanekal, S., Kessel, R., Sibeck, D., and Ukhorskiy, A. (2013).  
 1463 Science objectives and rationale for the radiation belt storm probes mission. *Space*  
 1464 *Science Reviews*, 179(1-4):3–27.
- 1465 Meredith, N., Horne, R., Summers, D., Thorne, R., Iles, R., Heynderickx, D., and  
 1466 Anderson, R. (2002). Evidence for acceleration of outer zone electrons to relativistic  
 1467 energies by whistler mode chorus. In *Annales Geophysicae*, volume 20, pages 967–  
 1468 979.
- 1469 Millan, R. and Thorne, R. (2007). Review of radiation belt relativistic electron losses.  
 1470 *Journal of Atmospheric and Solar-Terrestrial Physics*, 69(3):362 – 377.
- 1471 Millan, R. M., Lin, R., Smith, D., Lorentzen, K., and McCarthy, M. (2002). X-  
 1472 ray observations of mev electron precipitation with a balloon-borne germanium  
 1473 spectrometer. *Geophysical research letters*, 29(24).
- 1474 Mitchell, D., Lanzerotti, L., Kim, C., Stokes, M., Ho, G., Cooper, S., Ukhorskiy, A.,  
 1475 Manweiler, J., Jaskulek, S., Haggerty, D., et al. (2013). Radiation belt storm probes  
 1476 ion composition experiment (RBSPICE). *Space Science Reviews*, 179(1-4):263–308.
- 1477 Mozer, F. S., Agapitov, O. V., Blake, J. B., and Vasko, I. Y. (2018). Simultaneous  
 1478 observations of lower band chorus emissions at the equator and microburst  
 1479 precipitating electrons in the ionosphere. *Geophysical Research Letters*.
- 1480 Nakamura, R., Baker, D. N., Blake, J. B., Kanekal, S., Klecker, B., and Hovestadt,  
 1481 D. (1995). Relativistic electron precipitation enhancements near the outer edge of  
 1482 the radiation belt. *Geophysical Research Letters*, 22(9):1129–1132.

- 1483 Nakamura, R., Isowa, M., Kamide, Y., Baker, D., Blake, J., and Looper, M. (2000).  
 1484 Observations of relativistic electron microbursts in association with VLF chorus.  
 1485 *J. Geophys. Res.*, 105:15875–15885.
- 1486 Nishimura, Y., Bortnik, J., Li, W., Thorne, R., Chen, L., Lyons, L., Angelopoulos,  
 1487 V., Mende, S., Bonnell, J., Le Contel, O., et al. (2011). Multievent study of the  
 1488 correlation between pulsating aurora and whistler mode chorus emissions. *Journal*  
 1489 *of Geophysical Research: Space Physics*, 116(A11).
- 1490 O'Brien, T., Claudepierre, S., Blake, J., Fennell, J. F., Clemons, J., Roeder, J.,  
 1491 Spence, H. E., Reeves, G., and Baker, D. (2014). An empirically observed pitch-  
 1492 angle diffusion eigenmode in the earth's electron belt near  $l^*= 5.0$ . *Geophysical*  
 1493 *Research Letters*, 41(2):251–258.
- 1494 O'Brien, T., Claudepierre, S., Guild, T., Fennell, J., Turner, D., Blake, J., Clemons,  
 1495 J., and Roeder, J. (2016). Inner zone and slot electron radial diffusion revisited.  
 1496 *Geophysical Research Letters*, 43(14):7301–7310.
- 1497 O'Brien, T. and Moldwin, M. (2003). Empirical plasmapause models from magnetic  
 1498 indices. *Geophysical Research Letters*, 30(4).
- 1499 O'Brien, T. P., Looper, M. D., and Blake, J. B. (2004). Quantification of relativistic  
 1500 electron microburst losses during the GEM storms. *Geophysical Research Letters*,  
 1501 31(4). L04802.
- 1502 O'Brien, T. P., Lorentzen, K. R., Mann, I. R., Meredith, N. P., Blake, J. B., Fennell,  
 1503 J. F., Looper, M. D., Milling, D. K., and Anderson, R. R. (2003). Energization of  
 1504 relativistic electrons in the presence of ULF power and MeV microbursts: Evidence  
 1505 for dual ULF and VLF acceleration. *Journal of Geophysical Research: Space*  
 1506 *Physics*, 108(A8).
- 1507 Olson, W. P. and Pfitzer, K. A. (1982). A dynamic model of the magnetospheric  
 1508 magnetic and electric fields for july 29, 1977. *Journal of Geophysical Research:*  
 1509 *Space Physics*, 87(A8):5943–5948.
- 1510 Ozaki, M., Miyoshi, Y., Shiokawa, K., Hosokawa, K., Oyama, S.-i., Kataoka, R.,  
 1511 Ebihara, Y., Ogawa, Y., Kasahara, Y., Yagitani, S., et al. (2019). Visualization of  
 1512 rapid electron precipitation via chorus element wave-particle interactions. *Nature*  
 1513 *communications*, 10(1):257.
- 1514 Ozaki, M., Yagitani, S., Ishizaka, K., Shiokawa, K., Miyoshi, Y., Kadokura, A.,  
 1515 Yamagishi, H., Kataoka, R., Ieda, A., Ebihara, Y., Sato, N., and Nagano, I. (2012).  
 1516 Observed correlation between pulsating aurora and chorus waves at Syowa Station  
 1517 in Antarctica: A case study. *Journal of Geophysical Research: Space Physics*,  
 1518 117(A8).

- 1519 Parks, G. (2003). *Physics Of Space Plasmas: An Introduction, Second Edition.*  
 1520 Westview Press.
- 1521 Parks, G. K. (1967). Spatial characteristics of auroral-zone X-ray microbursts. *Journal  
 1522 of Geophysical Research*, 72(1):215–226.
- 1523 Reeves, G., Spence, H. E., Henderson, M., Morley, S., Friedel, R., Funsten, H., Baker,  
 1524 D., Kanekal, S., Blake, J., Fennell, J., et al. (2013). Electron acceleration in the  
 1525 heart of the van allen radiation belts. *Science*, 341(6149):991–994.
- 1526 Reeves, G. D., McAdams, K. L., Friedel, R. H. W., and O'Brien, T. P. (2003). Ac-  
 1527 celeration and loss of relativistic electrons during geomagnetic storms. *Geophysical  
 1528 Research Letters*, 30(10):n/a–n/a. 1529.
- 1529 Santolik, O., Gurnett, D., Pickett, J., Parrot, M., and Cornilleau-Wehrlin, N. (2003).  
 1530 Spatio-temporal structure of storm-time chorus. *Journal of Geophysical Research:  
 1531 Space Physics*, 108(A7).
- 1532 Santolk, O., Parrot, M., and Lefevre, F. (2003). Singular value decomposition  
 1533 methods for wave propagation analysis. *Radio Science*, 38(1):n/a–n/a. 1010.
- 1534 Schulz, M. and Lanzerotti, L. J. (1974). *Particle Diffusion in the Radiation Belts.*  
 1535 Springer.
- 1536 Selesnick, R. S., Blake, J. B., and Mewaldt, R. A. (2003). Atmospheric losses of  
 1537 radiation belt electrons. *Journal of Geophysical Research: Space Physics*, 108(A12).  
 1538 1468.
- 1539 Shprits, Y. Y., Meredith, N. P., and Thorne, R. M. (2007). Parameterization  
 1540 of radiation belt electron loss timescales due to interactions with chorus waves.  
 1541 *Geophysical Research Letters*, 34(11):n/a–n/a. L11110.
- 1542 Shprits, Y. Y. and Thorne, R. M. (2004). Time dependent radial diffusion modeling  
 1543 of relativistic electrons with realistic loss rates. *Geophysical Research Letters*,  
 1544 31(8):n/a–n/a. L08805.
- 1545 Spence, H. E., Blake, J. B., Crew, A. B., Driscoll, S., Klumpar, D. M., Larsen,  
 1546 B. A., Legere, J., Longworth, S., Mosleh, E., O'Brien, T. P., Smith, S., Springer,  
 1547 L., and Widholm, M. (2012). Focusing on size and energy dependence of electron  
 1548 microbursts from the van allen radiation belts. *Space Weather*, 10(11).
- 1549 Summers, D., Thorne, R. M., and Xiao, F. (1998). Relativistic theory of wave-particle  
 1550 resonant diffusion with application to electron acceleration in the magnetosphere.  
 1551 *Journal of Geophysical Research: Space Physics*, 103(A9):20487–20500.

- 1552 Takahashi, K. and Denton, R. E. (2007). Magnetospheric seismology using multi-  
 1553 harmonic toroidal waves observed at geosynchronous orbit. *Journal of Geophysical*  
 1554 *Research: Space Physics*, 112(A5).
- 1555 Thorne, R. M. (2010). Radiation belt dynamics: The importance of wave-particle  
 1556 interactions. *Geophysical Research Letters*, 37(22). L22107.
- 1557 Thorne, R. M. and Andreoli, L. J. (1981). *Mechanisms for Intense Relativistic*  
 1558 *Electron Precipitation*, pages 381–394. Springer Netherlands, Dordrecht.
- 1559 Thorne, R. M., O'Brien, T. P., Shprits, Y. Y., Summers, D., and Horne, R. B. (2005).  
 1560 Timescale for MeV electron microburst loss during geomagnetic storms. *Journal*  
 1561 *of Geophysical Research: Space Physics*, 110(A9). A09202.
- 1562 Trefall, H., Bjordal, J., Ullaland, S., and Stadsnes, J. (1966). On the extension of  
 1563 auroral-zone x-ray microbursts. *Journal of Atmospheric and Terrestrial Physics*,  
 1564 28(2):225–233.
- 1565 Tsurutani, B. T. and Lakhina, G. S. (1997). Some basic concepts of wave-particle  
 1566 interactions in collisionless plasmas. *Reviews of Geophysics*, 35(4):491–501.
- 1567 Tsyganenko, N. (1989). A solution of the chapman-ferraro problem for an ellipsoidal  
 1568 magnetopause. *Planetary and Space Science*, 37(9):1037 – 1046.
- 1569 Tsyganenko, N. A. and Sitnov, M. I. (2005). Modeling the dynamics of the inner  
 1570 magnetosphere during strong geomagnetic storms. *Journal of Geophysical Research:*  
 1571 *Space Physics*, 110(A3).
- 1572 Turner, D., Claudepierre, S., Fennell, J., O'Brien, T., Blake, J., Lemon, C.,  
 1573 Gkioulidou, M., Takahashi, K., Reeves, G., Thaller, S., et al. (2015). Energetic  
 1574 electron injections deep into the inner magnetosphere associated with substorm  
 1575 activity. *Geophysical Research Letters*, 42(7):2079–2087.
- 1576 Ukhorskiy, A. Y., Anderson, B. J., Brandt, P. C., and Tsyganenko, N. A. (2006).  
 1577 Storm time evolution of the outer radiation belt: Transport and losses. *Journal of*  
 1578 *Geophysical Research: Space Physics*, 111(A11):n/a–n/a. A11S03.
- 1579 Van Allen, J. A. (1959). The geomagnetically trapped corpuscular radiation. *Journal*  
 1580 *of Geophysical Research*, 64(11):1683–1689.
- 1581 Vernov, S. and Chudakov, A. (1960). Investigation of radiation in outer space. In  
 1582 *International Cosmic Ray Conference*, volume 3, page 19.
- 1583 Walker, A. D. M. (1993). *Plasma waves in the magnetosphere*, volume 24. Springer  
 1584 Science & Business Media.

- 1585 Woodger, L., Halford, A., Millan, R., McCarthy, M., Smith, D., Bowers, G., Sample,  
1586 J., Anderson, B., and Liang, X. (2015). A summary of the BARREL campaigns:  
1587 Technique for studying electron precipitation. *Journal of Geophysical Research: Space Physics*, 120(6):4922–4935.  
1588

## APPENDIX: APPENDIX A

1590 This appendix contains Figs. A.1 and A.2. Figure A.1 shows evidence that  
1591 supports our claim that the “hiss-like” chorus wave observed at 11:17:03 UT with  
1592 EMFISIS WFR instrument on RBSP-A was parallel propagating. The polar angle  
1593 of the wave vector and the supporting planarity of the magnetic field polarization  
1594 shown in Fig. A.1 was calculated using the singular value decomposition (SVD)  
1595 method (Santolk et al., 2003).

1596 Figure A.2 supports the claim that RBSPICE-A observed a 10-80% increase in  
1597 the count rates at the microburst times and pitch angles. Figure A.2 shows the ratio  
1598 of the RBSPICE-A’s EBR count rates during the four microbursts to the quiet time  
1599 one spin before, at the same pitch angles.

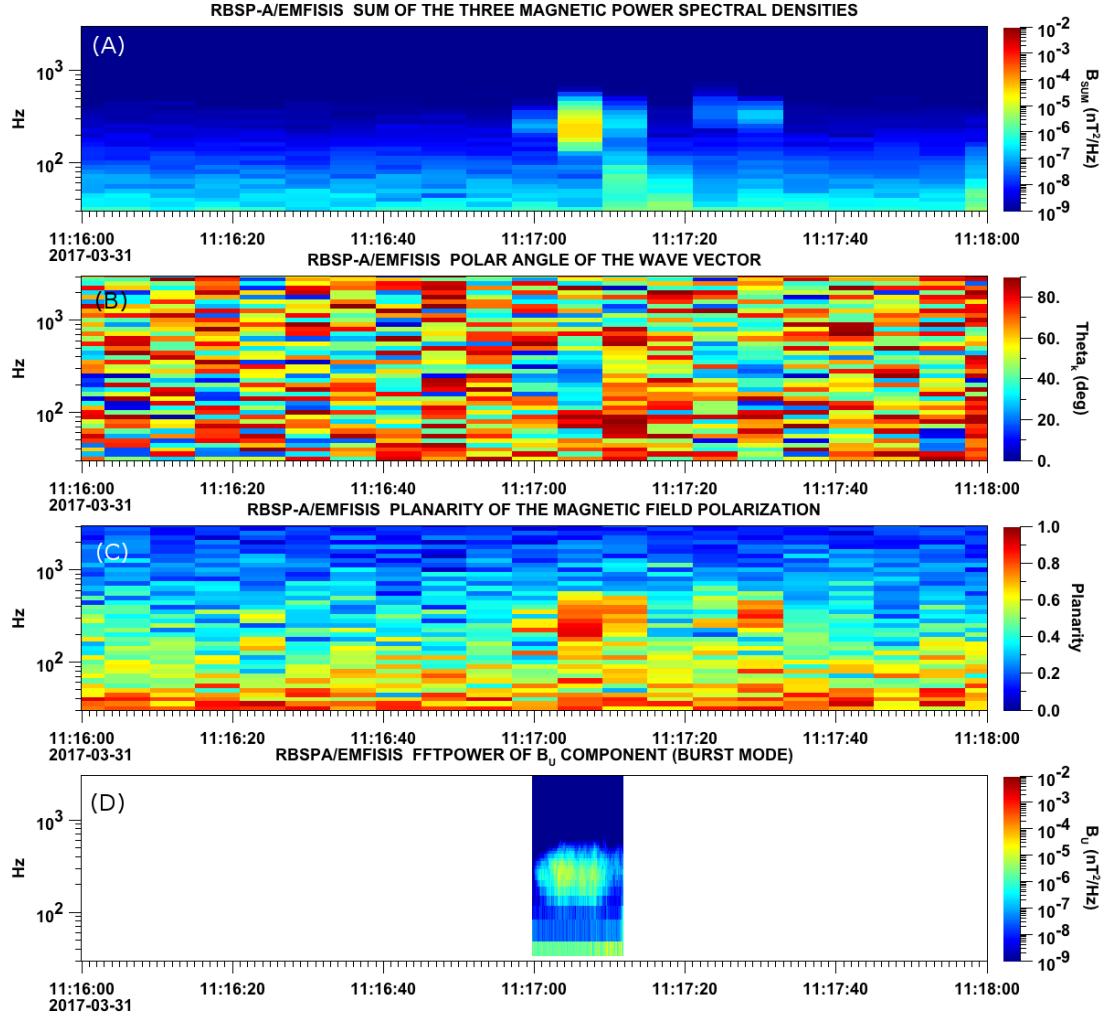


Figure A.1: Panel (A) shows the magnetic power spectral density as a function of frequency and time from the EMFISIS WFR instrument on board RBSP-A. The “hiss-like” wave used for the resonant diffusion analysis was observed starting at 11:17:03 UT. In the same format as panel (A), panel (B) shows the polar angle of the wave vector for this time period. The wave of interest had a normal wave vector,  $\theta_k < 30^\circ$ . Since the results in panel (B) are valid only for high planarity, panel (C) shows planarity in the same format as panels (A) and (B). The wave of interest was found to have a planarity of  $> 0.8$ . Lastly, panel (D) shows the available burst mode data.

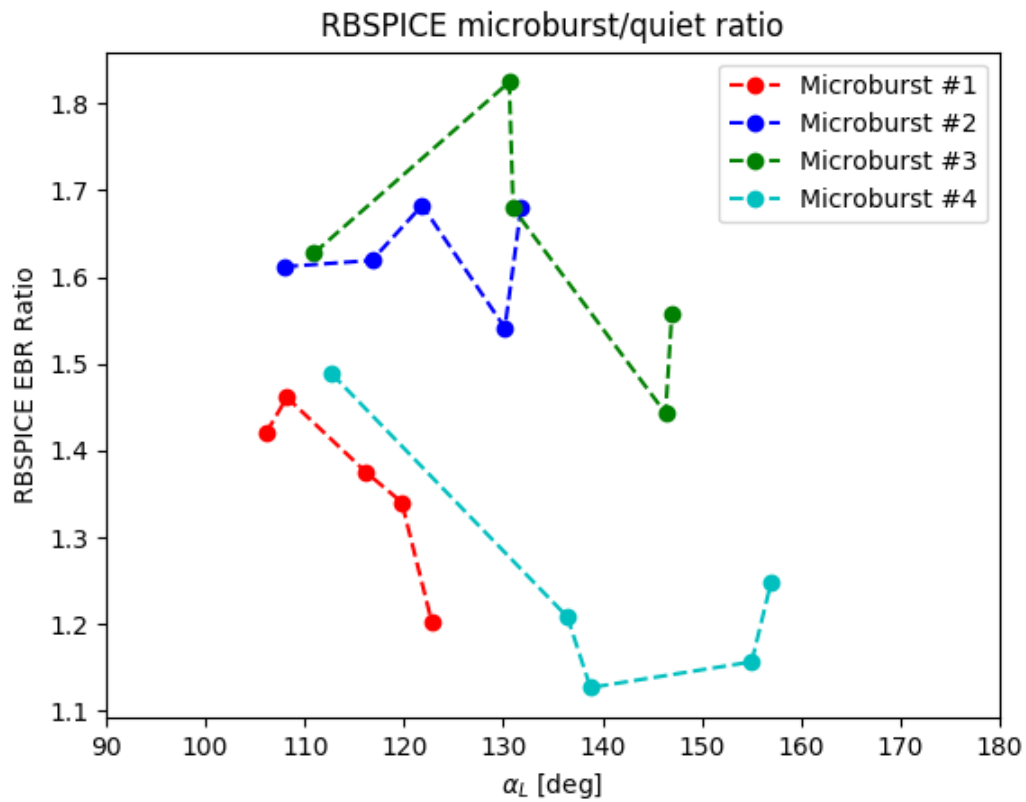


Figure A.2: Ratio of the RBSPICE EBR at microburst times indicated with the black vertical arrows in Fig. 2, to the EBR at the same pitch angles one spin prior (quiet time). The microburst flux was enhanced by 10-80% across  $100^\circ < \alpha_L < 160^\circ$  PA, and appear to be peaked closer to  $\alpha_L = 90^\circ$ .

1600

## APPENDIX: APPENDIX B

1601  
1602

This appendix describes the method we used to calculate the time difference and separation between FU3 and FU4 at 06:12 UT on February 2nd, 2015.

1603

Time and position correction1604  
1605

We used the following method to calculate the clock difference,  $\delta t_c$  and separation,  $d$  between FU3 and FU4 at 06:12 UT on February 2nd, 2015.

1606  
1607  
1608  
1609  
1610  
1611  
1612  
1613

The relative clock difference was calculated with a cross-correlation time lag analysis on uniquely-identified trains of microbursts that hit both spacecraft simultaneously. Four time periods with coincident microbursts were hand-picked on February 2nd, 2015 and are shown in Figs. B.1-B.4, panels (a) and (b). The cross-correlation time lag analysis was applied to the HiRes time series in panels (a) and (b), and the resulting normalized cross-correlation coefficient as a function of time is shown in panel (c). To validate the peak lag identified in panel (c), FU3's time series was shifted by that lag and is shown in panel (d).

1614  
1615  
1616  
1617  
1618  
1619

The clock differences from the simultaneous microbursts in Figs. B.1-B.4 were linearly fit to account for the relative clock drift ( $\approx 20$  ms/hour at this time), giving a value of  $\delta t_c = 2.28 \pm 0.12$  s at the time of the microburst analyzed here. This time shift was applied to the HiRes data in Fig. 1. A clock difference of  $\delta t_c = 2.45^{+0.51}_{-0.98}$  s was independently calculated with the FIREBIRD-II telemetry beacon time stamps that were downlinked during operational passes.

1620  
1621  
1622  
1623  
1624  
1625  
1626  
1627  
1628  
1629  
1630  
1631  
1632

We calculate the spacecraft separation, by applying same the cross-correlation time lag analysis on structures assumed to be spatial and are shown in Figs. B.5 and B.6. The lag from the peak cross-correlation between these events is a sum of the clock difference and time lag due to the spacecraft separation. We interpret the time lag due to the spacecraft separation as the time difference between when the leading satellite observed a stationary spatial feature, to when the trailing satellite observed the same stationary spatial feature. With the method described above, we find the spatial time lag to be  $\delta t_d = 2.64 \pm 0.12$  s (after we account for the clock difference and its uncertainty). To convert from a spatial time lag to a spacecraft separation, we calculate the satellite velocity. We calculate the velocity using a Two Line Element (TLE), a data format containing the orbit parameters that are used for orbit propagation. With the TLE derived spacecraft velocity,  $v = 7.57$  km/s, the spacecraft separation was  $d = 19.9 \pm 0.9$  km.

1633  
1634  
1635  
1636

An independent method to calculate the spacecraft separation was developed. The separation was calculated using TLEs. The TLE from February 2nd was anomalous and was not used in this analysis. Instead, seven TLEs released up to five days after the microburst event were backpropagated, using the SGP-4 algorithm

1637 (Hoots and Roehrich, 1980) that calculates orbital state vectors with perturbations  
1638 such as Earth's atmosphere, as well as gravitational effects from the moon and sun.  
1639 Then the predicted spacecraft separations at the time of the microburst event were  
1640 averaged to derive a separation of  $d = 18.4 \pm 1.5$  km. These two methods give  
1641 similar separations, which implies that the stationary event assumption used in the  
1642 cross-correlation time lag analysis is reasonable.

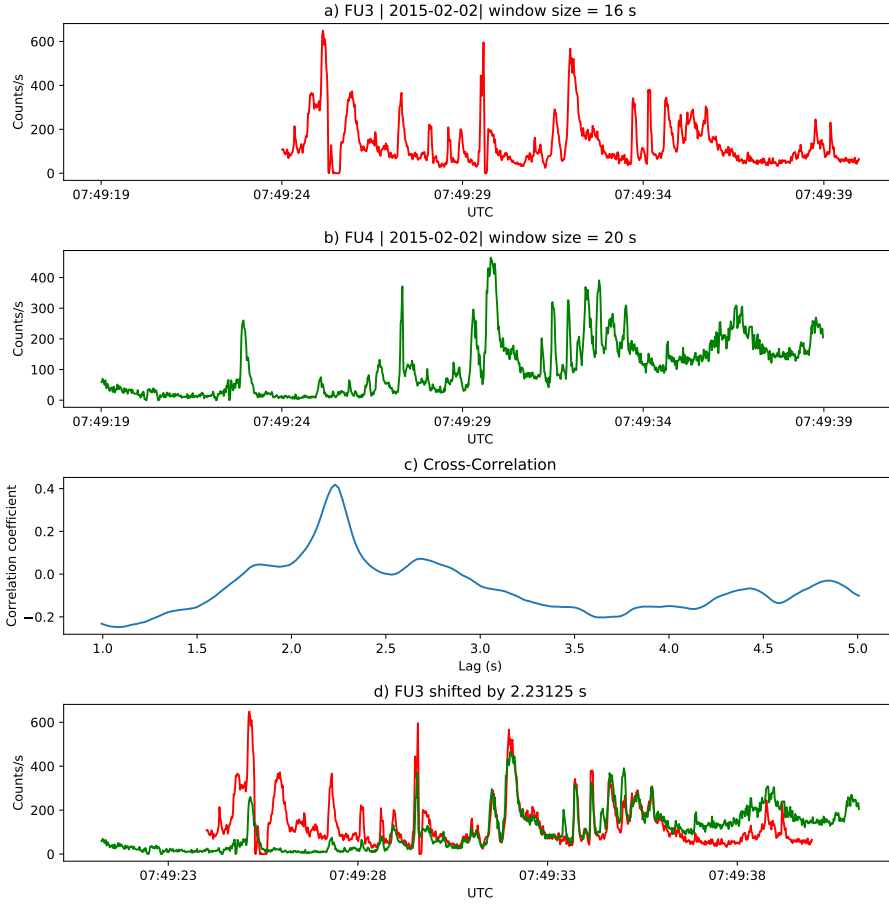


Figure B.1: Cross-correlation time lag analysis applied to a train of microbursts. Panel (a) and (b) show the count rate from the lowest energy channel. Panel (c) shows the cross-correlation coefficient as a function of time lag. Panel (d) shows the shifted timeseries. Clock difference was 2.23 s.

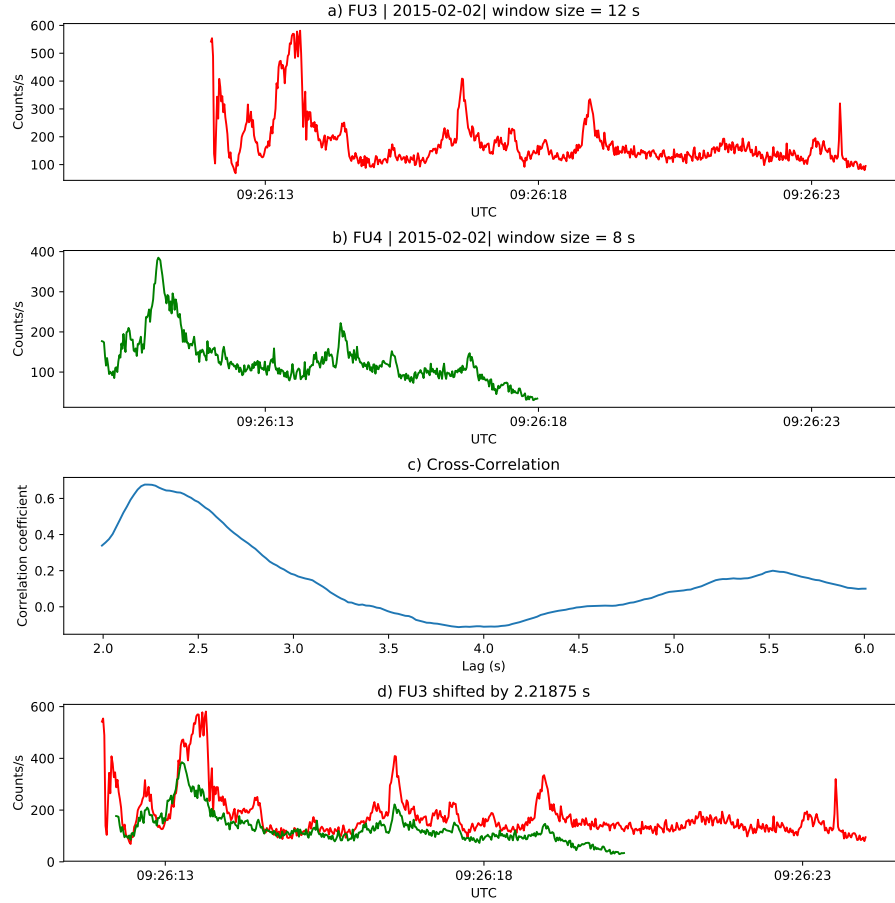


Figure B.2: Same analysis as Fig. B.1 on a different time period. Clock difference was 2.21 s.

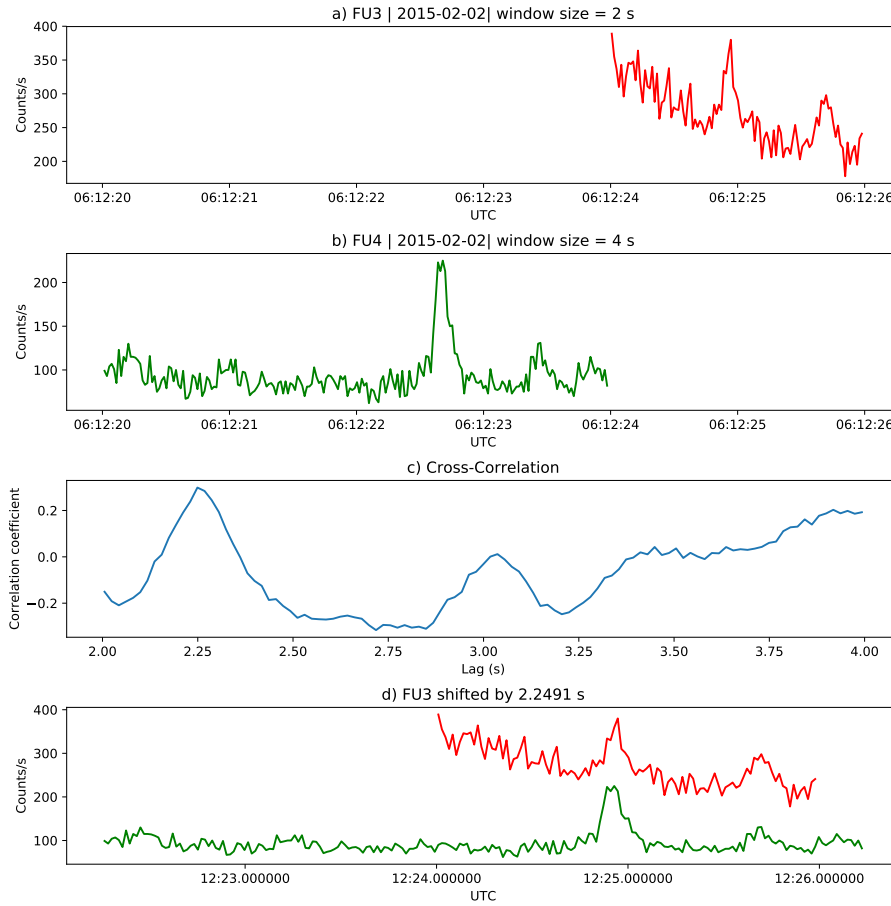


Figure B.3: Same analysis as Fig. B.1 on a different time period. Clock difference was 2.25 s.

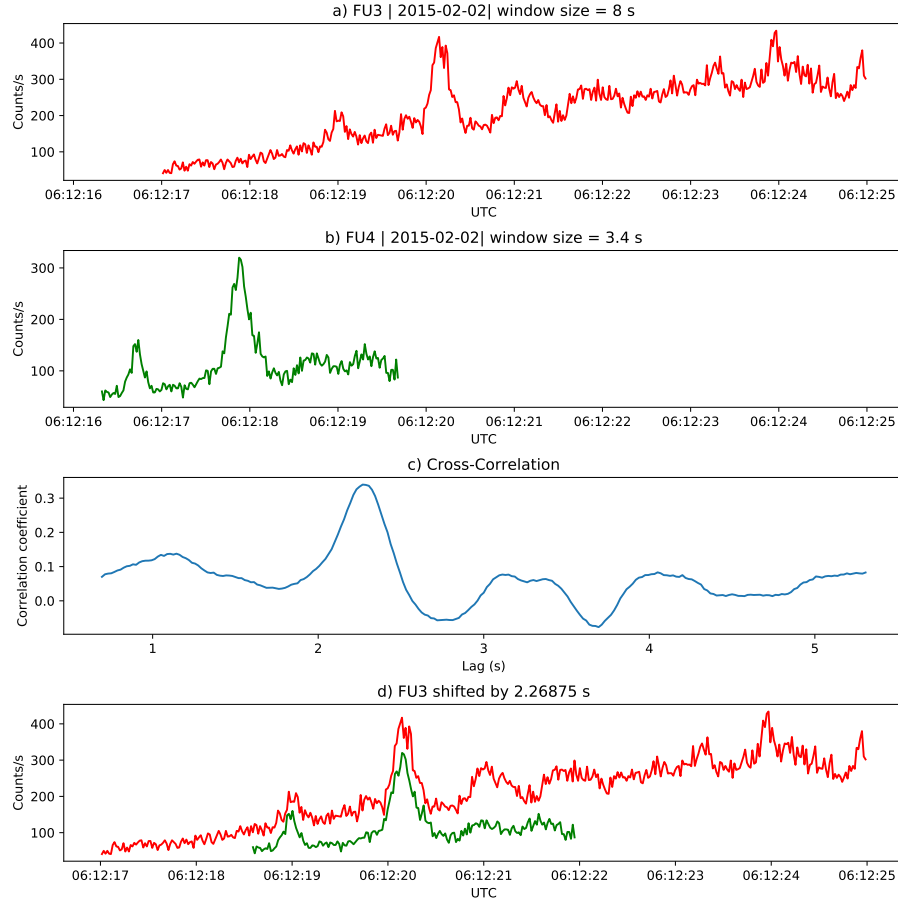


Figure B.4: Same analysis as Fig. B.1 on a different time period. Clock difference was 2.27 s.

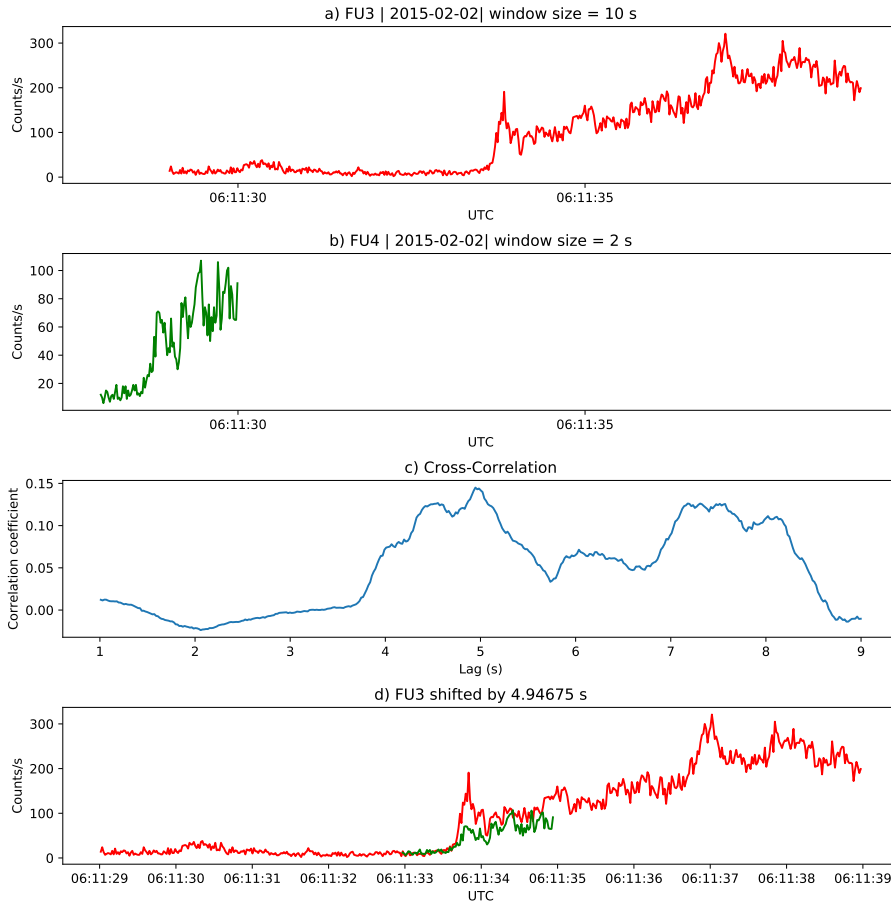


Figure B.5: Same cross-correlation time lag analysis applied to stationary spatial structures. The cross-correlation lag between these events is a sum of the clock difference and time lag due to the spacecraft separation. The lag derived at this time was 4.95 s.

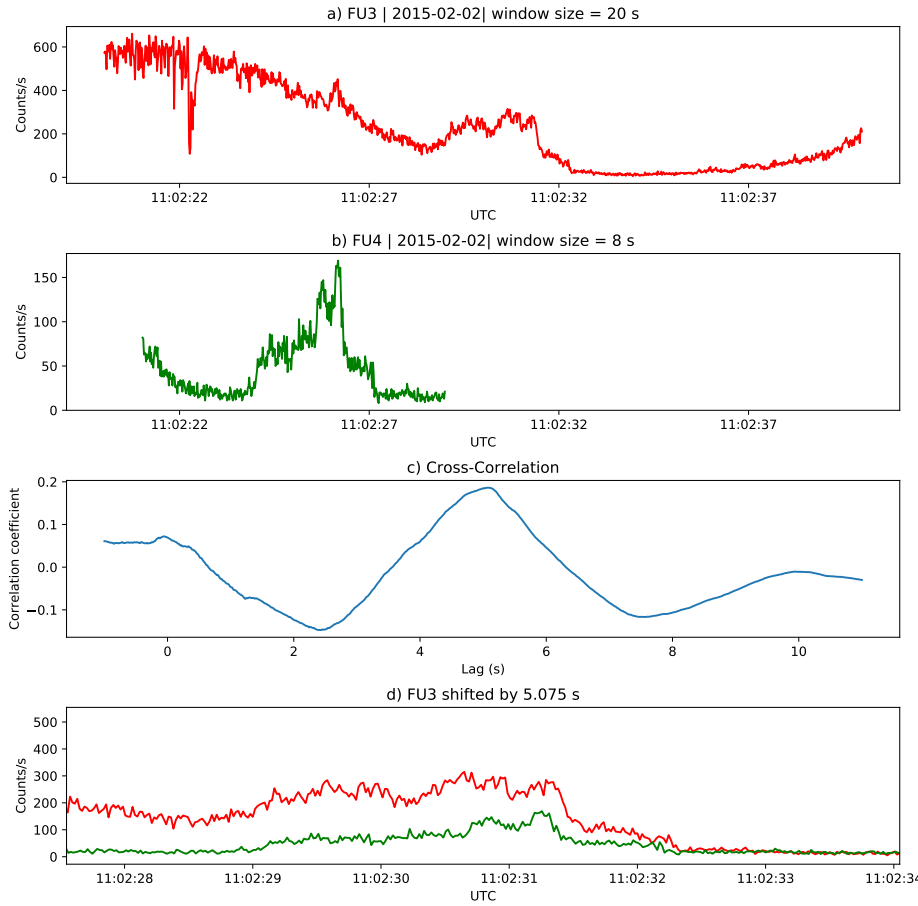


Figure B.6: Same analysis as Fig. B.5 applied to a different stationary spatial feature. The lag derived at this time was 5.01 s.